Trace metal analysis by laser ablation-inductively coupled plasma-mass spectrometry and x-ray K-edge densitometry of forensic samples

by

Jonna Elizabeth Berry

A dissertation submitted to the graduate faculty

in partial fulfillment of the requirements for the degree of

DOCTOR OF PHILOSOPHY

Major: Analytical Chemistry (Forensic Chemistry)

Program of Study Committee:
Robert S. Houk, Major Professor
Emily Smith
Young Jin Lee
Patricia Thiel
Thomas Holme

Iowa State University

Ames, Iowa

2015

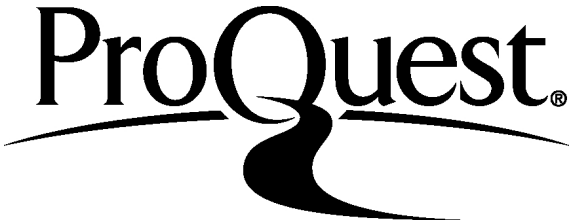

TABLE OF CONTENTS

ABSTRACT

This dissertation describes a variety of studies on the determination of trace elements in samples with forensic importance. Laser ablation-inductively coupled plasma-mass spectrometry (LA-ICP-MS) was used to determine the trace element composition of numerous lipstick samples. Lipstick samples were determined to be homogeneous. Most lipstick samples of similar colors were readily distinguishable at a 95% confidence interval based on trace element composition. Numerous strands of a multi-strand speaker cable were analyzed by LA-ICP-MS. The strands in this study are spatially heterogeneous in trace element composition. In actual forensic applications, the possibility of spatial heterogeneity must be considered, especially in cases where only small samples (e.g., copper wire fragments after an explosion) are available. The effects of many unpredictable variables, such as weather, temperature, and human activity, on the retention of gunshot residue (GSR) around projectile wounds were assessed with LA-ICP-MS. Skin samples around gunshot and stab wounds and larvae feeding in and around the wounds on decomposing pig carcasses were analyzed for elements consistent with GSR (Sb, Pb, Ba, and Cu). These elements were detected at higher levels in skin and larvae samples around the gunshot wounds compared to the stab wounds for an extended period of time throughout decomposition in both a winter and summer study. After decomposition, radiographic images of the pig bones containing possible damage from bullets revealed metallic particles embedded within a number of bones. Metallic particles within the bones were analyzed with x-ray, K-edge densitometry and determined to contain lead, indicating that bullet residue can be retained throughout decomposition and detected within bones containing projectile trauma.

CHAPTER 1. GENERAL INTRODUCTION

The History of Elemental Analysis

Techniques for accurate quantification of elements in solutions have greatly improved over the years. Many years ago, the concentration of an element in a solution was determined by measuring the weight of a precipitate after a chemical reaction (1). Later, quantification of a single element required a chemical reaction to separate the element from the solution, react it with a colorimetric agent, and quantification by absorption spectrophotometry or fluorimetry. These techniques were time consuming, required many steps which increased the risk for errors, and were generally capable of measuring only a single element per analysis.

The introduction of atomic spectroscopy methods allowed for the quantification of elements in a solution without chemical separations due to increased selectivity from narrower absorption or emission lines. The development of arc and spark emission excitation allowed for the analysis of more than one element at a time. However, photographic plate detection was cumbersome and no single excitation source or conditions provided optimal sensitivity for all elements (2). A few year later the first atomic absorption spectrophotometer (AAS) was constructed by Walsh (3). The sensitivity of the absorption method was improved compared to the emission methods because it was no longer dependent on the excitation potential of the spectral lines measured (3). AAS instrumentation was much more amenable to widespread, routine analysis than emission methods at the time.

In 1960, the first plasma torch based on inductive coupling to an ionized gas with a hole through the center of the plasma, at or near thermal equilibrium, was developed

(4). The inductively coupled plasma (ICP) is an atmospheric, high temperature atomization source (5000-6000 K) capable of vaporizing, atomizing and ionizing a variety of samples (5, 6). Soon after being developed, these high frequency induction type plasmas were used as spectrometric emission sources (7) and were capable of detecting multiple elements in aqueous solutions with very low detection limits (8).

Over the next 20 years inductively coupled plasma-atomic emission spectrometry (ICP-AES) gained prominence as a comprehensive and versatile technique for elemental analysis. Although ICP-AES is still widely used, it suffers from complex spectral lines and many background corrections were needed for analysis (9).

ICP-MS

The feasibility of ICP-mass spectrometry (MS) for determination of elemental concentrations and isotopic abundance ratios in solutions was first demonstrated by Houk *et al.* in 1980 (10). Today, ICP-MS is among the most powerful and sensitive techniques for elemental analysis.

The capability of ICP-MS to measure Li through U in a single analysis of a solution makes it a versatile technique for elemental analysis. Large linear dynamic range and extremely low detection limits of ICP-MS are advantageous for quantification of elements. Detection limits for ICP-MS range from parts-per-billion (ng/g) to the parts-per-quadrillion (fg/g) for a typical solution, depending on the element of interest and background levels. Many fields employ ICP-MS for elemental analysis, including geology (11), environmental chemistry (12), biochemistry (13), semiconductors (14), nanomaterials (15), nuclear chemistry (16), and forensic (17, 18).

Trace Element Analysis in Forensics

Comparison of samples by trace element composition can be useful in forensic analyses. A number of samples that may be acquired as evidence at a crime scene have been analyzed for trace element composition, such as glass (19, 20, 21), soil (22, 23), hair (24), teeth and bones (25), and drugs (26) by various techniques. Some such analysis techniques include particle induced x-ray emission (PIXE), micro x-ray fluorescence (mXRF), scanning electron microscopy-energy dispersive spectroscopy (SEM-EDX), spark source mass spectrometry, laser induced breakdown spectroscopy (LIBS), synchrotron radiation x-ray fluorescence, flame atomic absorption spectroscopy (FAAS), and graphite furnace-AAS.

Although there are many techniques used for elemental analysis in forensics, ICP-MS offers the potential for a highly sensitive, rapid, and cost effective analysis of small samples for identification and comparison of forensic evidence (27, 28). Many forensically related samples have been analyzed for trace elements by ICP-MS, such as, hair (29) and nails (30), cigarettes (31), charcoal ash (32), heroin (33, 34), and ginseng roots (35). Trace and ultratrace elemental analysis by ICP-MS has also been used in many forensic analyses to determine if samples are similar to or distinguishable from one another. This technique has been used to compare various samples such as steel and glass (27), including float (36), container (37), sheet (38), and automotive (39) glass, for forensic analysis. Unfortunately, analysis of solid samples by ICP-MS requires dissolution of the sample into an aqueous solution. Dissolution destroys the sample and information of the initial sample such as morphology or integrity is lost, which is a disadvantage when analyzing forensic samples.

LA-ICP-MS for Trace Element Analysis in Forensics

For analysis of solids by ICP-MS, there are two common options. Dissolving the sample yields better precision and is more easily calibrated but can be cumbersome and does destroy the original piece of evidence. However, original sample integrity is retained when laser ablation (LA)-ICP-MS is used directly on solids. Therefore, the speed, convenience, and limited sample destruction of LA sampling is an advantage for forensic work. Ablation of samples by LA-ICP-MS is relatively non-destructive and allows for replicate measurements of a sample, which may be required for forensic analyses. LA-ICP-MS has been used to distinguish between gold samples and also to determine their provenance (40). Other samples such as gemstones (41, 42), soils (17, 43), car paints (18), bones and teeth (44), and printing inks (45) have also been distinguished based on trace elemental composition measured with LA-ICP-MS. Trace elemental composition comparisons have also been used to determine the source of samples, such as i) a field where particular cannabis crops had been grown, (28) ii) mines from which gold samples were produced, (40) and iii) provenance of historical materials such as oriental porcelain, and ochers by LA-ICP-MS (46, 47).

However, not all forensic samples can be clearly distinguished from each other based on trace elemental composition using ICP-MS or LA-ICP-MS. In a nationally-prominent example, detailed investigation into compositional analysis of bullet lead by the Federal Bureau of Investigation (FBI) and the National Research Council (NRC) indicated many problems with the use of trace element composition for forensic comparison of lead bullets (48). It was determined that anywhere from 12,000 up to 35

million bullets for a 40-grain .22 caliber long rifle may be produced from "compositionally indistinguishable volumes of lead" (CIVL). Many bullet manufacturers also add scrap lead from the bullet production into the melt at random times, which sporadically changes the composition of the original melt (48).

In this dissertation, studies on three types of forensically related samples analyzed for trace element composition are presented. Lipstick samples were distinguished from one another based on trace element composition with LA-ICP-MS. LA-ICP-MS was also used to analyze copper wire samples to assess the variability in the trace element composition along the length of a wire. The presence of gunshot residue on tissue and in larval was determined from the amount of antimony, barium, lead, and copper on and within the pig tissue samples by LA-ICP-MS. Finally, the pig decomposition studies resulted in bones that apparently had very small (<0.5mm) bullet fragments in them. The presence of gunshot residue or bullet transfer within bone samples was determined by radiography and K-edge, x-ray densitometry. This latter method avoids even the small amount of sample destruction inflicted by LA-ICP-MS.

Analysis of Specific Forensic Samples for Trace Element Composition

Trace Elements in Lipsticks

Cosmetics, such as lipstick, recovered from a crime scene may provide valuable forensic information. Lipstick is worn regularly by many people, smears left on cigarette butts, glassware, clothing, bedding, napkins, paper, etc. may be valuable evidence in a forensic investigation (49, 50). Lipstick recovered from clothing or skin may also indicate physical contact between individuals. Forensic analysis of recovered lipstick smear evidence can provide valuable information on the recent activities of a

victim or suspect. Trace elemental analysis of lipstick smears could be used to complement existing visual comparative procedures to determine the lipstick brand and color.

Atomic spectroscopy methods are well suited for sensitive and selective analysis of complex samples. Lipstick samples have also been analyzed to determine trace metal concentrations, particularly for toxic metals. Techniques such as graphite furnace atomic absorption spectroscopy (AAS) (51), AAS for acid digested and solid lipstick samples (52, 53, 54), laser induced breakdown spectroscopy (LIBS) (55), ion chromatography (56), neutron activation analysis (NAA) (57), and SEM-EDS (58) have been used to analyze trace metals in lipsticks. Toxic metals in lipsticks have also been determined by ICP-AES (55) and ICP-MS, (59, 60, 61) but not LA-ICP-MS.

Trace Elements in Copper Wire

Speaker cable, typically composed of multiple strands of copper wire, is commonly used for binding or strangling victims and is often left at crime scenes. Fragments may also be recovered from electronic circuits or components after a bomb explosion. Comparison of one or more copper wire strands found at a crime scene to those found in the possession of a suspect could be used as evidence to link the suspect to the scene of the crime. A study by Dettman *et al.* (62) measured trace element concentrations in high-purity copper wire by solution ICP-MS. Unfortunately, dissolution destroys the sample which is a disadvantage when analyzing forensic evidence (62). Dettman *et al.* found substantial variability in the trace element composition along a ~20 m length of copper wire indicating trace element heterogeneity in high purity copper wire strands. However, even greater variability in the trace

element composition existed between different copper rods produced by a single manufacturer over a 10 day span and therefore high purity copper samples could still be distinguished from one another (62).

Trace Element Analysis of Gunshot Residue with LA-ICP-MS

Determining the type of trauma present on a recovered body, i.e. sharp force, blunt force, or projectile trauma, is important in forensic investigations to establish the cause of death. Projectile trauma can be difficult to distinguish from sharp force trauma on a decomposing carcass due to the stage of decomposition and insect activity around and within the wound tracts, (63, 64) especially if the bullet is not recovered at the scene. Only a few radiochemical and microscopic studies have been conducted regarding the analysis of gunshot wounds in decomposing remains (63, 65, 66, 67).

The current method to distinguish projectile trauma from other trauma is the detection of GSR around a wound. One composition consistent with GSR particles is a combination of lead, barium, and antimony in an individual particle (68). GSR is airborne vaporized particles which are ejected through the gun muzzle, cool rapidly into liquid droplets, and subsequently solidify (68). Copper and iron have also been detected in GSR particles (69). These particles are typically collected from a surface, i.e. the hand of a suspected shooter, with an adhesive stub and analyzed using scanning electron microscopy-energy dispersive x-ray spectroscopy (SEM-EDS) (70). SEM-EDS can non-destructively locate and provide morphological information on individual particles which is advantageous for forensic analysis of GSR. However, in most forensic casework, GSR is not analyzed on decomposing bodies due to the limitations of current GSR collection methods.

Decomposition is a progressive process and can be divided into five chronological stages: fresh; bloat; active decay; advanced decay; and dry or remains (67). During these stages the body undergoes many changes that may alter or obscure gunshot wound evidence on skin (67). Depending on the type of environment in which the body is exposed, the insect activity on the remains, and the stage of decomposition, GSR is only detectable by SEM-EDS around the entrance wound for a short period of time (~24 hours) (63). Efficient GSR collection may be hindered by liquids and adipocere that may be present on the surface of decomposing remains (63).

GSR particles on decomposing remains are difficult to detect with SEM-EDX. Therefore, organisms, such as fly larvae, that feed around wounds on decomposing tissue have been studied (63, 64, 65). ICP-MS was also used to analyze GSR on skin tissue around gunshot wounds on a pig carcass to distinguish projectile from sharp force trauma in later stages of decomposition (63). Elements consistent with gunshot residue were present at higher concentrations in the skin tissue around the gunshot wounds compared to the tissue around the stab wounds for 37 days after death in the summer and 60 days after death in the winter study (63). Udey *et al.* (69) further studied the GSR in tissue by examining the possibility of differentiating bullet types in fresh and decomposed tissue using ICP-MS. All of these studies were conducted using dissolved samples. Laser ablation (LA)-ICP-MS of larvae and tissue samples would provide faster results with less sample preparation for the detection of GSR compared to dissolution for ICP-MS analysis.

Trace Element Analysis of Gunshot Residue with Radiography and K-edge, X-ray Densitometry

GSR particles are radiopaque and are easily observed in radiographs (71, 72). In cases of gunshot injuries, radiographs can be used for the retrieval of the bullet or to visualize pieces of the bullet as well as metallic particles from the primer, the bullet, the cartridge case, and the firearm itself (73). In a study by Lantz *et al.*, radiopaque bullet residue was observed around the entrance wound of a victim shot by a .22 caliber rifle and analyzed with scanning electron microscopy-energy dispersive x-ray spectroscopy (SEM-EDX). Lead was determined to be the predominant element present.

K-edge absorption densitometry is capable of detecting heavy metals with high spatial resolution. This method has been used to measure and monitor uranium and plutonium in several samples in facilities around the world (74). In K-edge densitometry analysis, an X-ray beam is passed through a sample to a collimated energy-sensitive X-ray detector. At an energy corresponding to an absorption edge for an element, there is an abrupt decrease in transmission resulting in a step edge at a particular photon energy in the transmitted X-ray spectrum (75). The photon energies at which step edges occur identify the elements present in the sample. This technique can be used to identify the presence of lead in GSR or bullet transfer particles that are embedded within skeletonized remains.

Data Analysis for Comparison of Forensic Samples

Data analysis methodology is also important in forensic analysis. One simple yet valuable chemometric method is principal component analysis (PCA), which reduces multivariate data into a two- or three-dimensional scores plot. The scores plot depicts

most of the variation within a data set. PCA has been proven to be a useful, efficient, and reproducible technique for the comparison of forensic samples by trace elemental composition with LA-ICP-MS. (17, 37, 47, 76)

Dissertation Organization

The first chapter of this dissertation is an introduction to the history of elemental analysis, the use of elemental analysis in forensics, more specifically LA-ICP-MS, for trace elemental analysis of forensic samples, and a background on radiographic techniques in forensic analysis. Chapter 2 and 3 are manuscripts prepared for submission in a peer reviewed journal. These chapters describe the analysis of lipstick and copper wire samples for trace element homogeneity and to distinguish between samples based on trace element composition with LA-ICP-MS. Chapter 4 is a manuscript submitted to the *Journal of Forensic Science* regarding the detection of GSR on decomposing remains with LA-ICP-MS. Chapter 5 is a manuscript prepared for the submission to the *Journal of Forensic Science* on the detection of GSR within skeletonized remains by radiography and K-edge, x-ray densitometry. Chapter 6 presents general conclusions of this dissertation. Appendix A is a paper published in Organic Electronics for which I contributed analysis of the composition of the solar cell by LA-ICP-MS.

References

1. Lundell GEF. The chemical analysis of things as they are. Ind and Eng Chem, Anal Edition 1933;5:221-225.
2. Smith DM. Spectrographic analysis of rare and high purity materials. Analyst 1946;71:368-375.
3. Russell BJ, Shelton JP, Walsh A. An atomic-absorption spectrophotometer and its application to the analysis of solutions. Spectrochim Acta 1957;8:317-328.

4. Reed TB. Induction-coupled plasma torch. J Appl Phys 1961;32:821-824.
5. Houk RS, Thompson JJ. Inductively coupled plasma mass spectrometry. Mass Spec Rev 7 1988:425-461.
6. Jarvis KE, Gray AL, Houk RS. Handbook of inductively coupled plasma mass spectrometry. New York: Chapman and Hall, 1992.
7. Greenfield S, Jones IL, Berry CT. High-pressure plasmas as spectroscopic emission sources. Analyst 1964;89:713-720.
8. Wendt RH, Fassel VA. Induction-coupled plasma spectrometric excitation souce. Anal Chem 1965;37:920-922.
9. Douglas D, Rosenblatt G, Quan E. Inductively coupled plasma-mass spectrometry- a new technique for trace element analysis. Trace Substanes in Environmental Heath - XVII, Columbia; 1983.
10. Houk RS, Fassel VA, Flesch GD, Svec HJ, Inductively coupled argon plasma as an ion sounce for mass spectrometric determination of trace elements. Anal Chem 1980;52:2283-2289.
11. Linge K, Jarvis K. "Quadrupole ICP-MS: Introduction to Instrumentation, Measurement Techniques and Analytical Capabilities," Geostan Geoanal Res 2009;33:445-467.
12. Garbe-Schonberg CD, Reimann C, Pavlov VA. Laser ablation ICP-MS analyses of tree-ring profiles in pine and birch from norway and NW russia. A reliable record of the pollution history of the area. Environ Geol 1997;32:9-16.
13. Li F, Armstrong D, Houk RS. Behavior of bacteria in the inductively coupled plasma: atomization and production of atomic ions for mass spectrometry. Anal Chem 2005;77:1407-1413.
14. Horn M. Applications of ICP-MS in semiconductor industry. Fresenius J Anal Chem 1999;364:385-390.
15. Yang MH, Lin CH, Chang LW, Lin P. Application of ICP-MS for the study of desposition and toxicity of metal-based nanomaterials. Nanotox 2012;926:345-359.
16. Becker JS, Pickhardt C, Dietze H. Laser ablation inductively coupled plasma mass spectrometry for the trace, ultratrace and isotope analysis of long-lived radionuclides in solid samples. Int J Mass Spec 2000;202:283-297.
17. Arroyo L, Trejos T, Hosick T, Machemer S, Almirall J, Gardinali P. Analysis of soils and sediments by laser ablation inductively coupled plasma mass spectrometry (LA-ICP-MS): an innovative tool for enviromental forensics. Environ Forensics 2010;11:315-327.
18. Deconinck I, Latkoczy C, Günther D, Govaert F, Vanhaecke F. Capabilities of laser ablation-inductively coupled plasma mass spectrometry for (trace) element analysis of car paints for forensic purposes. J Anal At Spectrom 2006;21:279-287.
19. Ernst T, Berman T, Buscaglia J, Eckert-Lumsdon T, Hanlon C et al. Signal-to-noise ratios in forensic glass analysis by micro x-ray fluorescence spectrometry. X-Ray Spec 2014;43:13-21.

20. DeYoung P, Hall C, Mears P, Padilla D, Sampson J, Peaslee R et al. Comparison of glass fragments using particle-induced x-ray emission (PIXE) spectrometry. J Forensic Sci 2011:366-371.
21. Butterworth A, German B, Morgans D, Scaplehorn A. Trace elements present in vehicle headlamp and auxiliary lamp glasses. J Forensic Sci Soc 1974:41-45.
22. Woods B, Kirkbride P, Lennard C, Robertson J. Soil examination for a forensic trace evidence laboratory- part 2: elemental analysis. Forensic Sci Int 2014;245:195-201.
23. Furuya S, Bong W, Maeda I, Suzuki H, Abe Y, Osaka K et al. Development of trace heavy element quantification in soil samples by using high-energy (116 keV) synchrotron radiation x-ray fluorescence analysis for forensic investigations. X-sen Bunseki no Shinpo 2012;43:341-354.
24. Fakayode S, Owen S, Pollard D, Yakubu M. Use of flame atomic absorption spectroscopy and multivariate analysis for the determination of trace elements in human scalp. Am J Anal Chem 2013;4:348-359.
25. Pye K. Isotope and trace element analysis of human teeth and bones for forensic purposes. Geo Soc Special Pub 2004;232:215-236.
26. French H, Went M, Gibson S. Graphite furnace atomic absorption elemental analysis of ecstasy tablets. Forensic Sci Int 2013;231:88-91.
27. Watling JR, Lynch B, Herring D. Use of laser ablation inductively coupled plasma mass spectrometry for fingerprinting scene of crime evidence. J Anal Atom Spectrom 1997;12:195-203.
28. Watling JR. Sourcing the provenance of cannabis crops using inter-element association patterns 'fingerprinting' and laser ablation inductively coupled plasma mass spectrometry. J Anal At Spectrom 1998;13:917-926.
29. Lemos Batista B, Lisboa Rodrigues J, de Oliverira S, Vanessa C, Barbosa F. A fast ultrasound-assisted extraction procedure for trace elements determination in hair samples by ICP-MS for forensic analysis. Forensic Sci Int 2009;192(1-3):88-93.
30. Brown JNI, Robertson J, Brockman J. Measurement of U and Pu isotope ratios in hair and nail samples using extraction chromatography and multi-collector inductively coupled plasma mass spectrometry. Talanta 2014;129:481-485.
31. Suzuki Y, Suzuki S. Trace element analysis of cigarette and cigarette ash by ICP-MS and its application for forensic discrimination. Bunseki Kagaku 2012;61:911-916.
32. Kasamatsu M, Suzuki Y. Application of trace element analysis using ICP-MS to forensic discrimination of charcoal ash. Bunseki Kagaku 2012;61:577-581.
33. Chan KW, Tan GH, Wong R. ICP-MS method validation for the analysis of trace elements in illicit herion. Anal Letters 2012;45:1122-1132.
34. Licsandru A, Nacea V, Boscencu R. Investigation of uncertainty contributions for elemental analysis of seized street herion by ICPMS. Revista de Chem 2013;64:1237-1242.

35. Peake BM, Tong AY, Wells WJ, Harraway J, Niven B, Weege B et al. Determination of trace metal concentrations in ginseng (Panax Quinquefolius (American)) roots for forensic comparison using inductively coupled plasma mass-spectrometry. Forensic Sci Int 2015;251:214-219.
36. Berends-Montero S, Wiarda W, de Joode P, van der Peijl G. Forensic analysis of float glass using laser ablation inductively coupled plasma mass spectrometry (LA-ICP-MS): validation of a method. J Anal Atom Spec 2006;21:1185-1193.
37. Bajic S, Aeschliman D, Saetveit N, Baldwin D, Houk RS. Analysis of glass fragments by laser ablation-inductively coupled plasma-mass spectrometry and principal component analysis. J Forensic Sci 2005;50:1123-1127.
38. Suzuki Y, Kikkawa HS, Kasamatsu M, Higashikawa Y, Suzuki S. Forensic discrimination of sheet glass exposed to high temperature by the determination of trace impurities using ICP-MS. Anal Sci 2008;24:745-749.
39. Naes B, Umpierrez S, Ryland S, Barnett C, Almirall J. A comparison of laser ablation inductively coupled plasma mass spectrometry, micro x-ray fluorescence spectroscopy, and laser induced breakdown spectroscopy for the discrimination of automotive glass. Spectrochimica Acta Part B: Atom Spec 2008;63:1145-1150.
40. Watling JR, Herbert H, Delev D, Abell ID. Gold fingerprinting by laser ablation inductively coupled plasma mass spectrometry. Spectrochimica Acta Part B: Atom Spec 1994;49B:205-219.
41. Watling JR, Herbert HK, Barrow IS, Thomas AG. Analysis of diamonds and indicator minerals for diamond exploration by laser ablation-inductively coupled plasma mass spectrometry. Analyst 1995;120:1357-1364.
42. Guillong M, Gunther D. Quasi "non-destructive" laser ablation-inductively coupled plasma-mass spectrometry fingerprinting of sapphires. Spectrochimica Acta Part B: Atom Spec 2001;56B:1219-1231.
43. Jantzi SC, Almirall JR. Elemental analysis and forensic comparison of soils by laser ablation inductively coupled plasma mass spectrometry (LA-ICP-MS) and laser-induced breakdown spectroscopy (LIBS) with multivariate discrimination: tape mounting as an alternative to pellets. Appl Spec 2014;68:963-974.
44. Castro W, Hoogewerff J, Latkoczy C, Almirall J. Application of laser ablation (LA-ICP-SF-MS) for the elemental analysis of bone and teeth sample for discrimination purposes. Forensic Sci Int 2010;195:17-27.
45. Subedi K, Trejos T, Almirall J. Forensic analysis of printing inks using tandem laser induced breakdown spectroscopy and laser ablation inductively coupled plasma mass spectrometry. Spectrochim. Acta Part B: Atom Spec 2015;103-104:76-83.
46. Bartle E, Watling JR. Provenance determination of oriental porcelain using laser ablation-inductively coupled plasma-mass spectrometry. J of Forensic Sci 2007;52:341-348.
47. Green R, Watling JR. Trace element fingerprinting of australian ocher using laser ablation inductively coupled plasma-mass spectrometry (LA-ICP-MS) for the provenance establishment and authentication of indigenous art. J of Forensic Sci 2007;52:851-859.

48. National Research Council (U.S.) CoSAoBLECC. Forensic analysis: weighing bullet lead evidence. Washington, D.C: National Academies Press, 2004.
49. López-López M, Özbek N, García-Ruiz C. Confocal raman spectroscopy to trace lipsick with their smudges on different surfaces. Talanta 2014;123:135-139.
50. Ehara Y, Marumo Y. Identification of lipstick smears by fluorescence observation and purge-and-trap gas chromatography. Forensic Sci Int 1998;96:1-10.
51. Rodrigues Soares A, Nascentes CC. Development of a simple method for the determination of lead in lipstick using alkaline solubilization and graphite furnace atomic absorption spectrometry. Talanta 2013;105:272-277.
52. Gunduz S, Akman S. Investigation of lead contents in lipsticks by solid sampling high resolution continuum source electrothermal atomic absorption spectrometry. Regul Tox Pharm 2013;65(1):34-37.
53. Al-Saleh I, Al-Enazi S. Trace metals in lipsticks. Toxicol Environ Chem 2011;93(6):1149-1165.
54. Al-Saleh I, Al-Enazi S, Shinwari N. Assessment of lead in cosmetic products. Regul Tox Pharm 2009;54:105-113.
55. Gondal MA, Seddigi ZS, Nasr MM, Gondal B. Spectroscopic detection of health hazardous contaminants in lipstick using laser induced breakdown spectroscopy. J Hazard Mater 2010;175:726-732.
56. Lee S, Jeong H, Chang I. Simultaneous determination of heavy metals in cosmetic products. J Cosmet Sci 2008;59:441-448.
57. Misra G, Mittal VK. Neutron activation analysis of lipsticks using gamma-ray spectrometry. J Appl Spectrosc 2004;71(2):270-274.
58. Choudhry MY. Comparison of minute smears of lipstick by microspectrophotometry and scanning electron microscopy/energy-dispersive spectroscopy. J Forensic Sci 1991;36(2):366-375.
59. Piccinini P, Piecha M, Torrent SF. European survey on the content of lead in lip products. J. Pharnaceut Biomed 2013;76:225-233.
60. Atkins P. Analysis of lipstick for toxic elements using ICP-MS. SPEX CertiPrep, Metuchen, 2012.
61. Hepp N. Determination of total lead in 400 lipsticks on the U.S. market using a validated mircrowave-assisted digestion, inductively coupled plasma-mass spectrometric method. J Cosmet Sci 2012;63:159-176.
62. Dettman J, Cassabaum A, Saunders CP, Snyder DL, Buscaglia J. Forensic discrimination of copper items using trace element concentrations. Anal Chem 2014;86:8176-8182.
63. LaGoo L, Schaefer LS, Szymanski DW, Smith RW. Detction of gunshot residue in blowfly larvae and decomposing porcine tissue using inductively coupled plasma mass spectrometry (ICP-MS). J Forensic Sci 2010;55(3):624-632.
64. Rashid RA, Ariffuddin N, Ahmad NW. Blowfly, Chrysomya megacephala as an alternative specimen in determination of gunshot residue. IEEE S Bus Eng and Ind App 2012:542-547.

65. Roeterdink EM, Dadour IR, Watling JR. Extraction of gunshot tesidues from the larvae of the forensically important blowfly Claaiphora dubia (macquart) (Diptera: Calliphoridae). Int J Legal Med 2004;118:63-70.
66. Taborelli A, Gibelli D, Rizzi A, Andreola S, Brandone A, Cattaneo C. Gunshot residues on dry bone after decomposition-a pilot study. J Forensic Sci 2012;57(5):1281-1284.
67. MacAulay LE, Barr DG, Strongman DB. Effects of decomposition on gunshot wound characteristics: under moderate temperatures with insect activity. J Forensic Sci 2009;54(2):443-447.
68. Dalby O, Butler D, Birkett JW. Analysis of gunshot residue and associated materials--a review. J Forensic Sci 2010;55(4):924-943.
69. Udey RN, Hunter BC, Smith RW. Differentiation of bullet type based on the analysis of gunshot residue using inductively coupled plasma mass spectrometry. J Forensic Sci 2011;56(5):1268-1276.
70. Germani MS. Evaluation of instrumental parameters for sutomated scanning electron microscopy/ gunshot residue particle analysis. J Canadian Soc of Forensic Sci 1991;36(2):331-342.
71. Brogdon BG. Forensic Radiology. Boca Raton: CRC Press, 1998.
72. Lantz PE, Jerome GW, Jaworski JA. Radiopaque deposits surrounding a contact small-caliber gunshot wound. Am J Foren Med Path 1994;15(1):10-13.
73. Romolo SF, Margot P. Identification of gunshot residue: a critical review. For Sci Int 2001;119:195-211.
74. Aljundi T, Jensen T, Gray JN. Heavy metal contamination detection using x-rays. Quant Nondes Eval 1996;15:465-472.
75. Jensen T, Aljundi T, Gray JN. Using x-ray, K-edge densitometry in spent fuel characterization. Proceedings of the Topical Meeting on the DOE Spent Nuclear Fuel and Fissile Materials Management; 1998: Charleston.
76. Aeschliman D, Bajic S, Baldwin D, Houk RS. Multivariate pattern matching of trace elements in solids by laser ablation-inductively coupled plasma-mass spectrometry: source attribution and preliminary diagnosis of fractionation. Anal Chem 2004;76:3119-3125.

CHAPTER 2. DISTINGUISHING LIPSTICK SAMPLES OF SIMILAR COLORS BY TRACE ELEMENT ANALYSIS FOR FORENSIC COMPARISONS

Jonna Berry and R. S. Houk

Abstract

Cosmetic evidence, such as lipstick, can be useful to evaluate a link between a suspect and a victim or crime scene. Trace element composition of lipstick samples was determined using laser ablation-inductively coupled plasma-mass spectrometry (LA-ICP-MS). Three sections of 28 lipstick samples were analyzed with LA-ICP-MS to assess the homogeneity in trace element composition throughout a lipstick sample. Compositional variability within a lipstick sample and between different lipstick samples was assessed with principal component analysis on mass spectra collected from three sections of 28 lipsticks during LA-ICP-MS. Lipstick samples were determined to be homogeneous in elemental composition. Most lipstick samples of similar colors were readily distinguishable at a 95% confidence interval (C.I.) based on trace element composition. Lipsticks in the Dark Brown color group were distinguishable within only an 80% C.I.

Introduction

Cosmetics, such as lipstick, recovered from a crime scene may provide valuable forensic information. Lipstick is worn regularly by many people and lipstick smears left on cigarette butts, glassware, clothing, bedding, napkins, paper, etc. may be valuable evidence (1, 2). Lipstick recovered from clothing or skin may also indicate physical contact between individuals. Forensic analysis of recovered lipstick smear evidence can provide valuable information on the recent activities of a victim or suspect. Trace

elemental analysis of lipstick smears could be used to complement existing visual comparative procedures to determine the lipstick brand and color.

Previous forensic techniques employed for the organic analysis of lipsticks by compositional comparison include thin layer chromatography (TLC) (3, 4, 5), gas chromatography (GC) (3, 4, 6), and high performance liquid chromatography (HPLC) (7, 8). These methods provide useful information regarding the identification of lipsticks. However, they all require long sample preparation times and destroy the sample.

Nondestructive techniques for the forensic analysis of lipstick smears include UV fluorescence observation combined with purge-and-trap gas chromatography (2), microspectrophotometry and scanning electron microscopy energy dispersive spectroscopy (SEM-EDS) (9), and Raman spectroscopy (1, 10, 11, 12). However, background from particular substrates such as paper and fibers and fluorescence from lipstick smears can cause interferences of some lipstick spectra (1, 9, 10, 11).

Atomic spectroscopy methods are well suited for sensitive and selective analysis of complex samples. Lipsticks have also been analyzed to determine trace metal concentrations, particularly for toxic metals. Many techniques have been used to analyze trace metals in lipsticks: graphite furnace atomic absorption spectroscopy (AAS) (13), AAS for acid digested and solid lipstick samples (14, 15, 16), laser induced breakdown spectroscopy (LIBS) (17), ion chromatography (18), neutron activation analysis (NAA) (19), and SEM-EDS (9). ICP-atomic emission spectroscopy (ICP-AES) (17) and ICP-MS (20, 21, 22) have also been used to determine toxic metals in lipsticks.

ICP-MS also offers the potential for a highly sensitive, rapid, and cost effective analysis of small samples for identification and comparison of forensic evidence (23, 24).

Trace and ultratrace elemental analysis by ICP-MS has been used to determine if various materials are similar to or distinguishable from one another based on trace element composition. Various samples of steel and glass, including float, container, sheet, and automotive glass, have been compared to one another for forensic analysis using this technique (23, 25, 26, 27).

Samples are usually dissolved for ICP-MS analysis. However, original sample integrity is retained when laser ablation (LA)-ICP-MS is used directly on solids. Ablation of samples by LA-ICP-MS is relatively non-destructive and allows for replicate measurements of a sample, which may be required for forensic analyses. The speed and convenience of sampling with LA-ICP-MS is also advantageous for forensic work. Samples such as gemstones, soils, gold, and car paints have been distinguished based on trace elemental composition by LA-ICP-MS (28, 29, 30, 31, 32). Trace elemental composition comparisons have also been used to determine the source of samples, such as a) a field where particular cannabis crops had been grown, (24) b) mines from which gold samples were produced, (32) and c) materials such as oriental porcelain, and ochers by LA-ICP-MS (33, 34).

Data analysis methodology is also important in forensic analysis. Principal component analysis reduces multivariate data into a simple, two- or three-dimensional scores plot. The scores plot allows for visual interpretation of most of the variation within and between samples in a data set. PCA provides quantitative statistical data as to similarities or differences between samples. PCA has proven to be a fast, efficient, and reproducible technique for the comparison of forensic samples by trace elemental composition with LA-ICP-MS (25, 30, 34, 35).

Experimental

Elemental composition and homogeneity of 28 lipstick samples were determined by LA-ICP-MS. Thirteen lipstick samples were purchased new from a store. Two sticks of lipstick each of the same brand and color were obtained in order to determine if duplicate lipstick samples had indistinguishable trace elemental composition. Duplicate lipstick samples were purchased for five different colors; these duplicates labeled are a or b in Table 1. Used lipstick samples were donated by students and faculty at Iowa State University (n=15) (Table 1). Lipstick samples were observed visually and samples that were indistinguishable in color were grouped together into eight color groups (Table 1).

Full Mass Scan of Lipsticks to Identify Elements Present

Each lipstick was analyzed by LA-ICP-MS to determine the trace element composition. Four to five smears of lipstick, around 2.4 cm x 5 mm, were applied to clean Teflon squares (2.5 x 2.5 cm) for laser ablation. Teflon contains minimal trace metal background and thus was chosen as the substrate for the lipstick smears. The Teflon squares were soaked in 12% nitric acid with 18 MΩ·cm Millipore water for a minimum of 48 hours before use. The nitric acid was prepared by in-house sub-boiling distillation. The lipstick smears were ablated with a femtosecond laser (Coherent Libra Ti:Sapphire, pulse width 100 fs, frequency tripled to 266 nm, Santa Clara, CA) laser in a single line scan pattern. Argon was used as the carrier gas through the ablation cell. The nominal spot size was ~70 µm.

Full elemental mass spectra were acquired using a quadrupole ICP-MS (Bruker Aurora Elite, now Analytik Jena) to identify the elements present. Instrument and laser parameters were optimized for maximum stability and sensitivity during the ablation of

NIST 610 glass. Signals for all m/z values were measured in peak hopping mode. Background was measured during the ablation of an area on the Teflon square that did not contain lipstick. Other instrument parameters are listed in Table 2 and selected m/z values for the following analysis are listed in Table 3

Homogeneity and Distinguishability of Lipsticks

Lipstick samples were separated into seven color groups based on smear color. The homogeneity of the trace elemental composition within each stick was determined and lipsticks within a color group were compared to one another in the same experiment. To assess trace element homogeneity, each stick was cut into three sections with non-flavored non-waxed dental floss, rather than a metal knife. The first section of the stick of lipstick is referred to as the "top" section, the next section as the "middle", and the last section nearest the bottom of the stick is labeled as the "bottom". Each lipstick section was smeared onto clean Teflon squares and ablated in the same manner as described previously. The m/z values selected from the full mass scan experiment (Table 3) were measured during the ablation of each smear. Ten mass spectra were collected per section of lipstick. Background was measured during the ablation of an area on the Teflon square that did not contain lipstick.

Data Analysis

PCA was performed on the acquired mass spectra in order to determine whether the lipstick samples were homogeneous in trace elemental composition throughout a lipstick sample and distinguishable within a color group. Blank subtracted signals below the limit of detection were denoted as zeros. After signals were corrected for the limit of detection, each mass spectrum was normalized to the signal with the highest intensity,

either $^{48}Ti^{+}$, $^{209}Bi^{+}$, $^{138}Ba^{+}$, or $^{27}Al^{+}$ (Table 1). The signals from all isotopes of the reference element were removed from the PCA. Solo Eigenvector version 6.5.1 was used for the PCA comparison of mass spectra. No other scaling or preprocessing was used before data were input into the PCA software.

Results and Discussion

Multielement mass spectra were acquired from every stick of lipstick to determine all trace elements present in at least one of the lipstick samples. Figure 1 is the multielement mass spectrum from lipstick sample Red 1; the y-axis is set to a maximum of $1.0x10^{6}$ c/s in order to view the trace elements. Isotopes present in at least one lipstick sample were measured for homogeneity of a single lipstick sample and for distinction between different lipstick samples (Table 3).

Three sections of each of the 28 lipstick samples were analyzed. PCA allows for a visual representation of the variation in large amounts of data, such as numerous mass spectra, for comparison purposes. Data points which cluster in similar score space in a PCA scores plot indicate the samples are similar, or indistinguishable. In contrast, data points that occupy separate regions in score space have more variation between different sets than within each set and are distinguishable from one another.

Homogeneity of Trace Element Composition within a Lipstick Sample

Trace element composition was determined for three sections (top, middle, and bottom) of each lipstick sample by LA-ICP-MS. Ten mass spectra per section of lipstick were included into the PCA scores plots. Each mass spectrum is generated as a single data point on the PCA scores plots (Figs. 2-9). The ten replicate mass spectra of each

lipstick section generally cluster together in PCA score space, indicating good reproducibility and little variation between the mass spectra of a lipstick section. Mass spectra from the top, middle, and bottom sections of the same lipstick sample also generally overlap in score space (Figs. 2-9). Good overlap of the points from the three lipstick sections is observed in both Light Pink samples in Figure 3. This indicates that most sections of a lipstick sample are indistinguishable from one another based on trace element composition. These results indicate the lipstick samples in this experiment have little variation in trace element composition throughout a stick of lipstick and can be considered homogeneous.

Replicate mass spectra of some lipstick samples occupy larger PCA score space than others, i.e. lipstick samples Red 4 (Fig. 2), Orange 2 (Fig. 4), Light Brown 3a and 3b (Fig. 8), and Dark Brown 1a and 1b (Fig. 9). These lipstick samples have a higher variability in trace element composition, however, replicates from the top, middle, and bottom sections overlap in score space and are still considered indistinguishable. Replicate mass spectra of lipstick sections that occupy a smaller amount of score space contain less variability in trace element composition.

Distinguishing Lipstick Samples of Similar Color

Lipstick samples were separated into eight color groups based on visual similarities (Table 1). The mass spectra of the top, middle, and bottom section of each lipstick sample were compared to the mass spectra from the other lipstick samples within a color group with PCA. In PCA plots of each color group, sections of a lipstick sample generally cluster in separate regions of score space from other sections of lipstick samples of different brands and colors (Figs. 2-9). For example, the three lipstick

samples in the Orange color group cluster separately in score space from one another and are distinguishable (Fig. 4). The variability in trace element composition between lipstick samples is greater than the trace element variability within a single lipstick sample. In this study, most lipstick samples of different brands or colors are distinguishable from other lipstick samples of similar colors based on the trace element compositions to a 95% C.I. This does not pertain to duplicate lipstick samples of the same brand and color. Lipsticks from the Dark Brown color group were distinguishable to an 80% C.I. due to larger trace element composition variability in the Dark Brown 1a and 1b samples (Fig. 9).

Duplicate lipstick samples of the same brand and color are not distinguishable from one another based on trace element composition. Mass spectra acquired from all sections of the duplicate lipstick samples cluster together in score space on the PCA scores plots (Figs. 4, 7-9). The top, middle, and bottom sections from a given lipstick sample of the same brand and color are indistinguishable from one another in trace element composition. Duplicate lipstick samples of the same brand and color in this experiment are also indistinguishable based on trace element composition.

No significant difference in distinguishability between lipstick samples, or homogeneity within a single lipstick sample, was observed between the new and used lipstick samples. Replicate mass spectra from the top section of lipstick sample Red 2 (labeled Red 2T) do not cluster in the same PCA score space as the mass spectra from the middle (Red 2M) and bottom (Red 2B) sections of lipstick sample Red 2 (Fig. 2). The variation in the top section is due to an approximately 200 fold increase in bismuth concentration compared to the smears of the middle and bottom sections of lipstick.

This increase in bismuth may be due to contamination on the top section of lipstick since it was a used sample.

Variations in signal not attributed to changes in trace element composition were accounted for in this work. Mass spectra were normalized to the maximum signal to account for variations in the amount of lipstick ablated a) between replicate measurements of the same lipstick section, or b) between separate lipstick samples. Signal drift is also corrected for when the mass spectra are normalized to the maximum signal. All lipstick samples within a color group were analyzed on the same day to eliminate any day to day variation in laser and plasma conditions.

Conclusions

In this initial study, little variation in trace element composition throughout a lipstick sample was observed, showing that lipstick samples were homogeneous. All lipstick samples of different brands or colors are distinguishable from lipstick samples of similar colors based on their trace element compositions in a PCA scores plot. Duplicate lipstick samples of the same brand and color in this experiment are not distinguishable based on trace element composition. Contamination on the top section of a lipstick sample should be considered when analyzing used lipstick samples.

In forensic applications this method could assist in the identification of the brand and color of an unknown lipstick sample recovered at a crime scene by distinguishing the unknown sample from known lipstick samples based on trace element composition. The laser ablation method is quick and most of the sample remains intact for subsequent studies which is advantageous in forensic work.

Future analyses of lipstick samples should include the comparison of a new lipstick sample to a used lipstick sample of the same brand and color. More lipstick samples should be analyzed to determine if larger sample sizes may be distinguished from one another based on trace element composition. Larger sample sizes could also be used to determine an accurate statistical probability that two lipstick samples of similar color may be distinguished based on trace element composition. The effects of trace elements in underlying substrates, such as clothing and skin, should also be investigated. Eventually, databases containing trace elemental compositions of lipsticks may be created. This database could assist in identification of an unknown lipstick sample by distinguishing the unknown lipstick sample recovered at crime scenes from known samples in the database.

Acknowledgments

Research at the Ames Laboratory was supported by the National Institute of Justice (Award No. 2009-DN-R-112). The authors thank Dr. Stanley J. Bajic for guidance in PCA. The Ames Laboratory is operated for the U.S. Department of Energy by Iowa State University under Contract No. DEAC02-07CH11358.

References

1. López-López M, Özbek N, García-Ruiz C. Confocal raman spectroscopy to trace lipsick with their smudges on different surfaces. Talanta 2014;123:135-139.
2. Ehara Y, Marumo Y. Identification of lipstick smears by fluorescence observation and purge-and-trap gas chromatography. Forensic Sci Int 1998;96:1-10.
3. Lim bin Abdullah AF, Marimuthu Y, Haw CK, Mohamad Said NF, Nik Hassan NF, Yaacob MH at al. Forensic discrimination of lipsticks by thin layer chromatography and gas chromatography-mass spectrometry. Malay J Forensic Sci 2011;2(1):22-28.

4. Russell LW, Welch AE. Analysis of lipsticks. Forensic Sci. Int 1984;25:105-116.
5. Thornton JI, Casale PJ. Visualization of dyes on thin-layer chromatography plates by means of the argon ion laser. Forensic Sci Int 1979;14:215-219.
6. Engebretson A. Forensic lipstick analysis using chemical fingerprinting via gas chromatography. 233rd ACS Nation Meeting, Chicago, 2007.
7. Reuland DJ, Trinler WA. Comparison of lipstick smears by high performance liquid chromatography. part II. the effects of wear-time and subject on the chromatograms. J Forensic Sci Soc 1984;24(5):509-518.
8. Andrasko J. Forensic analysis of lipsticks. Forensic Sci Int 1981;17:235-251.
9. Choudhry MY. Comparison of minute smears of lipstick by microspectrophotometry and scanning electron microscopy/energy-dispersive spectroscopy. J Forensic Sci 1991;36(2):366-375.
10. Gardner P, Bertino MF, Weimer R, Hazelrigg E. Analysis of lipsticks using raman spectroscopy. Forensic Sci Int 2013;232:67-72.
11. Salahioglu F, Went MJ. Differentation of lipsticks by raman spectroscopy. Forensic Sci Int 2012;223:148-152.
12 Rodger C, Rutherford V, Broughton D, White PC, Smith WE. The in-situ analysis of lipsticks by surface enhanced resonance raman scattering. Analyst 1998;123:1823-1826.
13. Rodrigues Soares A, Nascentes CC. Development of a simple method for the determination of lead in lipstick using alkaline solubilization and graphite furnace atomic absorption spectrometry. Talanta 2013;105:272-277.
14. Gunduz S, Akman S. Investigation of lead contents in lipsticks by solid sampling high resolution continuum source electrothermal atomic absorption spectrometry. Regul Tox Pharm 2013;65(1):34-37.
15. Al-Saleh I, Al-Enazi S. Trace metals in lipsticks. Toxicol Environ Chem 2011;93(6):1149-1165.
16. Al-Saleh I, Al-Enazi S, Shinwari N. Assessment of lead in cosmetic products. Regul Tox Pharm 2009;54:105-113.
17. Gondal MA, Seddigi ZS, Nasr MM, Gondal B. Spectroscopic detection of health hazardous contaminants in lipstick using laser induced breakdown spectroscopy. J Hazard Mater 2010;175:726-732.
18. Lee S, Jeong H, Chang I. Simultaneous determination of heavy metals in cosmetic products. J Cosmet Sci 2008;59:441-448.
19. Misra G, Mittal VK. Neutron activation analysis of lipsticks using gamma-ray spectrometry. J Appl Spectrosc 2004;71(2):270-274.
20. Piccinini P, Piecha M, Torrent SF. European survey on the content of lead in lip products. J. Pharnaceut Biomed 2013;76:225-233.
21. Atkins P. Analysis of lipstick for toxic elements using ICP-MS. SPEX CertiPrep, Metuchen, 2012.

22. Hepp N. Determination of total lead in 400 lipsticks on the U.S. market using a validated mircrowave-assisted digestion, inductively coupled plasma-mass spectrometric method. J Cosmet Sci 2012;63:159-176.
23. Watling JR, Lynch B, Herring D. Use of laser ablation inductively coupled plasma mass spectrometry for fingerprinting scene of crime evidence. J Anal Atom Spectrom 1997;12:195-203.
24. Watling JR. Sourcing the provenance of cannabis crops using inter-element association patterns 'fingerprinting' and laser ablation inductively coupled plasma mass spectrometry. J Anal At Spectrom 1998;13:917-926.
25. Bajic S, Aeschliman D, Saetveit N, Baldwin D, Houk RS. Analysis of glass fragments by laser ablation-inductively coupled plasma-mass spectrometry and principal component analysis. J Forensic Sci 2005;50:1123-1127.
26. Suzuki Y, Kikkawa HS, Kasamatsu M, Higashikawa Y, Suzuki S. Forensic discrimination of sheet glass exposed to high temperature by the determination of trace impurities using ICP-MS. Anal Sci 2008;24:745-749.
27. Naes B, Umpierrez S, Ryland S, Barnett C, Almirall J. A comparison of laser ablation inductively coupled plasma mass spectrometry, micro x-ray fluorescence spectroscopy, and laser induced breakdown spectroscopy for the discrimination of automotive glass. Spectrochimica Acta Part B: Atom Spec 2008;63:1145-1150.
28. Guillong M, Gunther D. Quasi "non-destructive" laser ablation-inductively coupled plasma-mass spectrometry fingerprinting of sapphires. Spectrochimica Acta Part B: Atom Spec 2001;56B:1219-1231.
29. Watling JR, Herbert HK, Barrow IS, Thomas AG. Analysis of diamonds and indicator minerals for diamond exploration by laser ablation-inductively coupled plasma mass spectrometry. Analyst 1995;120:1357-1364.
30. Arroyo L, Trejos T, Hosick T, Machemer S, Almirall J, Gardinali P. Analysis of soils and sediments by laser ablation inductively coupled plasma mass spectrometry (LA-ICP-MS): an innovative tool for enviromental forensics. Environ Forensics 2010;11:315-327.
31. Deconinck I, Latkoczy C, Günther D, Govaert F, Vanhaecke F. Capabilities of laser ablation-inductively coupled plasma mass spectrometry for (trace) element analysis of car paints for forensic purposes. J Anal At Spectrom 2006;21:279-287.
32. Watling JR, Herbert H, Delev D, Abell ID. Gold fingerprinting by laser ablation inductively coupled plasma mass spectrometry. Spectrochimica Acta Part B: Atom Spec 1994;49B:205-219.
33. Bartle E, Watling JR. Provenance determination of oriental porcelain using laser ablation-inductively coupled plasma-mass spectrometry. J of Forensic Sci 2007;52:341-348.
34. Green R, Watling JR. Trace element fingerprinting of australian ocher using laser ablation inductively coupled plasma-mass spectrometry (LA-ICP-MS) for the provenance establishment and authentication of indigenous art. J of Forensic Sci 2007;52:851-859.

35. Aeschliman D, Bajic S, Baldwin D, Houk RS. Multivariate pattern matching of trace elements in solids by laser ablation-inductively coupled plasma-mass spectrometry: source attribution and preliminary diagnosis of fractionation. Anal Chem 2004;76:3119-3125.

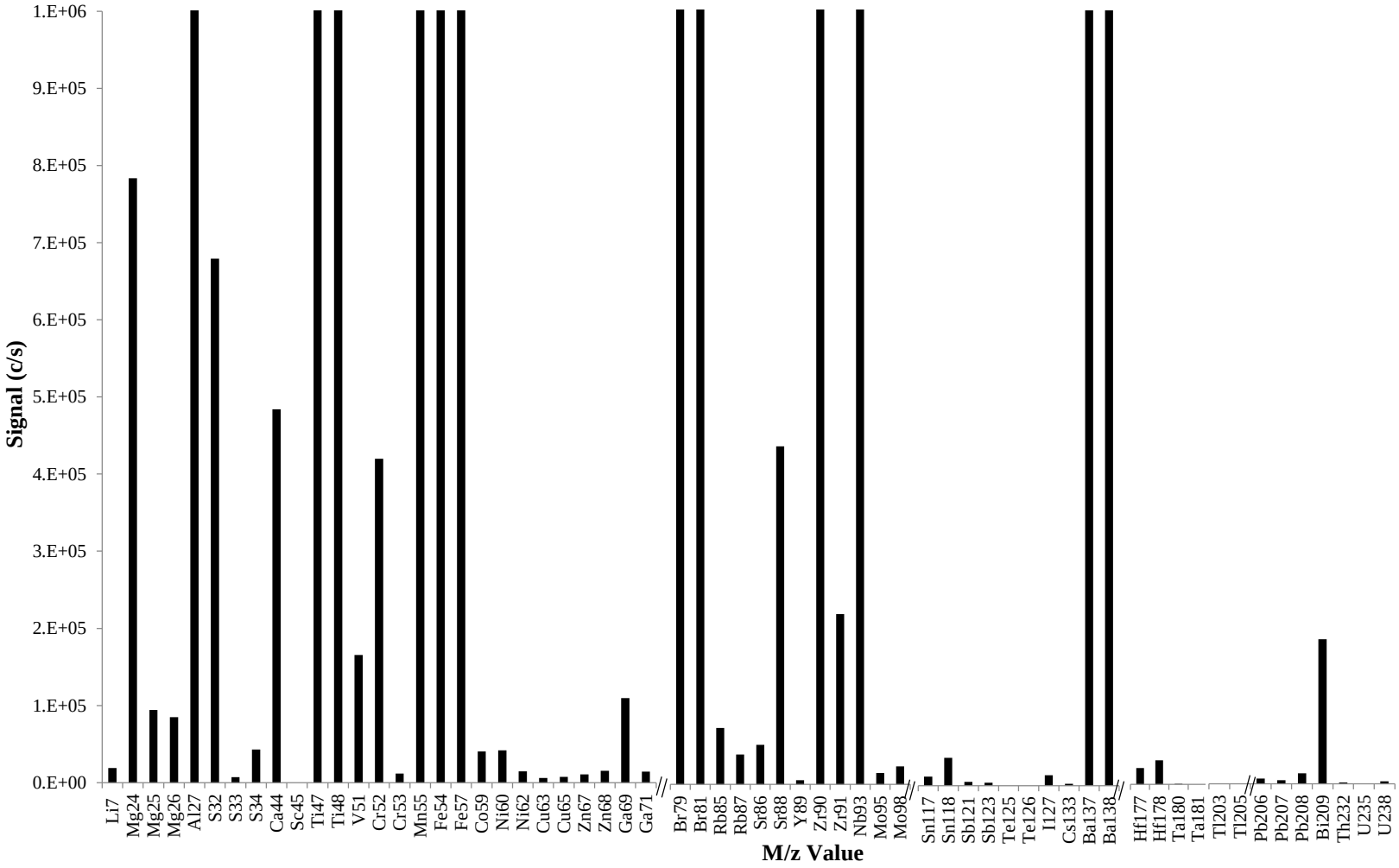

FIG. 1 – Multi elemental mass spectrum from lipstick sample Red 1. All isotopes of many elements are not shown and some were not measured. Several other analyte elements are observed in expected isotope ratios, i.e. Mg and Pb. The y-axis maximum is set to $1x10^6$ c/s and element which were not present in the lipstick sample were removed from the x-axis for easier viewing purposes.

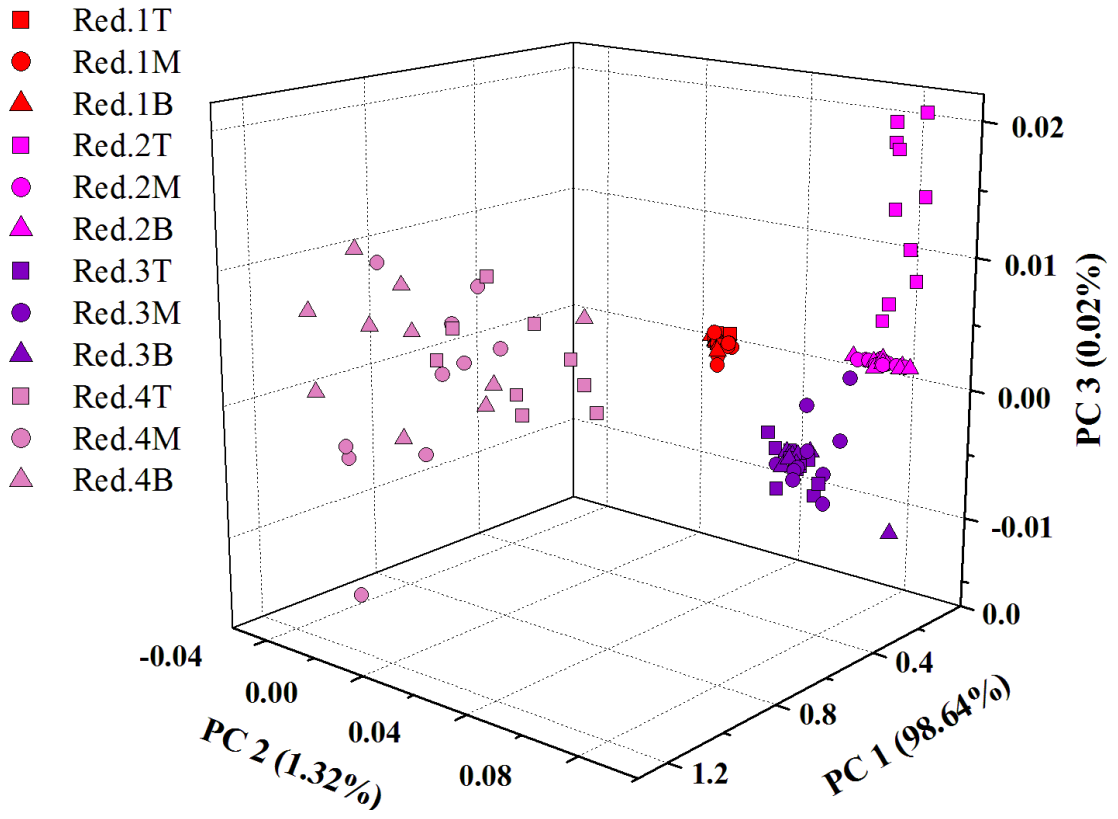

FIG. 2 – PCA scores plot from mass spectra of "Red" lipstick smears. Three sections of each lipstick sample, the top (T), middle (M), and bottom (B) cluster together and are indistinguishable. Different lipstick samples cluster separately from one another in score space, indicating that the lipstick samples are distinguishable.

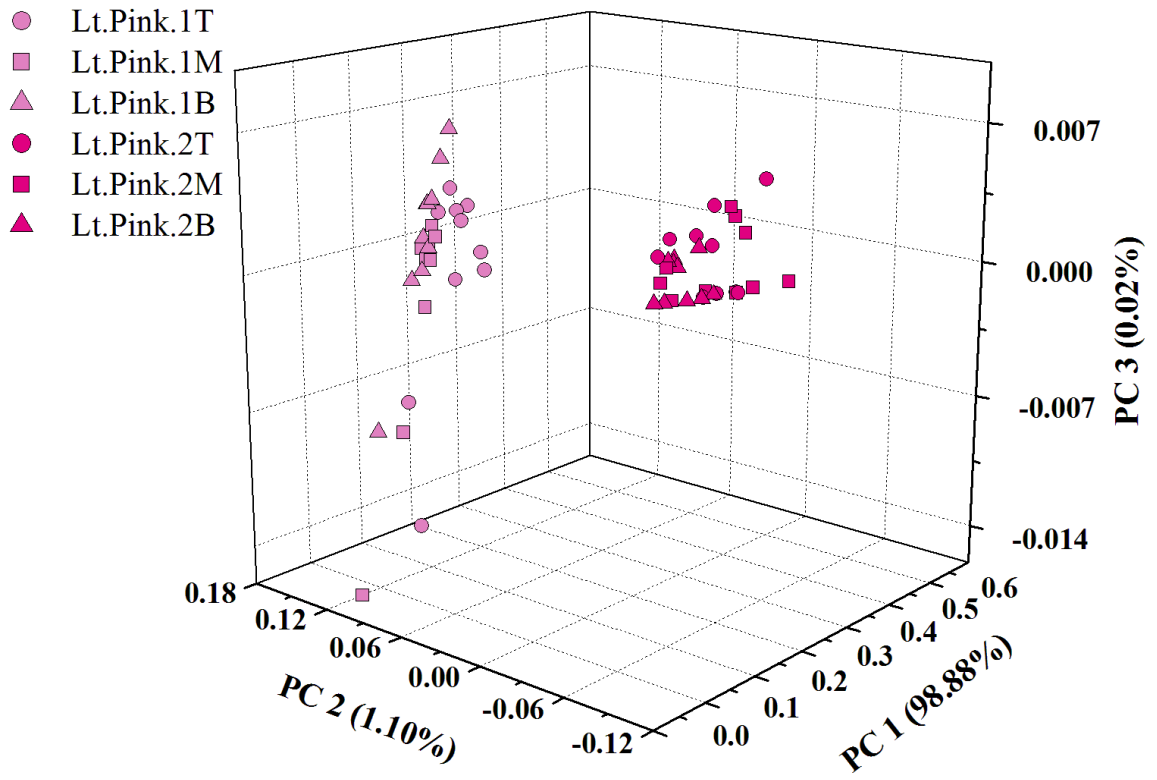

FIG. 3 – PCA scores plot from mass spectra of "Light Pink" lipstick smears. Three sections of each lipstick sample, the top (T), middle (M), and bottom (B), cluster together and are indistinguishable. Different lipstick samples cluster separately from one another in score space, indicating that the lipstick samples are distinguishable.

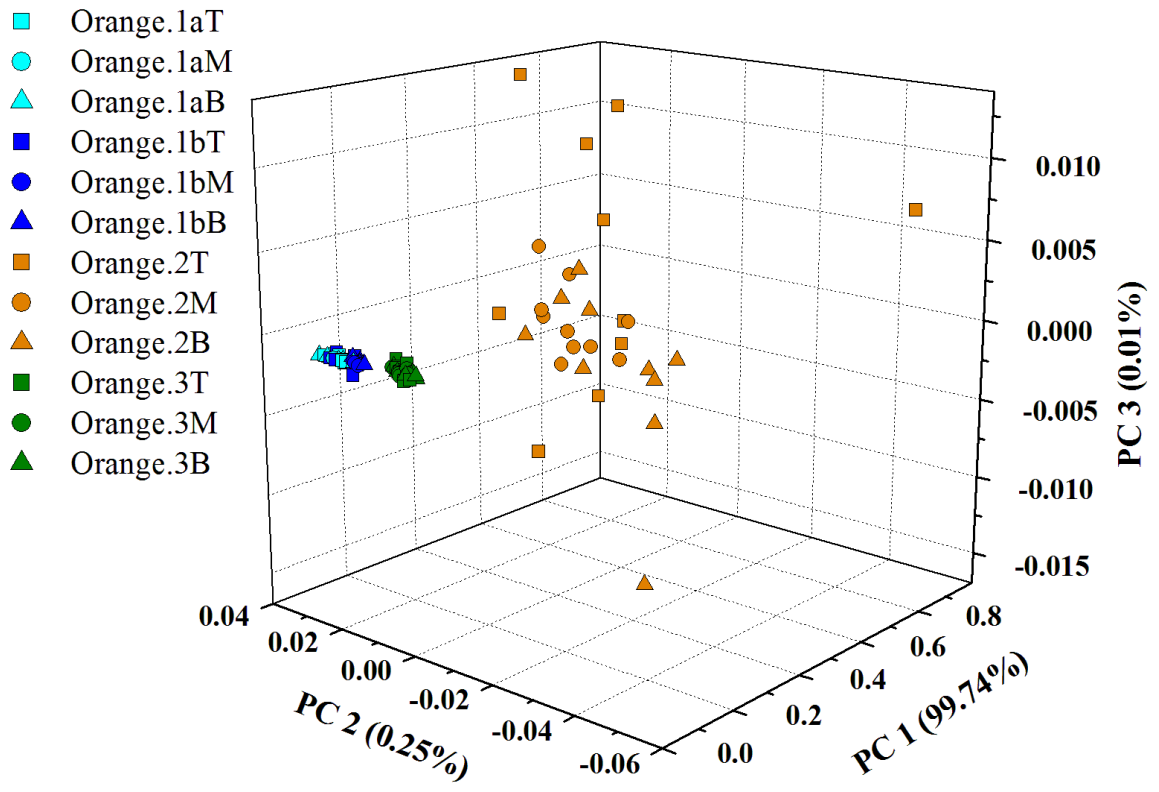

FIG. 4 – PCA scores plot from mass spectra of "Orange" lipstick smears. Three sections of each lipstick sample, the top (T), middle (M), and bottom (B) cluster together and are indistinguishable. Different lipstick samples cluster separately from one another in score space, indicating that the lipstick samples are distinguishable.

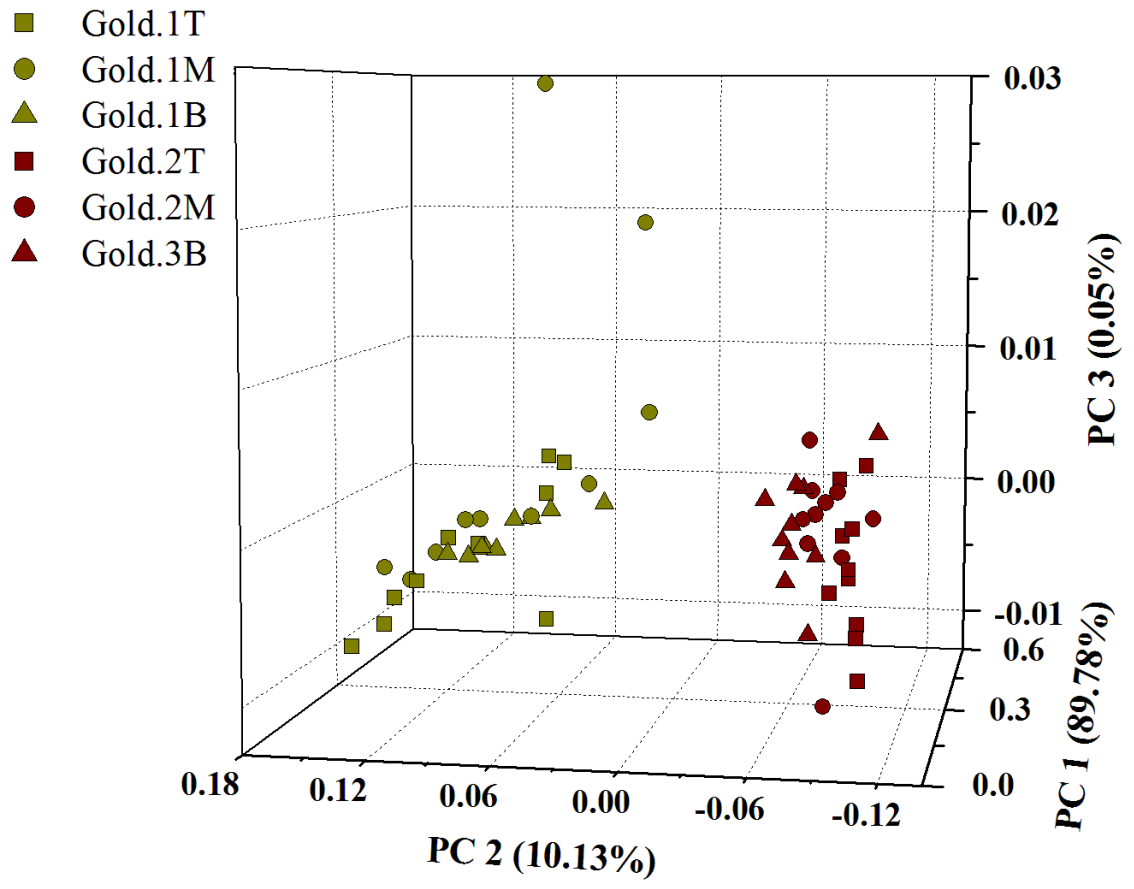

FIG. 5 – PCA scores plot from mass spectra of "Gold" lipstick smears. Three sections of each lipstick sample, the top (T), middle (M), and bottom (B) cluster together and are indistinguishable. Different lipstick samples cluster separately from one another in score space, indicating that the lipstick samples are distinguishable.

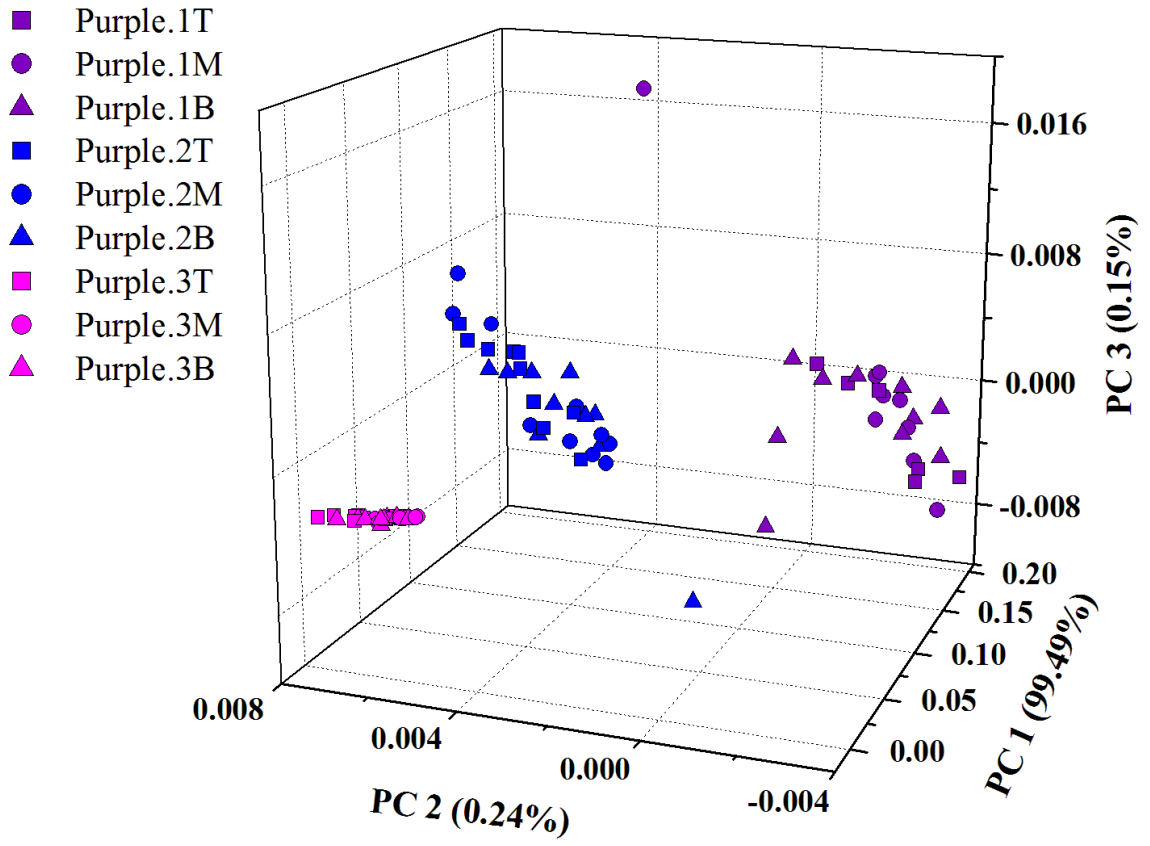

FIG. 6 – PCA scores plot from mass spectra of "Purple" lipstick smears. Three sections of each lipstick sample, the top (T), middle (M), and bottom (B) cluster together and are indistinguishable. Different lipstick samples cluster separately from one another in score space, indicating that the lipstick samples are distinguishable.

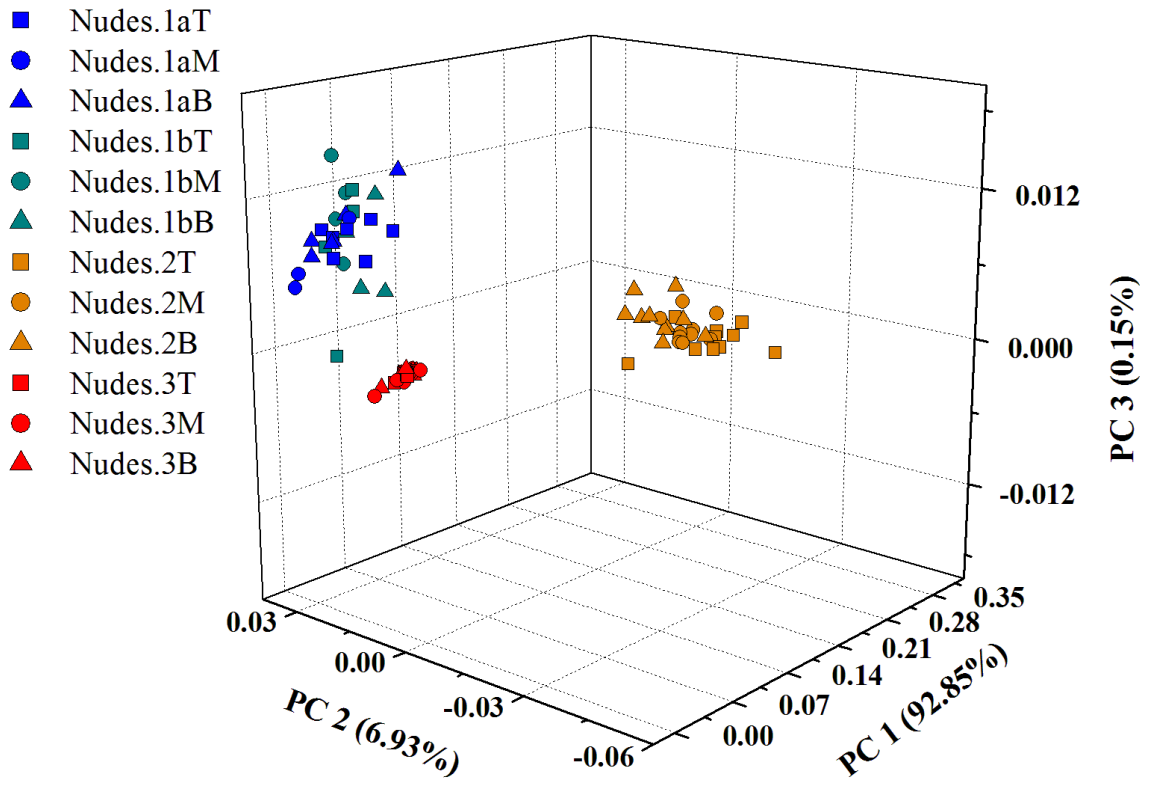

FIG. 7 – PCA scores plot from mass spectra of "Nude" lipstick smears. Three sections of each lipstick sample, the top (T), middle (M), and bottom (B) cluster together and are indistinguishable. Different lipstick samples cluster separately from one another in score space, indicating that the lipstick samples are distinguishable.

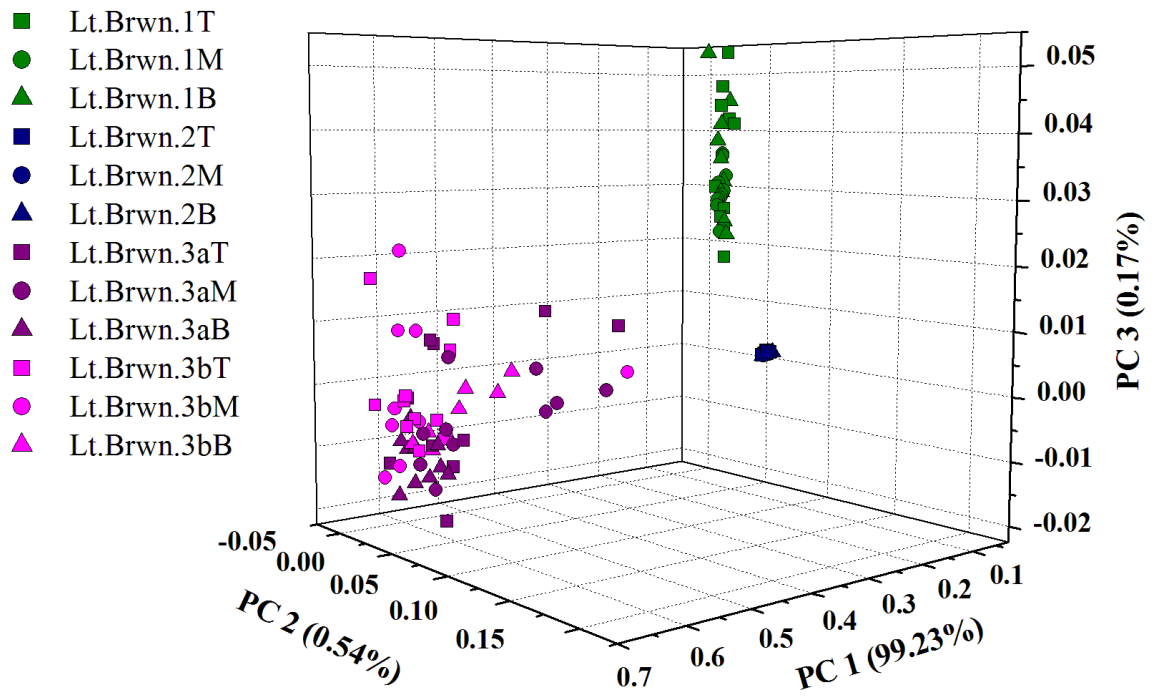

FIG. 8 – PCA scores plot from mass spectra of "Light Brown" lipstick smears. Three sections of each lipstick sample, the top (T), middle (M), and bottom (B) cluster together and are indistinguishable. Different lipstick samples cluster separately from one another in score space, indicating that the lipstick samples are distinguishable.

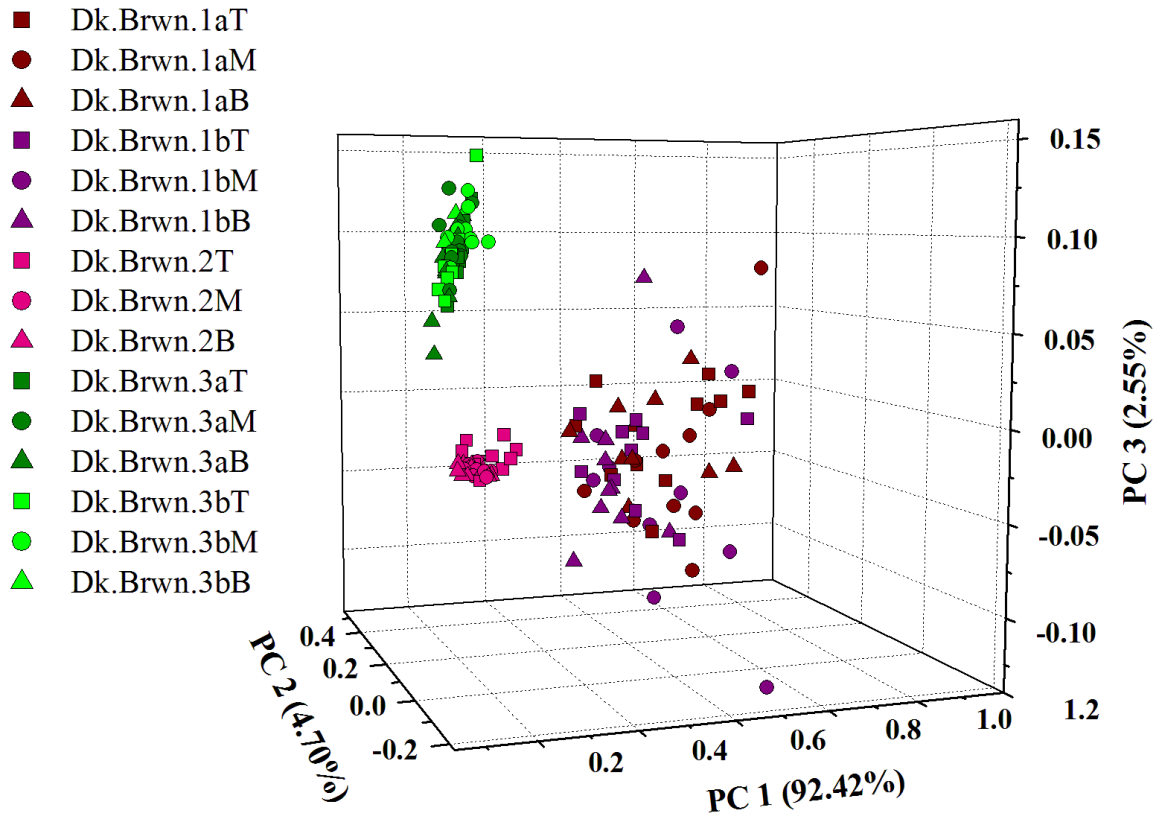

FIG. 9 – PCA scores plot from mass spectra of "Dark Brown" lipstick smears. Three sections of each lipstick sample, the top (T), middle (M), and bottom (B) cluster together and are indistinguishable. Different lipstick samples cluster separately from one another in score space, indicating that the lipstick samples are distinguishable.

TABLE 1 – Description of lipstick samples, the color groupings, and the isotope with the maximum signal that the signals from each lipstick section were normalized to. Lipstick samples with an "a" and "b" after the label are duplicates of the same brand and color.

Color Group	Label on Plots	Brand	Color	New/ Used	Section	Reference Isotope
Reds	Red.1T	Rimmel	Just So	Used	Top	$^{48}Ti^{+}$
	Red.1M	London			Middle	$^{48}Ti^{+}$
	Red.1B				Bottom	$^{48}Ti^{+}$
	Red.2T	Estée	Blazing	Used	Top	$^{48}Ti^{+}$
	Red.2M	Lauder	Berry		Middle	$^{48}Ti^{+}$
	Red.2B				Bottom	$^{48}Ti^{+}$
	Red.3T	L.A.	Berry Red	New	Top	$^{48}Ti^{+}$
	Red.3M	Colors			Middle	$^{48}Ti^{+}$
	Red.3B				Bottom	$^{48}Ti^{+}$
	Red.4T	Mary Kay	Amber	Used	Top	$^{138}Ba^{+}$
	Red.4M		Suede		Middle	$^{138}Ba^{+}$
	Red.4B				Bottom	$^{138}Ba^{+}$
Light Pinks	Lt.Pink.1T	Revlon	Heart	Used	Top	$^{209}Bi^{+}$
	Lt.Pink.1M		Warming		Middle	$^{209}Bi^{+}$
	Lt.Pink.1B				Bottom	$^{48}Ti^{+}$
	Lt.Pink.2T	Maybelline	Fushia	Used	Top	$^{48}Ti^{+}$
	Lt.Pink.2M		Blast		Middle	$^{48}Ti^{+}$
	Lt.Pink.2B				Bottom	$^{48}Ti^{+}$
Nudes	Nudes.1aT	L.A.	Satin	New	Top	$^{48}Ti^{+}$
	Nudes.1aM	Colors			Middle	$^{48}Ti^{+}$
	Nudes.1aB				Bottom	$^{48}Ti^{+}$
	Nudes.1bT	L.A.	Satin	New	Top	$^{48}Ti^{+}$
	Nudes.1bM	Colors			Middle	$^{48}Ti^{+}$
	Nudes.1bB				Bottom	$^{48}Ti^{+}$
	Nudes.2T	L'Oréal	Crystallized	Used	Top	$^{48}Ti^{+}$
	Nudes.2M		Coral		Middle	$^{48}Ti^{+}$
	Nudes.2B				Bottom	$^{48}Ti^{+}$
	Nudes.3T	CoverGirl	Pillow Pink	Used	Top	$^{48}Ti^{+}$
	Nudes.3M				Middle	$^{48}Ti^{+}$
	Nudes.3B				Bottom	$^{48}Ti^{+}$

TABLE 1 continued – Description of lipstick samples, the color groupings, and the isotope with the maximum signal that the signals from each lipstick section were normalized to. Lipstick samples with an "a" and "b" after the label are duplicates of the same brand and color.

Color Group	Label on Plots	Brand	Color	New/ Used	Section	Reference Isotope
Oranges	Orange.1aT	Milani	Mandrina	New	Top	$^{48}Ti^{+}$
	Orange.1aM				Middle	$^{48}Ti^{+}$
	Orange.1aB				Bottom	$^{48}Ti^{+}$
	Orange.1bT	Milani	Mandrina	New	Top	$^{48}Ti^{+}$
	Orange.1bM				Middle	$^{48}Ti^{+}$
	Orange.1bB				Bottom	$^{48}Ti^{+}$
	Orange.2T	Revlon	Strawberry	Used	Top	$^{48}Ti^{+}$
	Orange.2M		Suede		Middle	$^{48}Ti^{+}$
	Orange.2B				Bottom	$^{48}Ti^{+}$
	Orange.3T	Jafra	Chilled	Used	Top	$^{209}Bi^{+}$
	Orange.3M		Peach		Middle	$^{209}Bi^{+}$
	Orange.3B				Bottom	$^{209}Bi^{+}$
Golds	Gold.1T	Fashion	Forever	Used	Top	$^{48}Ti^{+}$
	Gold.1M	Fair	Gold		Middle	$^{48}Ti^{+}$
	Gold.1B				Bottom	$^{48}Ti^{+}$
	Gold.2T	Chanel	Pink	Used	Top	$^{48}Ti^{+}$
	Gold.2M		Sugar		Middle	$^{48}Ti^{+}$
	Gold.2B				Bottom	$^{48}Ti^{+}$
Purples	Purple.1T	Mary Kay	Rich Fig	Used	Top	$^{27}Al^{+}$
	Purple.1M				Middle	$^{27}Al^{+}$
	Purple.1B				Bottom	$^{27}Al^{+}$
	Purple.2T	L.A.	Berry Ice	New	Top	$^{138}Ba^{+}$
	Purple.2M	Colors			Middle	$^{138}Ba^{+}$
	Purple.2B				Bottom	$^{138}Ba^{+}$
	Purple.3T	L.A.	Luscious	New	Top	$^{138}Ba^{+}$
	Purple.3M	Colors	Wine		Middle	$^{48}Ti^{+}$
	Purple.3B				Bottom	$^{138}Ba^{+}$
Light Browns	Lt.Brwn.1T	L'Oréal	Iced Latte	Used	Top	$^{48}Ti^{+}$
	Lt.Brwn.1M				Middle	$^{48}Ti^{+}$
	Lt.Brwn.1B				Bottom	$^{48}Ti^{+}$
	Lt.Brwn.2T	Benefit	Lana	Used	Top	$^{48}Ti^{+}$
	Lt.Brwn.2M				Middle	$^{48}Ti^{+}$
	Lt.Brwn.2B				Bottom	$^{48}Ti^{+}$
	Lt.Brwn.3aT	New York	Plum Rum	New	Top	$^{48}Ti^{+}$
	Lt.Brwn.3aM	Color			Middle	$^{48}Ti^{+}$
	Lt.Brwn.3aB				Bottom	$^{48}Ti^{+}$
	Lt.Brwn.3bT	New York	Plum Rum	New	Top	$^{48}Ti^{+}$
	Lt.Brwn.3bM	Color			Middle	$^{48}Ti^{+}$
	Lt.Brwn.3bB				Bottom	$^{48}Ti^{+}$

TABLE 1 continued – Description of lipstick samples, the color groupings, and the isotope with the maximum signal that the signals from each lipstick section were normalized to. Lipstick samples with an "a" and "b" after the label are duplicates of the same brand and color.

Color Group	Label on Plots	Brand	Color	New/ Used	Section	Reference Isotope
Dark Browns	Dk.Brwn.1aT	L.A. Colors	Cocoa Shimmer	New	Top	$^{48}Ti^{+}$
	Dk.Brwn.1aM				Middle	$^{48}Ti^{+}$
	Dk.Brwn.1aB				Bottom	$^{48}Ti^{+}$
	Dk.Brwn.1bT	L.A. Colors	Cocoa Shimmer	New	Top	$^{48}Ti^{+}$
	Dk.Brwn.1bM				Middle	$^{48}Ti^{+}$
	Dk.Brwn.1bB				Bottom	$^{48}Ti^{+}$
	Dk.Brwn.2T	MAC	Frost Spanish Fly	Used	Top	$^{48}Ti^{+}$
	Dk.Brwn.2M				Middle	$^{48}Ti^{+}$
	Dk.Brwn.2B				Bottom	$^{48}Ti^{+}$
	Dk.Brwn.3aT	L.A. Colors	Frozen Berries	New	Top	$^{48}Ti^{+}$
	Dk.Brwn.3aM				Middle	$^{48}Ti^{+}$
	Dk.Brwn.3aB				Bottom	$^{48}Ti^{+}$
	Dk.Brwn.3bT	L.A. Colors	Frozen Berries	New	Top	$^{48}Ti^{+}$
	Dk.Brwn.3bM				Middle	$^{48}Ti^{+}$
	Dk.Brwn.3bB				Bottom	$^{48}Ti^{+}$

TABLE 2—Instrument and laser parameters for the analysis of lipstick smears

Outer gas flow	18.0 L Ar min^{-1}
Auxiliary flow	1.80 L Ar min^{-1}
Sheath flow	0.30 L Ar min^{-1}
Sampler and skimmer cones	Ni and Ni, CRI configuration (Analytik Jena)
Scan mode	Peak hopping
Dwell time	10 ms
RF Power	1400 W
Torch position, ion optics	Optimized for maximum sensitivity and stability
100 fs Laser	Coherent Libra Ti:Sapphire
Operational wavelength	266 nm
Laser energy	130 mW $pulse^{-1}$; Filtered to 17 mW $pulse^{-1}$
Frequency	1000 Hz
Spot size	~70 µm
Raster speed	450 µm sec^{-1}
Carrier gas flow rate through ablation cell	0.99-1.00 L Ar min^{-1}

TABLE 3 – List of isotope m/z values measured during ablation of lipstick smears in the Distinguishability and Homogeneity of Lipsticks experiment. Selected elements are present in at least one of the lipstick samples.

$^{7}Li^{+}$, $^{25}Mg^{+}$, $^{26}Mg^{+}$, $^{27}Al^{+}$, $^{45}Sc^{+}$, $^{47}Ti^{+}$, $^{48}Ti^{+}$, $^{51}V^{+}$, $^{55}Mn^{+}$, $^{54}Fe^{+}$, $^{57}Fe^{+}$, $^{59}Co^{+}$, $^{70}Ge^{+}$, $^{74}Ge^{+}$, $^{79}Br^{+}$, $^{80}Br^{+}$, $^{89}Y^{+}$, $^{90}Zr^{+}$, $^{91}Zr^{+}$, $^{93}Nb^{+}$, $^{95}Mo^{+}$, $^{98}Mo^{+}$, $^{103}Rh^{+}$, $^{117}Sn^{+}$, $^{118}Sn^{+}$, $^{121}Sb^{+}$, $^{123}Sb^{+}$, $^{127}I^{+}$, $^{133}Cs^{+}$, $^{137}Ba^{+}$, $^{138}Ba^{+}$, $^{139}La^{+}$, $^{141}Pr^{+}$, $^{177}Hf^{+}$, $^{178}Hf^{+}$, $^{182}W^{+}$, $^{183}W^{+}$, $^{194}Pt^{+}$, $^{195}Pt^{+}$, $^{203}Tl^{+}$, $^{205}Tl^{+}$, $^{206}Pb^{+}$, $^{207}Pb^{+}$, $^{208}Pb^{+}$, $^{209}Bi^{+}$, $^{232}Th^{+}$, $^{235}U^{+}$, $^{238}U^{+}$

CHAPTER 3. SAMPLING AND SPATIAL HETEROGENEITY IN TRACE ELEMENTAL ANALYSIS OF COPPER WIRE FOR FORENSIC COMPARISONS BY LASER ABLATION-INDUCTIVELY COUPLED PLASMA-MASS SPECTROMETRY

Jonna Berry, Stanley J. Bajic and R. S. Houk

Abstract

The objective of this work is to assess the forensic value of copper wire strands for pairwise comparison based on trace elemental composition. The bulk of the work is done without sample dissolution using laser ablation (LA)-inductively coupled plasma-mass spectrometry (ICP-MS) Numerous strands of varying lengths from a multi-strand speaker cable were analyzed. Multivariate statistical analysis was performed on the mass spectra to determine the compositional variability within a particular wire strand and between different strands. The copper wire strands in this study are spatially heterogeneous in trace element composition. The spatial variability in the trace elemental composition within a single strand of copper wire is similar to that between multiple strands. Examining spatially resolved data is important to determine the variations in elemental composition within a sample. In actual forensic applications, the possibility of spatial heterogeneity must be considered, especially in cases where only small samples (e.g., copper wire fragments after an explosion) are available.

Introduction

Inductively coupled plasma-mass spectrometry (ICP-MS) offers the potential for a highly sensitive, relatively non-destructive, rapid, and cost effective analysis of small

samples for identification and comparison of forensic evidence (1, 2). Trace and ultratrace elemental analysis by ICP-MS has been used to determine if samples are similar to or distinguishable from one another. This technique has been used to compare various samples of steel and glass, including float, container, sheet, and automotive glass, for forensic analysis (1, 3, 4, 5).

For analysis of solids by ICP-MS, there are two common options. Dissolving the sample yields better precision and is more easily calibrated but can be cumbersome and does destroy the original piece of evidence. Thus, the speed, convenience, and limited sample destruction of LA sampling is an advantageous feature for forensic work. LA-ICP-MS has been used to distinguish between gold samples and also to determine their provenance (6). Other samples such as gemstones, soils, and car paints have also been distinguished based on trace elemental composition measured with LA-ICP-MS (7, 8, 9, 10). The provenance has been determined for samples such as cannabis crops, oriental porcelain, and ochers as well, using LA-ICP-MS to measure trace elemental composition (2, 11, 12).

However, not all forensic samples can be clearly distinguished from each other based on trace elemental composition using LA-ICP-MS. In a nationally-prominent example, detailed investigation into compositional analysis of bullet lead by the Federal Bureau of Investigation (FBI) and the National Research Council (NRC) indicated many problems with the use of trace element composition for forensic comparison of lead bullets (13). Anywhere from 12,000 up to 35 million bullets for a 40-grain .22 caliber long rifle may be produced from “compositionally indistinguishable volumes of lead” (CIVL). Many bullet manufacturers also add scrap lead from the bullet production to melt at random times, which sporadically changes the composition of the original melt (13).

One recent development in LA-ICP-MS is the use of femtosecond lasers. Femtosecond lasers create finer particulates which lead to an increase in signal intensity and stability, and narrower confidence intervals for determining unknown concentrations compared to a nanosecond laser, particularly when ablating solid metal targets (14, 15, 16). A decrease in deposition around the ablation pit, an increase in signal intensities, and an improvement in the limit of detection are often observed when helium is used as the carrier gas through the ablation cell compared to argon (17, 18). A femtosecond laser with helium as the carrier gas through the ablation cell coupled to the ICP-MS can provide accurate measurements of trace elements with high sensitivity and selectivity.

Data analysis methodology is also important in forensic analysis. One simple yet valuable chemometric method is principal component analysis (PCA), which reduces multivariate data into a two- or three-dimensional scores plot. The scores plot depicts most of the variation within a data set. PCA has been proven to be a useful, efficient, and reproducible technique for the comparison of forensic samples by trace elemental composition with LA-ICP-MS (3, 9, 12, 19).

Speaker cable, typically composed of multiple strands of copper wire, is commonly used for binding or strangling victims and is often left at crime scenes. Fragments may also be recovered from electronic circuits or components after a bomb explosion. Comparison of one or more copper wire strands found at a crime scene to those found in the possession of a suspect could be used as evidence to link the suspect to the scene of the crime.

In the present work, preliminary experiments determined that individual strands of copper wire had quite different trace elemental compositions; all such strands could apparently be distinguished from one another easily (19). This initial study formed the

basis of the present work. The spatial variability of the elemental composition of the copper wire strands was further investigated. Monster XP Compact High Performance Speaker Cable wire used in this study is high purity copper speaker wire (>99% copper) (20). Elemental impurities within the wire increase the electrical resistivity and decrease the conductivity through the cable. Therefore, high purity copper wire is used for speaker cable due to its high electrical conductivity and low atomic impurities. This work aimed to distinguish between individual high purity copper wire samples. If high purity samples were distinguishable, samples of lower purity would most likely be easily distinguished from one another as well.

A similar study by Dettman *et al.* (21) measured trace element concentrations in high-purity copper wire by solution ICP-MS. Dissolution destroys the sample which can be a disadvantage when analyzing forensic evidence. Larger gauge wire was used in this study (12 AWG) (21), whereas the present work analyzed 36 AWG high-purity copper wire. The present work provides a thorough investigation of the variability in trace element composition throughout high-purity copper wire typically used as speaker cable.

This paper illustrates an issue in sampling size of the strands for pairwise comparisons, which is caused by the spatial heterogeneity of the trace elemental composition within each copper strand. This spatial heterogeneity effect was verified by solution analysis. Dettman *et al.* observed similar trace element variations within ~ 20 m length of a larger copper wire by solution analysis (21).

Experimental

Samples

The sample was a single 30 m length of 65 stranded Monster XP Compact High Performance Speaker Cable wire. The linear polyethylene dielectric (LPE) insulation coating was peeled off the wire. Copper strands were unwound and unbraided from the original cable. In this paper, the term "wire" refers to the entire speaker cable, a bundle of copper strands intertwined together and covered with plastic insulation. A "strand" is a single copper thread removed from the insulation and unwound from the wire. A "segment" of a strand is a linear section from which one or multiple "sub-segments" (~ 9 cm long) of strand were removed for analysis (Fig. 1). The same ten copper strands were used in all experiments and are labeled accordingly as Strand 1 through 10.

LA-ICP-MS Analysis

An apparatus to pull the strands straight in the ablation cell was developed to allow for the focused laser beam to remain on the strand during the ablation. The strands were wound around two screw posts to keep them taut during ablation. The apparatus contained a maximum of ten copper wire strands for ablation at once. Each sub-segment of copper strand removed for analysis was ~ 9 cm long to allow for room to grasp the strand to mount it in the apparatus. Various 2 cm long sub-segments were actually ablated in the LA cell. The copper strands were 36 AWG and the diameter was approximately 120 μm.

Two types of laser ablation experiments are presented. The experiments are listed in order of the number of sub-segments per strand which were analyzed, not in the chronological order they were performed. In Experiment I, one sub-segment of three segments (A, B, and C) of nine copper strands was removed for analysis (Fig. 1a). In

Experiment II, four adjacent sub-segments of two segments (D and E) of ten copper strands were removed for analysis (Fig. 1b). Multiple laser ablation experiments were conducted, which all yielded similar results. The two laser ablation experiments presented in this paper provide a reasonable representation of the results from many such experiments done over the duration of the project.

In both experiments, the sub-segments were ablated with a femtosecond (fs) (Coherent Libra Ti:Sapphire 266 nm, Santa Clara, CA) laser in a single line scan pattern. Helium gas was used as the carrier gas through the ablation cell. The nominal spot size was ~70 μm. The laser removed most of the upper half of each circular wire, leaving the remaining strand with a semi-circular, D-shaped cross section.

The strands were suspended ~ 1 cm above a piece of Teflon so the edge of the laser that did not ablate the strand was defocused before it reached the Teflon piece. Argon was introduced into the sample tube after the ablation cell and before the torch via a Y setup. The elemental mass spectra were acquired using a magnetic sector ICP-MS (Element 1, Thermo Scientific Inc., Bremen Germany). All data were obtained in low resolution, $m/\Delta m \sim 300$. Plasma conditions were optimized with a nebulized tune solution for maximum and most stable signals (Table 1). In Experiment I, 45 mass spectra were measured per sub-segment of each strand. Signals for Ag, Bi, Cu, Pb, Sb, Sn, W, Zn and Zr were peak-area integrated and background subtracted. In Experiment II, 12 mass spectra per sub-segment were measured. Signals for the m/z values of Ag, Cu, Pb, Sb, Sn, Zn and Zr were peak-area integrated and background subtracted. In both experiments the background was measured with the laser on, but shuttered, and helium flowing through the ablation cell. Bi and W were added to the original list of elements in Experiment I after being detected in various dissolution samples of copper strands.

Measures were taken to account for various instrumental effects. Experiments I and II (described below) were each completed in a day (one day per experiment) in order to eliminate day-to-day plasma variations. A piece of standard NIST 610 glass was ablated with the fs laser and selected m/z values were measured at the beginning and end of each experiment and compared in order to monitor for instrument drift over time. Signals for the selected m/z values were normalized to the $^{63}Cu^{+}$ signal to correct for the variations in the amount of copper removed during ablation and to address possible problems caused by copper deposition on the cones. New background spectra were measured frequently. The new background spectrum was subtracted from the succeeding copper strand mass spectra.

Various laser ablation experiments, detailed below, were performed with the fs laser to eliminate possible sources of variations in trace element signals other than heterogeneity of the strand. One experiment assessed different methods of cleaning the strand before ablation. Strands were wiped with either a dry Kimwipe, or a Kimwipe wetted with deionized water, or ablated with the fs laser to remove the surface of the strand before the mass spectra were acquired. In order to remove the surface of the strand with the fs laser and retain a significant amount of strand for re-ablation, the raster speed was increased to 400 μm s^{-1} and the laser power was decreased to 34 mW. The raster speed and laser power were reset to the parameters listed in Table 1 when mass spectra were collected. The mass spectra from the cleaned strands were compared to mass spectra from strands where no cleaning was performed. There was no significant difference in the mass spectra between the cleaned strands and the strands which were not cleaned (data not shown).

Sample Dissolution Analysis

Signals during LA-ICP-MS are often erratic, even for spatially homogeneous samples. Therefore, several segments of copper strands were dissolved to determine whether LA alone caused the apparent spatial variations in elemental signals. Sample dissolution was used as a validation method for the LA-ICP-MS results. Three segments (F, G, and H) of nine copper wire strands were broken by hand (i.e. not cut with a metal object) every 12 to 15 m (Fig. 1c). Each segment of copper strand was weighed to ~0.025 g and dissolved in ~1 g of an acid solution of 20 percent hydrochloric acid and 20 percent nitric acid (2:1). Both acids were prepared by in-house sub-boiling distillation. The solution was diluted to ~500 ppm copper and 0.5 percent acid with 18 MΩ·cm Millipore water. Indium was added at ~ 4 ppb as an internal standard. Solutions were prepared in Teflon bottles which were vapor cleaned above 70 percent nitric acid for at least 16 hours. The solutions were introduced into the ICP-MS via a 400 µL nebulizer and an ESI Apex-Q desolvation device. The heater on the Apex was set to 100 ^{o}C and the chiller was set to 2 ^{o}C. Argon gas was used as the sample gas at 1.015 L min^{-1} into the ESI Apex-Q. Nitrogen gas was also applied to the Apex Q at ≤ 10 mL min^{-1} to increase signal and improve stability. Plasma conditions were optimized with a standard solution for maximum and most stable signals (Table 1). The signals for Ag, In, Sn, Sb, W, Pb, and Bi were acquired using a Thermo Scientific Element 1 ICP-MS. The background was measured with a blank of the 0.5 percent acid solution and Millipore water. Signals for the measured m/z values were peak-area integrated, background subtracted and corrected for the amount of copper strand dissolved and for the internal standard concentrations.

Data Analysis for Comparison of Strands

PCA reduces multivariate data into a simple, two- or three-dimensional scores plot which depicts most of the variation within the data set (22). The scores plot is composed of a set of axes called principal components (PCs). The PCs represent the major variance within the variables, in this case, net signals at selected m/z values, of a data set. A PCA scores plot allows for the visualization and interpretation of the samples in the data set for comparison to one another (19).

Data sets comprising multiple mass spectra from one, or multiple, sub- segments of a copper strand were used to produce a PCA scores plot. One such data set was selected as the model. Data sets from the other sub-segments were then compared to the model. The variance, or spread of results, from the data set to the model was determined by the Q-value. The Q-value is a measure of the difference, or residual, between the mass spectra of one data set to their projection onto the model in the PC scores plot (19). A large Q-value indicates the data sets differ extensively. In the same model, multiple Q-values of a data set are averaged together to simplify the plot and depict an overall point that represents the average Q-value for each copper strand. A 95% confidence interval (C.I.) is calculated from each model. If the average Q-value of a strand is larger than the Q-value of the 95% C.I. of the model, the copper strand is considered distinguishable from the model. Alternatively, if the average Q-value of a copper strand is smaller than the Q-value of the 95% C.I. of the model, the copper strand and the model are considered indistinguishable from one another to a 95% C.I.

To simplify the data, tables were created which list the strands that were indistinguishable from the PCA model based on the average Q-value of the strand and the 95% C.I. of the model. The strands that are not listed in a particular table were distinguishable from the model.

For laser ablation results, signals were normalized to the $^{63}Cu^{+}$ signal and the Cu signals were removed from the PCA analysis. For the dissolution results, signals were peak-area integrated, background subtracted and corrected for the amount of copper strand dissolved and for the internal standard concentrations. Cu and In signals were removed from the PCA analysis. Commercial PCA software, Solo Eigenvector version 6.5.1 was used. No other scaling or preprocessing was used before data were input into the PCA software.

Results and Discussion

Laser Ablation

Two sub-segments of a copper strand were ablated with the fs laser and all selected elements were measured by ICP-MS (Fig. 2). Seven elements with the largest signals that contained more than one isotope and minimum interferences were initially selected for experiments. The selected elements included Cu, Zn, Zr, Ag, Sn, Sb, and Pb. Examination of the various isotope ratios shows that all these signals are due to the actual atomic ions and are not polyatomic interferences.

Numerous experiments were also conducted on the copper strands using a nanosecond (ns) laser (LSX 500 Nd:YAG 266 nm, CETAC Technologies, Omaha NE). Results were similar with either laser; however, only the fs laser results are reported below. In particular, the spatial heterogeneity described below was of similar severity with either laser.

Experiment I: Pairwise Comparison of Segments A, B, and C Between Nine Copper Strands

Three segments (A, B, and C) per copper strand were ablated with the fs laser. The mass spectra from segment A of one strand are used as the model in an average Q-residual plot and compared to the mass spectra of segment A from the remaining strands. This comparison is repeated with segment A of each strand used as the PCA model. The Q-values from each mass spectrum were averaged together to represent the average Q-value for that strand. The strands which were indistinguishable from the PCA model (average Q-value was lower than the Q-value from the 95% C.I. of the model) in the average Q-residual plot are listed in Table 2. Most of the strands are distinguishable from one another in the pairwise comparisons, in agreement with the previous observations using both LA (19) and solution analysis (21). There are only six total indistinguishable pairwise comparisons when the mass spectra from one sub-segment of segment A are used as the model for comparisons (Table 2). Results are similar when the mass spectra from the single sub-segments of segment B and C are used as the models (data not shown).

Next, the mass spectra from the sub-segments of segments A, B, and C of a strand were combined and used as the model. The mass spectra from the three segments of the remaining strands are compared to the model. The Q-values from the three sub-segments

in each strand were averaged together to represent the average Q-residual for a strand. The strands which were indistinguishable from the new model are listed in Table 3. When the distance over which the copper strand is analyzed increases from one sub-segment to three sub-segments, the total number of indistinguishable pairwise comparisons increases to eight. Note that in Table 3, Strand 8 is indistinguishable from six of the models. This is because the compositional variability within the mass spectra of the segments in Strand 8 is smaller than the variability within most of the other strands in this experiment. This is explained in more detail at the end of the Results/ Discussion section.

Experiment I: Pairwise Comparison of Sub-Segments within an Individual Strand

Based on the previous results, many of the copper strands seem to be distinguishable from one another based on trace elemental composition (19). However, this judgment is based on analysis of only small sub-segments of the strands. The mass spectra of one segment are compared to the mass spectra from the remaining segments within the same strand in an average Q-residual plot (Fig. 3). If the average Q-value of a strand is larger than the Q-value of the 95% C.I. of the model, the copper strand is considered distinguishable from the model. Alternatively, if the average Q-value of a copper strand is smaller than the Q-value of the 95% C.I. of the model, the copper strand and the model are considered indistinguishable from one another to a 95% C.I.

Figure 3 shows that different segments of the same strand are also distinguishable from one another. The differences between the segments within the same strand are of similar magnitude as the difference between strands in the previous average Q-residual plots. The results from the segments not shown in the graph are also distinguishable from one another within the same strand; they are omitted merely to simplify the plot.

Signals for each element measured during laser ablation were plotted versus distance over which the strand was ablated (Fig. 4). Signal spikes are mainly due to actual spatial variations in the trace elemental composition within the 2 cm long copper strand (Fig. 4). The laser ablated the 2 cm piece of copper strand over 4.5 minutes while the ICP-MS hopped through the selected m/z values. The large spikes in element signal persist over 10 s or more of the analysis and are not merely due to large, transient particles entering the plasma. This instrument measures the various elements sequentially. A small time lapse occurs between isotope measurements as the magnetic field and accelerating voltage are changed to transmit a different m/z value. Considering the small time lapse, many of the trace elements do not occur together throughout the strand. It appears that certain elements, especially Sn (Fig. 4), are present mainly in discrete grains or inclusions and are not distributed homogeneously.

These results indicate that the spatial variability of the trace elemental composition throughout a copper strand is similar to the variability between different strands of a speaker wire. Trace element data are easily collected over a small spatial section by laser ablation. Examination of time resolved isotope signals over a length of a sample is useful to assess the heterogeneity of the sample. Many common analytical methods do not collect time and spatially resolved data, or cause it to be lost during data processing. For the copper strands studied in the present work, analysis of one small fragment of a strand is not an adequate sample size to evaluate a possible match between different strands or wires.

Experiment II: Effects of Increased Sample Size on Pairwise Comparisons

A larger number of sub-segments were analyzed in order to determine the effects of increased sampling size on pairwise comparisons of copper stands. Four sub-

segments of segment D and E were ablated with the fs laser (Fig. 1b). Eight sub-segments per strand were sampled in this experiment compared to the three sub-segments analyzed in the previous experiment. Mass spectra from four sub-segments of segment D of a strand were compared to those from the four sub-segments of segment D from the remaining strands. With a larger area of copper strand for comparison, the total number of indistinguishable pairwise comparisons increases to 43 (Table 4). The results are similar when the four sub-segments of segment E of a strand are compared to the sub-segments of segment E of the remaining strands in an average Q-residual plot (plot not shown).

The increase in the number of indistinguishable pairwise comparisons compared to Experiment I may be partly due to the number of sub-segments per segment used for analysis. An increase in the number of sub-segments of copper strand leads to a larger number of indistinguishable stands. The increase in spatial variability is attributed to the heterogeneity of the trace elemental composition within the strand. Using four sub-segments as the PCA model in the average Q-residual plot increases the variability within the model. With larger variability within the model, segment D of the remaining strands becomes less distinguishable from the model.

Mass spectra of the eight sub-segments from segments D and E are included in the Q-residual model and compared to spectra from the sub-segments from segment D and E of the remaining strands (Table 5). There are 44 indistinguishable pairwise comparisons when eight sub-segments of a strand are compared to eight sub-segments of the remaining strands in an average Q-residual plot. Again, an increase in the spatial variability of the trace elemental composition over longer distances of copper strand analyzed causes more strands to become indistinguishable from one another based on the average Q-residual

plot. Normally, the precision and reproducibility would be expected to improve when more samples are compared resulting in more distinguishable samples. With these results, an *increase* in the number of indistinguishable samples when more samples are compared is an indication of sampling issues.

Experiment II: Pairwise Comparison of Segments D, and E within an Individual Strand

The four sub-segments from segment D are compared to the four sub-segments of segment E within the same strand in an average Q-residual plot (Fig. 5). The segments of Strand 1 are distinguishable from one another. In the remaining strands, the segments are distinguishable from one another (the average Q-value falls above the 95% C.I.) when one segment is used as the model. However, when the opposite segment of the same strand is used as the model, the segments appear indistinguishable from one another (the average Q-value falls below the 95% C.I.).

In this case, the segment selected as the model affects the comparison diagnosis. This result is caused by the spatial variability of the trace elemental composition within the segment used as the model. When the spatial variability of the sub-segments in the PCA model is larger than that of the sub-segments the model is compared to, the two segments are indistinguishable from one another in the average Q-residual plot.

Note the larger Q-value for the 95% C.I. in the model when the two segments are indistinguishable; the horizontal dashed lines are higher in Fig. 5 in these cases. This is another indication that the model has a larger variation with more spatial variability within the sub-segments. Likewise, the two segments appear distinguishable from one another when the spatial variability in the trace elemental composition of the sub-segments in the model is smaller than that of the sub-segments the model was compared

to. These results also indicate that the spatial variability of the trace elemental composition within a single copper strand is similar to the variability between strands.

All of the trace elements measured contribute to the spatial variability within a model to different degrees, depending on the sub-segment. For example, one sub-segment may have large Pb and Sn signal spikes (e.g., Fig. 4), which increases the variability when that data set is used as the model. Different sub-segments could have large signal spikes in different locations, or from other elements, which would increase the variability when those sets are used as the model. The present work shows that these sub-segments may even originate from the same copper strand, which explains why segments from the same strand are distinguishable as well as indistinguishable from one another, depending on which segment is selected for the model. For example, when segment D, in Strand 2 (Fig. 5) is used as the model segment E from the same stand appears distinguishable from the model. Segment E from Strand 2 has large Sn and Sb signal spikes. This increases the variability within the model for segment E compared to segment D, resulting in segment E being distinguishable from segment D. Conversely, when segment E from Strand 2 is used as the PCA model, segment D is indistinguishable from the model in the Q-residual plot. This again is due to the large variability within the results for segment E when it is used as the model. Large variability within the data set used as the model can cause more data sets to become indistinguishable from the model. Therefore, heterogeneity of the sample and sampling size must be considered in order to confirm an indistinguishable pair or distinguish two samples from one another based on trace elemental composition.

An important observation from this study is that when more sub-segments are included in the PCA model of a Q-residual plot, more strands become indistinguishable

from the model in a pairwise comparison. The increase in the number of indistinguishable pairwise comparisons is due to an increase in the variation within the PCA model. Variation in the data, in this particular case, is a result of fluctuations in the signals for the various m/z values measured during laser ablation of the copper strands. Examples of large variations in PCA models include the Q-residual plot for segment comparison of Strands 2-6 in Fig 5. Multiple effects may cause fluctuations in the signals of the various m/z values. Spatial heterogeneity throughout the copper strand will cause fluctuations in the signal at various m/z values. The more area (or sub-segments) included into the PCA model, the more signal fluctuation is introduced, unless very large areas of the sample are analyzed. This creates a PCA model with large variations, which leads to more indistinguishable strands in a pairwise comparison to the PCA model. Other sources of signal fluctuation were considered and measures were taken to attenuate or correct for these fluctuations, as explained in the Experimental section.

Dissolution Experiments

Dissolution experiments were conducted to ensure that the variability within and between strands was not due to the laser ablation process. Five strands were measured as solutions. After the three segments from five strands were analyzed the copper deposition in the Apex and cones became too large and further analyses would not have been reliable. Fifteen mass spectra were collected per segment of copper strand. Signals for the m/z values were blank subtracted and corrected for the amount of copper strand dissolved and for the internal standard signal.

The fifteen mass spectra per segment for all three segments of the five strands were included into a PCA scores plot (Fig. 6). The fifteen replicates of each segment cluster together in the PCA score space. Replicates or samples which cluster in similar

score space in a PCA scores plot are considered similar, or indistinguishable. However, most of the segments within the same strand, as well as segments between different strands, cluster separately in score space (Fig. 6). The separate clustering of the segments between strands, as well as within a single strand, indicates the segments of a particular strand are dissimilar, or distinguishable from one another. This observation further demonstrates that the trace elemental composition varies significantly both between strands and also between segments of a single strand. Dettman *et al.* also found substantial variability in the trace element composition along ~20 m lengths of copper wire, along with even larger variability in the trace element composition of copper rods produced over a 10 day span (21).

Sample contamination must be considered in the dissolution samples and may account for some separation of the samples in the score space. However, the likeliness of variable contamination in every dissolution sample is considered small; therefore, most of the separation in score space is likely due to spatial variability in the elemental composition throughout a strand.

Conclusions

This study shows that the spatial variability, or homogeneity, of the trace elemental composition within a sample, such as a copper strand, should be determined in order to verifiably distinguish recovered fragments from other strands within the same wire. Examining spatially resolved data is important to verify the variations in elemental composition within a sample. This is an example of a case where ablating only small portions does not adequately represent the entire sample. When a small number of sub-segments from a copper strand are analyzed, the results indicate most of the strands are

distinguishable from one another in pairwise comparisons. However, when sub-segments throughout 30 m of the copper strand are analyzed, many of the strands are no longer distinguishable due to the spatial variability of the trace elemental composition throughout individual copper strands. Individual segments within a single strand are also distinguishable from one another in an average Q-residual plot, indicating spatial variability throughout a strand. When the spatial variability in the trace elemental composition used as the PCA model in an average Q-residual plot increases, more strands become indistinguishable by pairwise comparisons from the PCA model. The variations in the elemental composition along the length of a strand are similar to the variations between different strands. The heterogeneity of the sample and sampling size must be considered in order to confirm an indistinguishable pair, or distinguish two samples from one another, based on trace elemental composition.

In actual forensic applications, the possibility of spatial heterogeneity should be evaluated, particularly in cases where only small samples are available (e.g., copper strand fragments after an explosion). It may be helpful to investigate the manufacturing process more closely to determine the cause of the heterogeneity throughout a copper strand, as described by Dettman *et al.* and done for other materials like container glass (23) and bullet lead (13).

Acknowledgments

Research at the Ames Laboratory was supported by the National Institute of Justice (Award No. 2009-DN-R-112). The Ames Laboratory is operated for the U.S. Department of Energy by Iowa State University under Contract No. DEAC02-07CH11358.

References

1. Watling JR, Lynch B, Herring D. Use of laser ablation inductively coupled plasma mass spectrometry for fingerprinting scene of crime evidence. J Anal Atom Spectrom 1997;12:195-203.
2. Watling JR. Sourcing the provenance of cannabis crops using inter-element association patterns 'fingerprinting' and laser ablation inductively coupled plasma mass spectrometry. J Anal At Spectrom 1998;13:917-926.
3. Bajic S, Aeschliman D, Saetveit N, Baldwin D, Houk RS. Analysis of glass fragments by laser ablation-inductively coupled plasma-mass spectrometry and principal component analysis. J Forensic Sci 2005;50:1123-1127.
4. Suzuki Y, Kikkawa HS, Kasamatsu M, Higashikawa Y, Suzuki S. Forensic discrimination of sheet glass exposed to high temperature by the determination of trace impurities using ICP-MS. Anal Sci 2008;24:745-749.
5. Naes B, Umpierrez S, Ryland S, Barnett C, Almirall J. A comparison of laser ablation inductively coupled plasma mass spectrometry, micro x-ray fluorescence spectroscopy, and laser induced breakdown spectroscopy for the discrimination of automotive glass. Spectrochimica Acta Part B: Atom Spec 2008;63:1145-1150.
6 Watling JR, Herbert H, Delev D, Abell ID. Gold fingerprinting by laser ablation inductively coupled plasma mass spectrometry. Spectrochimica Acta Part B: Atom Spec 1994;49B:205-219.
7. Guillong M, Gunther D. Quasi "non-destructive" laser ablation-inductively coupled plasma-mass spectrometry fingerprinting of sapphires. Spectrochimica Acta Part B: Atom Spec 2001;56B:1219-1231.
8. Watling JR, Herbert HK, Barrow IS, Thomas AG. Analysis of diamonds and indicator minerals for diamond exploration by laser ablation-inductively coupled plasma mass spectrometry. Analyst 1995;120:1357-1364.
9. Arroyo L, Trejos T, Hosick T, Machemer S, Almirall J, Gardinali P. Analysis of soils and sediments by laser ablation inductively coupled plasma mass spectrometry (LA-ICP-MS): an innovative tool for enviromental forensics. Environ Forensics 2010;11:315-327.
10. Deconinck I, Latkoczy C, Günther D, Govaert F, Vanhaecke F. Capabilities of laser ablation-inductively coupled plasma mass spectrometry for (trace) element analysis of car paints for forensic purposes. J Anal At Spectrom 2006;21:279-287.
11. Bartle E, Watling JR. Provenance determination of oriental porcelain using laser ablation-inductively coupled plasma-mass spectrometry. J of Forensic Sci 2007;52:341-348.
12. Green R, Watling JR. Trace element fingerprinting of australian ocher using laser ablation inductively coupled plasma-mass spectrometry (LA-ICP-MS) for the provenance establishment and authentication of indigenous art. J of Forensic Sci 2007;52:851-859.
13. National Research Council (U.S.) CoSAoBLECC. Forensic analysis: weighing bullet lead evidence. Washington, D.C: National Academies Press, 2004.

14. Liu C, Mao XL, Mao SS, Zeng X, Greif R, Russo RE. Nanosecond and femtosecond LA of brass: particulate and ICPMS measurements. Anal Chem 2004;76:379-383.
15. Margetic V, Pakulev A, Stockhaus A, Bolshov M, Niemax K, Hergenröder R. A comparison of nanosecond and femtosecond laser-induced plasma spectroscopy of brass samples. Spectrochim Acta Part B: Atom Spec 2000;55:1771-1785.
16. Možná V, Pisonero J, Holá M, Kanický V, Günther D. Quantitative analysis of Fe-based samples using ultraviolet nanosecond and femtosecond laser ablation-ICP-MS. J Anal At Spectrom 2006;21:1194-1201.
17. Kuhn HR, Günther D. Elemental fractionation studies in laser ablation inductively coupled plasma mass spectrometry on laser-induced brass aerosols. Anal Chem 2003;75:747-753.
18. Günther D, Heinrich CA. Enhanced sensitivity in laser ablation-ICP mass spectrometry using helium-argon mixtures as aerosol carrier. J Anal At Spectrom 1999;14:1363-1368.
19. Aeschliman D, Bajic S, Baldwin D, Houk RS. Multivariate pattern matching of trace elements in solids by laser ablation-inductively coupled plasma-mass spectrometry: source attribution and preliminary diagnosis of fractionation. Anal Chem 2004;76:3119-3125.
20. Berry J, Bajic SJ, Houk RS. Determination of the spatial variability of the elemental composition of copper wire using inductively coupled plasma-mass spectrometry. Poster session: American Academy of Forensic Science, Alanta, 2012.
21. Dettman J, Cassabaum A, Saunders CP, Snyder DL, Buscaglia J. Forensic discrimination of copper items using trace element concentrations. Anal Chem 2014;86:8176-8182.
22. Beebe KR, Pell R, Seasholtz MB. Chemometrics; a practical guide, New York: Wiley, 1998.
23. Harrington KJ, Land DP, Pollock EM, Springer FA, Howitt DG. Forensic development of LA-ICP-MS: elemental profiling and evaluation of homogeneity in soda-lime container glass. 2012. http://projects.nfstc.org. [Accessed 4 December 2012].

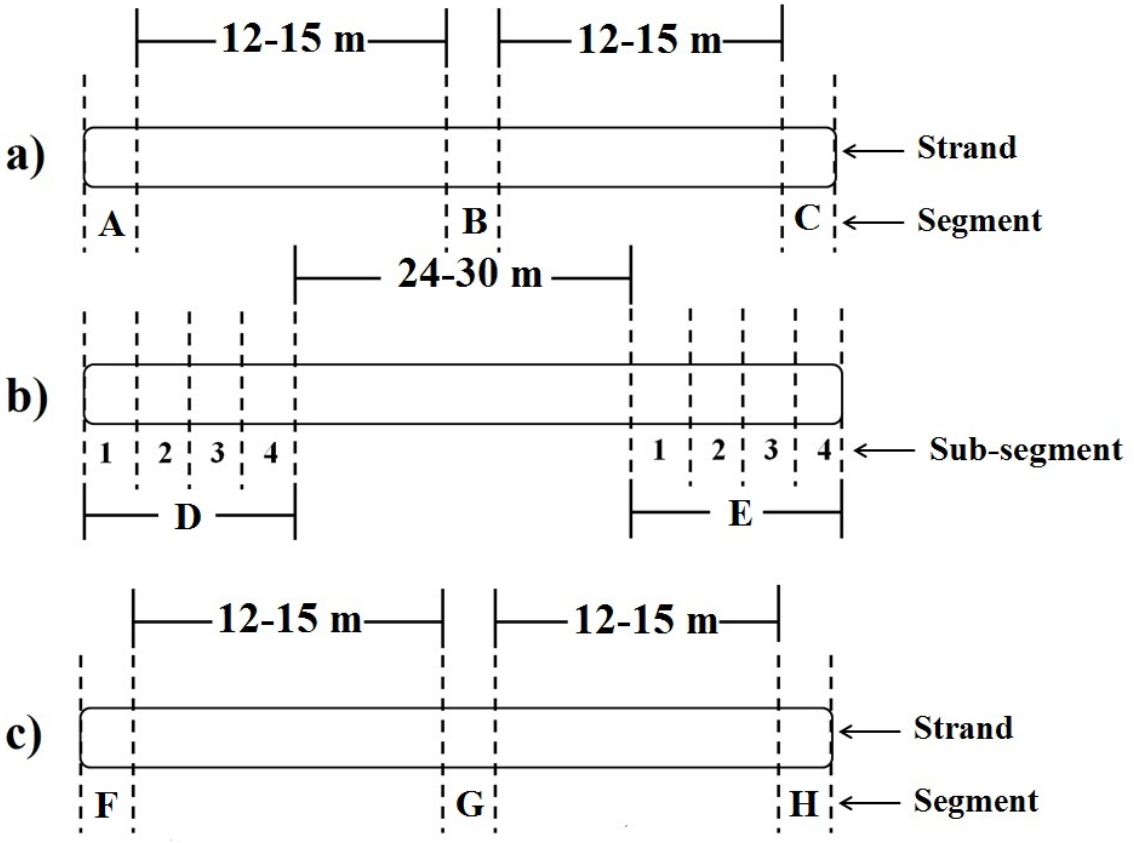

FIG. 1—Illustration of where the segments and sub-segments were removed from copper wire strands for analysis. Figure 1a) depicts the location where the segments and sub-segments were excised from the strand for Experiment I for laser ablation analysis. Figure 1b) depicts the location where the segments and sub-segments were excised from the strand for Experiment II for laser ablation analysis. Figure 1c) is a diagram of the segments removed for sample dissolution analysis.

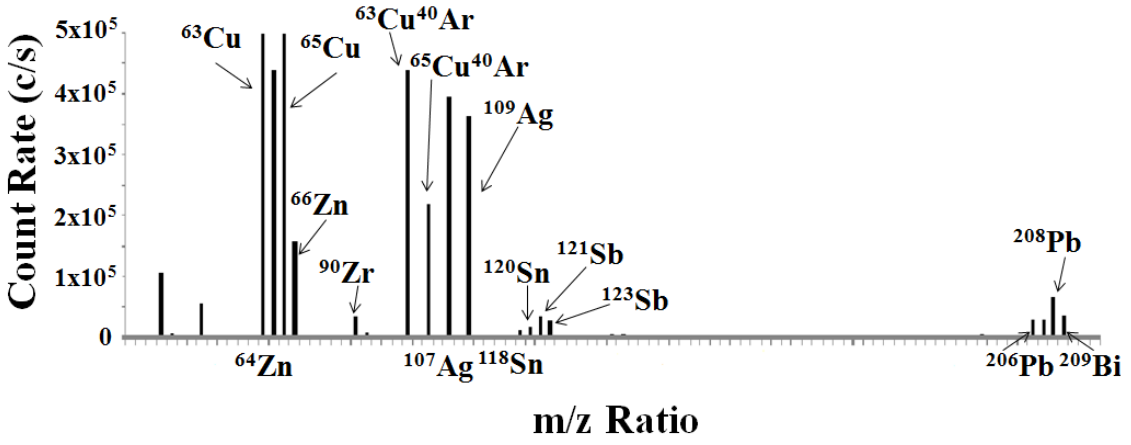

FIG. 2—Average mass spectrum for two copper strands ablated with the fs laser and measured by ICP-MS. Peaks with significant count rates (c/s) were labeled, m/z ratios were measured from ^{7}Li to ^{238}U. Peaks below m/z 63 were not labeled due to polyatomic interferences.

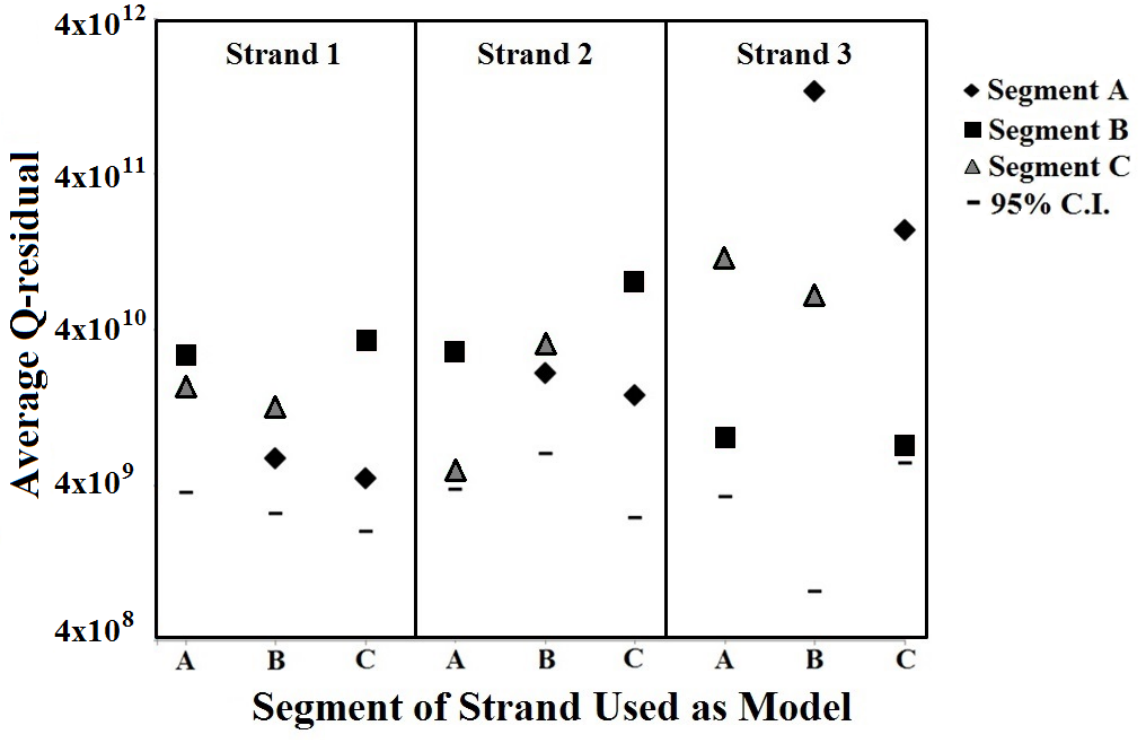

FIG. 3—Average Q-residual plot from segments (A, B, or C) of nine copper strands. The segments in the boxes originate from the strand numbered at the top of each box. The segments from the remaining six strands not shown in plot are also distinguishable from one another within the same strand. Strands were ablated and measured by ICP-MS.

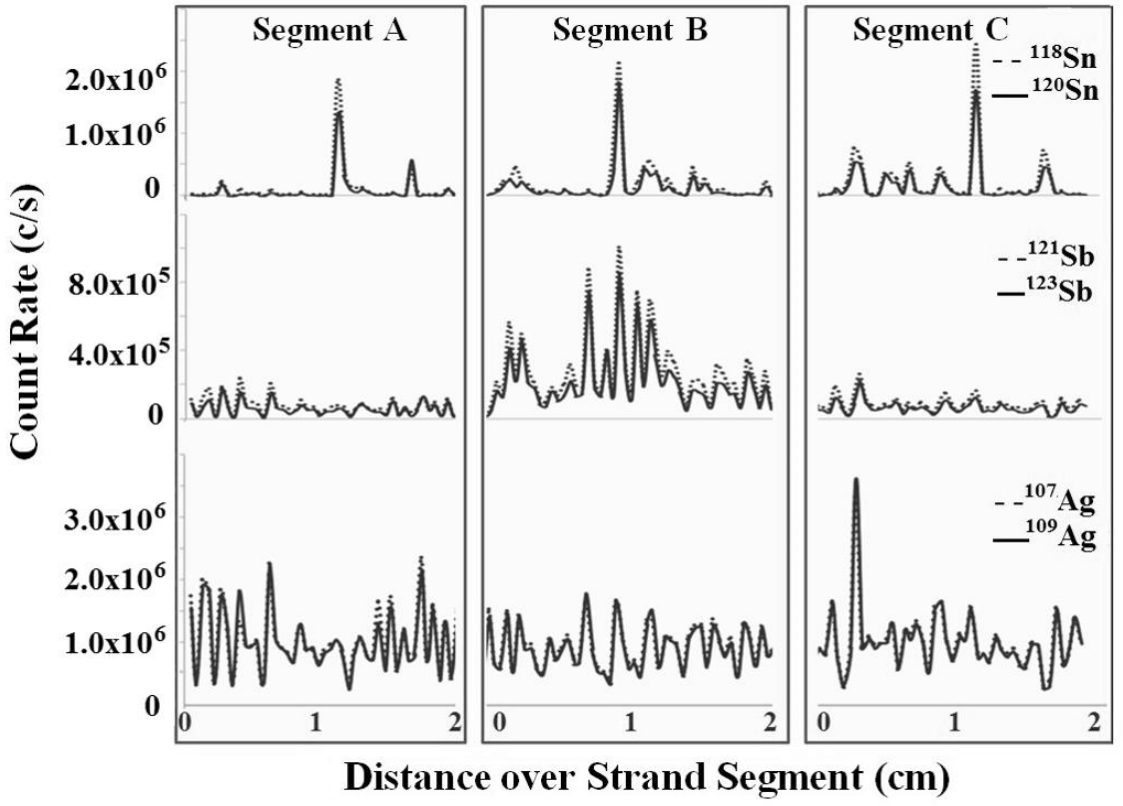

FIG. 4—Plot of count rate (c/s) vs. distance ablated over a strand segment (cm). Segment A, B, and C were removed between 12-15 meters throughout a strand. 45 scans of the selected isotopes were measured on the Element 1 ICP-MS over 275 seconds as the laser ablated over the 2 cm of the strand. Results were similar with the remaining m/z ratios measured. Signals are normalized to $^{63}Cu^{+}$ signal.

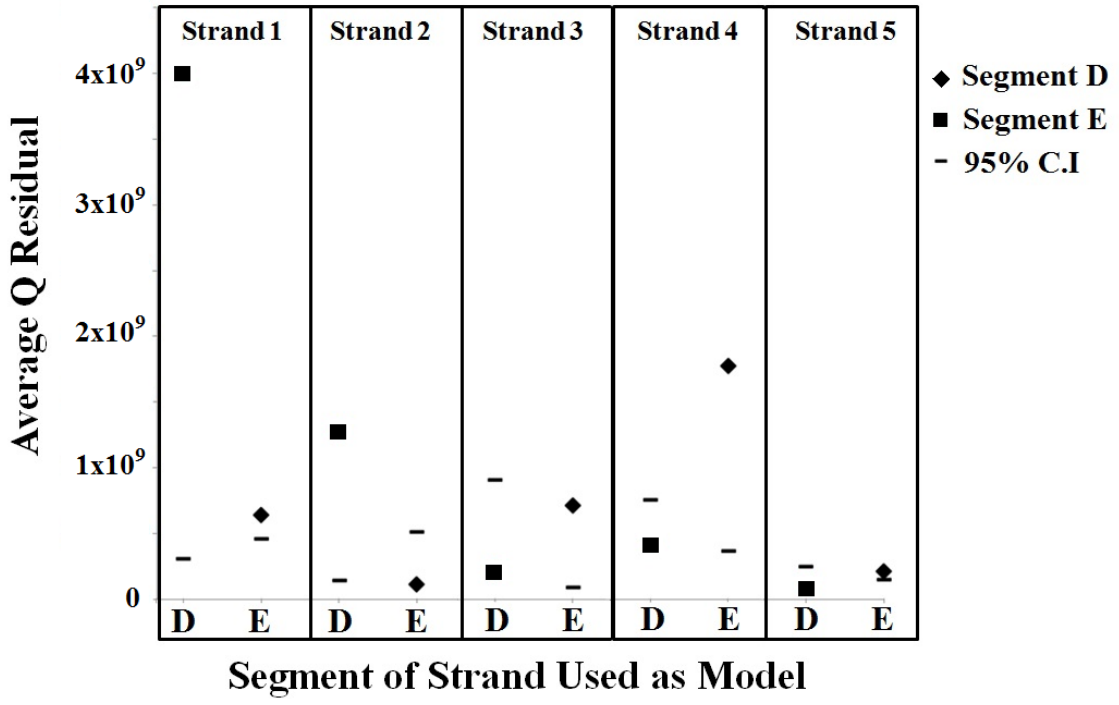

FIG. 5—Average Q-residual plot from one segment (D or E) of five copper strands. The segments in each box originate from the strand numbered at the top of each box. The remaining five strands not shown in plot follow the same trend as the plots above. Wire strands were ablated with the fs laser and measured by ICP-MS.

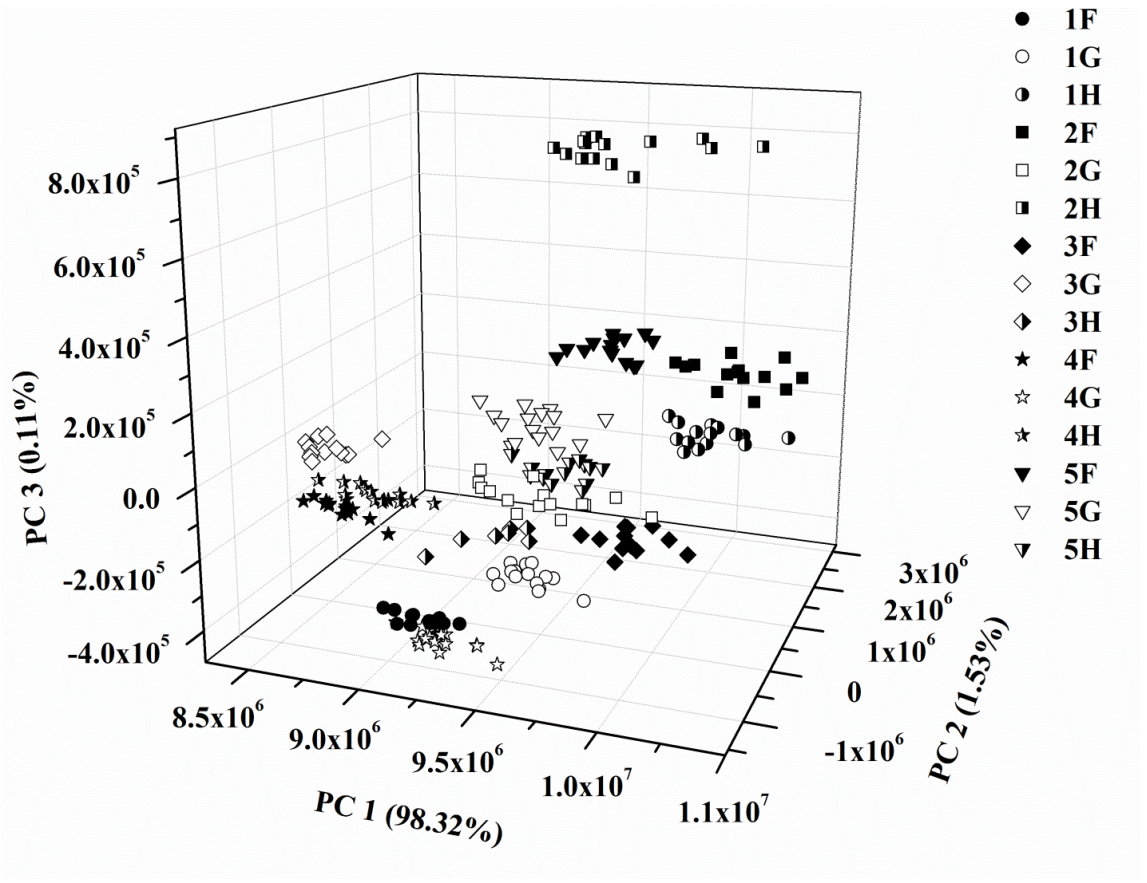

FIG. 6—Scores plot from mass spectra of dissolved samples of three segments, (F, G, and H) from five strands. Each mass spectrum is represented as a single data point on the plot. Segments F, G, and H from Strand 5 cluster close together and may be indistinguishable. The remaining segments cluster separately from one another in score space, indicating that different segments of the same strand are distinguishable.

TABLE 1—Instrument and laser parameters for the analysis of copper wire strands

ICP-MS Instrument	Element I (Thermo Scientific, Inc.)	
Sampler and skimmer cones	Ni, H configuration (Thermo Scientific, Inc.)	
Scan mode	Peak jump	
dwell/settling time	10 ms dwell time/ 2.1 ms settling time	
Resolution	Low	
100 fs Laser	Coherent Libra Ti:Sapphire	
Operational wavelength	266 nm	
Laser energy	140 mW $pulse^{-1}$	
Frequency	1000 Hz	
Spot size	~70 µm	
Raster speed	80 µm sec^{-1}	
	Laser Ablation Experiment	**Dissolution Experiment**
Carrier gas through ablation cell	0.800 + 0.19 L He min^{-1}	-
Additional gas after laser, before torch	0.530-0.550 L Ar min^{-1}	-
Nitrogen gas through Apex Q	-	<10 mL min^{-1}
Sample gas into Apex Q	-	1.015 L Ar min^{-1}
RF Power	1150 W	1150 W
Cool/auxiliary gas stream	16.00/1.16 L Ar min^{-1}	16.00/1.47 L Ar min^{-1}
Torch position, ion optics	Optimized for maximum sensitivity and stability	Optimized for maximum sensitivity and stability
Acquisition		
Runs/passes	Exp. I: 45 runs/1 pass Exp II: 12 runs/ 1 pass	15 runs/1 pass

TABLE 2—Experiment I: Comparison of Segment A. Numbers under "PCA Model" column correspond to the strand from which the mass spectra of segment A was used to produce the PCA model. The mass spectra from segment A of the strands listed in the "Indistinguishable Strand(s)" column are indistinguishable from the strand in the PCA model to a 95% C.I.

PCA Model	**Indistinguishable Strand(s)**
1	-
2	4, 9
3	-
4	-
5	9
7	5
8	-
9	-
10	4, 9

TABLE 3—Experiment I: Comparison of All Segments. Numbers under "PCA Model" column correspond to the strand from which the mass spectra of segment A, B and C were used to produce the PCA model. The mass spectra from segment A, B, and C of the strands listed in the "Indistinguishable Strand(s)" column are indistinguishable from the strand in the PCA model to a 95% C.I.

PCA Model	**Indistinguishable Strand(s)**
1	-
2	8
3	8
4	8
5	8
7	8, 2
8	-
9	1
10	8

TABLE 4–Experiment II: Comparison of Four Sub-Segments from Segment D. Numbers under "PCA Model" column correspond to the strand from which the mass spectra of four sub-segments from segment D were used to produce the PCA model. The mass spectra from four sub-segments from segment D of the strands listed in the "Indistinguishable Strand(s)" column are indistinguishable from the strand in the PCA model to a 95% C.I.

PCA Model	**Indistinguishable Strand(s)**
1	9, 5, 8, 2
2	-
3	1, 2, 5, 8, 9, 10
4	1, 2, 3, 5, 8, 9, 10
5	2, 8, 9, 10
6	1, 2, 3, 4, 5, 7, 8, 9, 10
7	1, 2, 5, 8, 9, 10
8	2, 9, 10
9	5, 10
10	2, 9

TABLE 5—Experiment II: Comparison of All Sub-Segments. Numbers under "PCA Model" column correspond to the strand from which the mass spectra of all sub-segments were used to produce the PCA model. The mass spectra from all sub-segments of the strands listed in the "Indistinguishable Strand(s)" column are indistinguishable from the strand in the PCA model to a 95% C.I.

PCA Model	**Indistinguishable Strand(s)**
1	2, 3, 4, 5, 8, 9, 10
2	3, 5
3	5, 8, 9, 10
4	3, 5, 8, 9, 10
5	8
6	3, 4, 5, 8, 9, 10
7	3, 4, 5, 6, 8, 9, 10
8	5, 9, 10
9	3, 4, 5, 8, 10
10	3, 5, 8, 9

CHAPTER 4. TRACE METAL ANALYSIS OF FLY LARVAE AND PORCINE SKIN TISSUE FOR GUNSHOT RESIDUE ON DECOMPOSING PIG CARRION

Jonna Berry and R. S. Houk

A manuscript submitted for publication in *The Journal of Forensic Science*

Abstract

Identifying trauma wounds on decomposing remains is important in order to establish a cause of death in forensic investigations. This pilot study was performed to assess the potential forensic value for the detection of gunshot residue via the elements Sb, Pb, Ba, and Cu on decomposing remains with laser ablation-inductively coupled plasma-mass spectrometry (LA-ICP-MS). The effects of a variety of unpredictable variables, such as weather, temperature, and human activity, on the retention of gunshot residue around projectile wounds were assessed. A winter and summer study were performed. Elements consistent with GSR persisted in the skin around the gunshot wounds through the winter study for 220 days after death. Antimony was present in the skin around the gunshot wounds in the summer study for 34 days after death. Larvae first appeared on the carcasses in the winter study 157 days after death; these larvae contained the characteristic GSR elements. Larvae were present on the summer study carcasses 24 hours after death. Elements consistent with gunshot residue were detected in the larvae feeding from within the gunshot wounds for 4 to 6 days after death. Other sources of lead and barium contamination, which could be mistaken for GSR, must be considered in actual forensic application of this methodology.

Introduction

Determining the type of trauma present on a recovered body, i.e. sharp force, blunt force, or projectile trauma, is important in forensic investigations to establish the cause of death. Projectile trauma can be difficult to distinguish from sharp force trauma on a decomposing carcass due to the stage of decomposition and insect activity around and within the wound tracts, (1, 2) especially if the bullet is not recovered at the scene. Only a few radiochemical and microscopic studies have been conducted regarding the analysis of gunshot wounds in decomposing remains (1, 3, 4, 5).

The current method to distinguish projectile trauma from other trauma is the detection of gunshot residue (GSR) around the wound. GSR may originate from the primer, propellant, lubricant, bullet, bullet jacket, cartridge case, and barrel of the gun (6). The airborne vaporized particles are ejected through the gun muzzle, cool rapidly into liquid droplets, and subsequently solidify (7). Some of these particles are carried with the bullet and settle in and around the bullet wound. Berryman *et al.* (8) hypothesized that a low pressure gas zone exists behind the bullet which draws in vapor and GSR during passage through tissue. This effect distributes GSR particles throughout the wound tract.

One composition consistent with GSR particles is a combination of lead, barium, and antimony in an individual particle (7). Copper and iron have also been detected in GSR particles (8). GSR particles are typically collected from a surface with an adhesive stub and analyzed using scanning electron microscopy-energy dispersive x-ray spectroscopy (SEM-EDS) (9). SEM-EDS can non-destructively locate and provide morphological information on individual particles which is advantageous for forensic analysis of GSR.

In most forensic casework, GSR is not analyzed on decomposing bodies due to the limitations of current GSR collection methods. Decomposition is a progressive process and can be divided into five chronological stages: fresh; bloat; active decay; advanced decay; and dry or remains (5). During these stages the body undergoes many changes that may alter or obscure gunshot wound evidence on skin (5). Depending on the type of environment in which the body is exposed, the insect activity on the remains, and the stage of decomposition, GSR is only detectable by SEM-EDS around the entrance wound for a short period of time (~24 hours) (1). Efficient GSR collection may be hindered by liquids and adipocere that may be present on the surface of decomposing remains (1). Debris on the sample surface may obstruct particle visualization and detection via SEM-EDS as well (1). SEM-EDS requires long analysis times, which are undesirable for forensic casework. The analysis of a blank stub for GSR background subtraction can take from 2 to 6 hours and analysis time increases with the number of particles on a sample (7). Another limitation of SEM-EDX is that elements of low atomic masses that may be present in GSR can remain undetected by SEM-EDX (10).

Due to the limitations of SEM-EDS for GSR analysis, alternative methods for detecting GSR have been employed. Koons *et al.* demonstrated the potential for ICP-MS to detect GSR through the analysis of cotton swabs spiked with Sb, Ba and Pb from standard solutions (11). Wang *et al.* also used solution nebulization ICP-MS to detect GSR extracted from GSR collection swabs (12). These studies show the potential for ICP-MS to detect GSR, however, samples were not collected from decomposing remains.

GSR particles on decomposing remains are difficult to detect with SEM-EDX, therefore, organisms that feed around wounds on decomposing tissue have been studied. ICP-MS with solution nebulization has been used to analyze blowfly larvae (*Chrysomya*

megacephala) from decomposing porcine carcasses for the presence of GSR. These studies were designed to distinguish projectile trauma from sharp force trauma on carrion. Blowfly larvae that fed on meat contaminated with GSR were digested and analyzed as solutions via ICP-MS for the presence of GSR (1, 2, 3). The larvae studies conducted by LaGoo *et al*. (1), Rashid (2), and Roeterdink *et al*. (3) concluded that the larvae that ate the meat previously shot with a gun contained higher concentrations of elements consistent with GSR than the larvae that fed off of the meat with no GSR.

ICP-MS was also used to analyze GSR on skin tissue around gunshot wounds on a pig carcass to distinguish projectile from sharp force trauma in later stages of decomposition (1). LaGoo *et al.* (1) placed two pig carcasses outside for 37 days during the summer and two additional pigs outside for 60 days during the winter. In each study, one carcass was shot 11 times and the second was stabbed 11 times. After 7 days of insect activity the gunshot wounds and stab wounds were morphologically similar and indistinguishable from one another. No GSR was detected around the surface of the entrance wounds via SEM-EDS after 24 hours. Elements consistent with gunshot residue were present at higher concentrations in the skin tissue around the gunshot wounds compared to the tissue around the stab wounds for 37 days after death in the summer and 60 days after death in the winter study (1). Udey *et al.* (9) further studied the GSR in tissue by examining the possibility of differentiating bullet types in fresh and decomposed tissue using ICP-MS. Elements such as Cu, Fe, Sb, Ba, and Pb were found to be present in significantly different concentrations around the gunshot wounds and could be used to differentiate gunshot wounds from controls. Copper was found in higher concentrations around tissue shot with jacketed bullets. Antimony and lead concentrations were significantly higher in samples shot with non-jacketed bullets (8). These results indicate

gunshot residue may remain embedded in tissues throughout decomposition of the remains.

All of the above studies were conducted using dissolved samples. Laser ablation (LA)-ICP-MS of larvae and tissue samples would provide faster results with less sample preparation for the detection of GSR compared to dissolution for ICP-MS analysis. Most of the skin sample remains intact after LA, in contrast to solution nebulization. If a section of skin is excised and dissolved, that piece is not amenable to further examination by other techniques. We are not aware of other studies on the detection of GSR on blowfly larvae or decomposing tissue using LA-ICP-MS.

This study addresses the retention of GSR embedded in the skin around the gunshot wounds, and also in larvae feeding in and around gunshot wounds, on decomposing carcasses in different environments. Samples were collected over a longer time frame compared to the study by LaGoo *et al.* (1) to determine if GSR can be retained and detected in skin tissue for an extended period of time. The main objective of the present work was to assess the potential value of LA-ICP-MS procedures for the detection of elements consistent with gunshot residue in larvae and skin samples on decomposing remains, and assess the duration that gunshot residue may be retained in such samples.

Experimental

This work included a winter and summer study. All carcasses in this study were obtained from the Iowa State University Swine Farm immediately after being euthanized for other reasons. In both studies pig carcasses were shot or stabbed approximately 1 to 2 hours after death. Carcasses were placed outside in large mesh cages for a period of time to decompose. The mesh cages kept large animals out while allowing insects to

access the remains. To determine the presence of GSR on decomposing remains, two types of samples were collected from all carcasses; a) larvae feeding in and around the gunshot and stab wounds, and b) skin tissue excised from around the wounds.

Winter Study

In the winter study, one pig carcass (~60 kg) was shot 15 times by an Ames Police Department Detective with a Sig Sauer .40 caliber handgun and Winchester SXT 180 grain bonded hollow point jacket ammunition. The barrel of the handgun was cleaned with a Bore Snake between each shot and held approximately 30 cm away from the carcass for each shot. Adjacent gunshot wounds were separated by at least 13 cm. A second pig carcass (~60 kg) was stabbed with a stainless steel kitchen knife 15 times as a control for wound morphology and trace metal content comparisons. Both pig carcasses were placed outside in November 2013 in an open field, approximately one meter apart, in mesh cages to decompose. Mesh cages were constructed from hog panel and covered with 2.54 cm chicken wire fencing. The sides of the cages were buried 15 to 25 cm deep into the soil to prevent animal scavengers from burrowing under the cages to access the carcasses. Mice could still access the carcasses, so 6 mm wire mesh was fastened to both mesh cages in March 2014.

The decomposition process is slower in the winter and skin samples were collected around the fifteen gunshot and stab wounds periodically from November 2013 until the end of June 2014. Flies arrived on the carcasses 144 days after death. Larvae hatched on the carcasses beginning 157 days after death, in April 2014, and were collected for 21 days. No larvae were present on days 174, 176, and 177. No larvae fed from the gunshot wounds from days 165 through 170; only larvae feeding on and inside the stab wounds were collected during this period.

Summer Study

The summer study began in June 2014. Three pig carcasses (~115 kg each) were each shot 15 times with a handgun in the same manner as the Winter Study. Three other pig carcasses (~115 kg each) were each stabbed with a knife 15 times as a control. In order to determine whether different environments affected the duration of time GSR could be detected in the larvae and on the skin, carcasses were placed in separate environments. A set of pig carcasses (one carcass containing gunshot wounds and one carcass containing stab wounds) were placed outside in mesh cages near a river bank. Another set of carcasses were placed in mesh cages in a forested area, and the third set were placed in mesh cages in an open field. The carcasses are referred to as the "river", "trees", and "open field" carcasses, respectively, in this paper. The mesh cages were used as described above.

Larvae were present on the summer carcasses 24 hours after the carcasses were placed outside. To allow time for feeding, the first larvae were collected 24 hours after they appeared. Larvae were collected from all carcasses until they were no longer feeding on or inside the wounds. Skin samples were collected from each carcass until September 2014.

Analysis of Larvae Samples

Larvae feeding in and around the gunshot and stab wounds were collected with plastic tweezers and placed in 15 mL plastic test tubes (Corning Inc.). Numerous larvae were collected feeding in and around three gunshot and three stab wounds from each set of carcasses. Collections occurred daily until larvae were no longer feeding in or around the wounds. Larvae samples were frozen with liquid nitrogen and stored in a freezer at -30 °C until the end of the study.

Frozen larvae were lyophilized (Labconco: FreeZone 4.5) for 24 hours to remove the water. After lyophilization, larvae were stuck to a piece of quartz with collodion and samples were ablated with a femtosecond laser (Coherent Libra) (Table 1). The m/z values for elements consistent with GSR (antimony, barium, and lead) were measured with a quadrupole ICP-MS (Bruker Aurora Elite, now Analytik Jena) to determine the presence of GSR elements.

Analysis of Skin Tissue Samples

Skin tissue was excised from around the wounds with a ceramic knife to avoid metal contamination. The skin was cut approximately 2 cm away from the wound on all sides. The skin sample containing the wound was separated from the underlying fat layer and placed between two pieces of wax paper in a sealable plastic bag. Skin samples were not collected from the same wound twice.

The plastic bags containing the skin samples were stored in a freezer at -30 °C until the end of the study. Skin samples were secured to square pieces of plastic cutting board, 20 x 15 cm, to ensure the sample remained flat while drying. Samples were then placed in a freezer (-80°C) for one hour. All skin samples then were lyophilized (Labconco: FreeZone 4.5) for 72 hours to remove the water. After lyophilization, skin samples were removed from the cutting boards for laser ablation.

Samples were ablated around the edges of the wound entrance hole with a femtosecond laser (Coherent Libra) (Table 1). The m/z values for elements consistent with GSR (copper, antimony, barium, and lead) were measured with a quadrupole ICP-MS (Bruker Aurora Elite, now Analytik Jena) to determine the presence of GSR.

Results and Discussion

Decomposition Observations and Wound Morphology: Winter Study

During the winter study, slight bloating was observed in both carcasses 1 day after death. Outdoor temperatures decreased from 4 °C to -6 °C by day 5 and the carcasses were covered with 2.5 cm of snow. On day 15, the temperature increased to 6 °C and the carcasses bloated further. From day 16 through day 102, the carcasses remained frozen, fully to partially covered in ice and snow, and no further decomposition was observed. Mice were able to access both carcasses through the 2.54 cm chicken wire from day 1 until day 110. Eventually, 6 mm wire mesh was fastened to the exterior of the cages to keep the mice out. As average temperatures increased to 15 °C, further bloating was observed in both carcasses by day 155. Flies were first present on the carcasses on day 144. However, temperatures fell to 4 °C, or lower overnights and no larvae hatched until day 157. Larvae fed from the carcasses for 24 hours and were collected on day 158. Larvae remained on the carcasses until day 186 but were no longer feeding near the wounds after day 178. Decompositional fluid seepage was observed on both carcasses on day 160. The desiccation stage of decomposition began before the last skin sample was collected on day 220.

The wound morphologies of the gunshot wounds and stab wounds were visually distinguishable in the winter study from day 1, until the spring, day 173, (Fig. 1). By day 173 the gunshot wounds and stab wounds were difficult to distinguish visually. Note the stab wound image from day 173 in the winter study (Fig. 1). The stab wound is encircled in the photograph and was the only hole present originally. The additional holes were created by the larvae as entrance and exit holes to travel within the carcass. These holes could potentially be mistaken for trauma wounds on decomposing carcasses.

Decomposition Observations and Wound Morphology: Summer Study

In the summer study, bloating was observed in all carcasses only 2 hours after death. Average outdoor temperatures throughout the summer study ranged from 14 °C to 27 °C. Egg masses were present on all carcasses 9 hours after death. Larvae hatched on all carcasses on days 2 or 3. Larvae collection began on day 3, after feeding from the carcasses for 24 hours, and collection began on day 4 from the open field stab wound carcass. Collection continued until larvae no longer fed on and within the wounds, which occurred on day 17 for the carcasses near the river, day 19 for the carcasses in the trees, and day 25 for the carcasses in the open field. Beetles are predators of fly larvae and arrived on most carcasses by day 8. Less beetle activity was observed on the carcasses in the open field compared to the carcasses near the river and in the trees, which may have allowed the larvae to feed around and within the wounds on these carcasses for a longer period of time. On day 25, 4 cm of rainfall caused the river near the farm to flood. The carcasses placed under the trees and in the open field were submerged under approximately 50 cm of flowing water for an unknown period of time (less than 24 hours). Skin samples were collected until day 34 on all carcasses. After day 34, no further wounds were discernable on the carcasses in the trees or open field, due to insect activity, decomposition, and the flood. The carcasses near the river were not affected by the flood and skin samples around wounds were collected on day 53 and 106 as well. The desiccation stage of decomposition began by day 53 of the summer study.

The wound morphology of the gunshot wounds and the stab wounds on the summer study carcasses were no longer visually distinguishable only 6 to 9 days after death (Fig. 2). This period is short due to high larvae activity on the carcasses and an increased rate of decay caused by the warmer temperatures during the summer study.

Detection of Gunshot Residue

In order to determine the elements that may distinguish the gunshot wounds from stab wounds, full elemental mass scans were completed during LA-ICP-MS of sixteen skin samples, eight containing gunshot wounds and eight containing stab wounds (Table 1). The elements Sb, Pb, Ba, and Cu were found to be present at higher levels around the gunshot wounds compared to the stab wounds and therefore, all skin samples were analyzed by LA-ICP-MS for these four elements.

Sb, Pb, and Ba are elements consistent with gunshot residue. Gunshot residue may also contain copper, although transfer from the copper jacket is the more probable source of copper on the skin samples around the gunshot wounds. Some species of the *Diptera* order regulate copper for growth (14). Therefore, copper was not evaluated in the larvae samples, only Sb, Ba, and Pb were measured.

The amount of GSR deposited around each gunshot wound did vary and may account for some variation in the amount of GSR elements found. In order to minimize the variation of deposited GSR, the guns in both the winter and summer studies were cleaned between shots to minimize carry over from the previous shot. The guns were also held at approximately the same distance from the carcasses for each shot. Sample signals were normalized to signals from a standard NIST 612 reference glass sample in order to eliminate changes in signals due to day-to-day laser and plasma variations, as well as signal loss due to the cone clogging.

Notice the data plots have a three or four cycle log scale on the vertical axis. Thus, a small separation between points for the samples collected from the carcasses containing gunshot wounds and from the samples containing stab wounds on the plots amounts to a large difference in the measured signals.

Winter Study: Skin Samples

Decompositional changes and mice activity made wound identification difficult near the end of the winter study. As a result, 11 skin samples were collected out of the 15 wounds which were inflicted into both carcasses.

Figure 4 shows a significant difference in antimony levels contained in the skin around the gunshot wounds compared to the stab wounds is observed for 155 days after death. Antimony levels were reduced by day 178. However, levels remained higher around the gunshot wounds than the stab wounds throughout the entire study. Lead levels in the skin around the gunshot wounds were also significantly higher than the lead levels in the skin around the stab wounds throughout the entire study, 220 days after death (Fig. 5). Barium levels in the skin around the gunshot wounds were initially higher than around the stab wounds. A reduction in barium abundance near the gunshot wounds occurred between day 47 and day 68; in this period nearly 8 cm of snow had accumulated. Regardless, a significant difference in barium levels around the gunshot wounds compared to the stab wounds remained for 155 days after death (Fig. 6). Copper levels were significantly higher in the skin around the gunshot wounds for 47 days after death compared to the stab wounds (Fig. 7). The decrease in copper levels around the gunshot wounds by day 68 may be due to the increase in precipitation between days 47 and 68 (Fig. 8).

Winter Study: Larvae Samples

In the winter study, when larvae were present within the gunshot wounds, both antimony and lead levels were higher in the larvae feeding on the gunshot wounds compared to the larvae feeding on the stab wounds (Figs. 8-9). Larvae were feeding on and within the gunshot wounds from day 158 to 166 and day 170 to 178. Larvae feeding

from the stab wounds were analyzed on days 158 through 178 (Figs. 8-10). Even though larvae were not present until 157 days had elapsed, Sb and Pb still persisted. Barium levels within the larvae feeding from the gunshot and stab wounds vary with time; and no significant difference is observed between Ba in gunshot vs. stab wounds (Fig. 10). This may be due to the possible bioaccumulation of barium within larvae which was also observed by LaGoo *et al.* (1). Barium may be a less reliable indicator element for the determination of gunshot residue within larvae.

Summer Study: Skin Samples

Due to decompositional changes, high larvae activity, and the flood, identification of all wounds on the carcasses in the summer study was difficult. Of the 15 wounds inflicted into all carcasses, 9 skin samples were collected from the carcasses in the trees and the open field, and 11 skin samples were collected from the carcasses near the river.

Antimony levels are very high in the skin around the gunshot wounds compared to the stab wounds for four days after death (Fig. 12). The difference in antimony levels in the skin around the gunshot wounds compared to the skin around the stab wounds decreases over 34 days of decomposition. Note the vertical axis is a log scale (Fig. 12), and despite the flood on day 25, the antimony levels around the gunshot wounds still remain at least two times higher than that around the stab wounds for the remainder of the study. No wounds remained on the carcasses in the open field and in the trees after 34 days. Antimony levels in the gunshot wounds collected from the carcasses near the river remain higher 106 days after death (Fig. 12), even in the summer.

Lead levels in the skin around the gunshot wounds were significantly higher compared to the lead levels around the stab wounds for four days after death (Fig. 13). By day 6 lead levels in the skin around the stab wounds increased and remained at higher

levels throughout the remainder of the study. Lead is found in many sources and is a very common contamination element. Possible lead contamination from dust stirred up from the fields on the farm or from gasoline in the trucks or tractors may be the cause of the increase in lead levels on the carcasses. Lead levels around the gunshot wounds from the carcasses in river and trees were at least three times higher than the lead around the stab wounds for the entire study (Fig. 13). Other sources of lead near carcasses should be considered for similar studies.

Barium levels in the skin around the gunshot wounds were higher than in the stab wounds initially. However, Ba levels did not persist for more than one day after death. Barium levels on the skin of the gunshot wounds were comparable to, or lower than, the barium levels on the skin of the stab wounds for the majority of the study. An increase in barium levels in the gunshot and stab wounds occurred between days 20 and 34. The cause of the increase in barium is unknown, however, the flood occurred during that time frame and may be a possible source of the excess barium. Herbicides that were sprayed onto the fields throughout the study were tested for possible trace metal contamination and no antimony, barium, or lead were measured in any of the herbicides.

Copper levels in the skin around the gunshot wounds were significantly higher than the copper levels in the skin around the stab wound for 12 days after death (Fig. 15). An increase in precipitation after day 8 of the study may account for the loss in copper levels in the skin around the gunshot wounds (Fig. 16). Copper is retained in the skin for a shorter duration around the gunshot wounds than antimony or lead, which may be an indication that the copper is from a different source, possibly transfer from the bullet jacket and not from the GSR.

Several unexpected events, such as the flood and possible contamination most likely caused by human activity in the summer, and mice in the winter, occurred while the carcasses were outside. These types of uncontrolled events would occur in actual forensic practice as well. This study indicates that GSR persists around a wound robustly enough to withstand many weather and human events.

Summer Study: Larvae Samples

Antimony levels within the larvae feeding from the gunshot wounds were significantly higher than the antimony levels within the larvae feeding from the stab wounds for 10 days after death (Fig. 17).

Lead levels in the larvae feeding on the gunshot wounds were higher than in the larvae feeding on the stab wounds for 4 days after death (Fig. 18). Lead levels in the larvae from the carcasses in the open field increased on day 5. An increase in lead levels in the larvae from the carcasses in the trees was observed 9 days after death. Increased lead levels in the larvae occurred at similar times as the increase in the lead levels on the skin around the wounds.

No significant difference in barium levels from the larvae feeding on the gunshot wounds was observed compared to the larvae feeding on the stab wounds throughout the entire study (Fig. 19). Similar results were observed from the larvae in the winter study (Fig. 10). These results in barium levels may be caused by the bioaccumulation of barium within larvae. Barium may not be a reliable element for the determination of gunshot residue within larvae, either. Larvae will not migrate from one food source to another. Therefore, it is unlikely that the increase in lead and barium levels in the larvae feeding from the stab wounds is caused by larvae that migrated from the carcass containing gunshot wounds.

Long lyophilization periods (up to 72 hours) were required for this study due to the large number of samples to be freeze dried. In most criminal cases, fewer larvae and less skin tissue would be collected for GSR analysis, so lyophilization would be much faster. Therefore, this method can still be considered a simple and rapid sample preparation method for the analysis of GSR on decomposing carcasses.

Quantification of Sb, Pb, Ba, and Cu present around the wounds would be difficult with LA-ICP-MS because a matrix matched standard is needed for calibration, i.e., to assure similar ablation of both the standard and the sample. Determining quantifiable amounts of element consistent with GSR would also be difficult with dissolution of samples due to uncertainty in the original amount of GSR dissolved. Dissolution is a destructive analysis method, and the original sample integrity may have significant forensic importance. Comparing the levels of metals consistent with GSR around gunshot wounds to stab wounds on decomposing remains can be considered a valid qualitative assessment for the detection of GSR.

Conclusions

Larvae, temperature, and precipitation had substantial effects on the retention of GSR in the skin around gunshot wounds on decomposing carcasses. In the winter study, outdoor temperatures were lower, larvae activity was absent or delayed, and elements consistent with GSR and possible transfer from the bullet were detected in the skin around the gunshot wounds at higher levels compared to the stab wounds for an extended period of time. Gunshot and stab wounds were no longer visually distinguishable on the winter study carcasses 173 days after death. However, antimony and lead were detected at higher levels in the skin around the gunshot wounds compared to the stab wounds for the entire duration of the study, 220 days after death.

Larvae were present on the winter study carcasses 157 days after death. When larvae were present within the gunshot wounds, antimony and lead were detected in the larvae feeding on the gunshot wounds at higher levels than the larvae feeding on the stab wounds.

In the summer study, elements consistent with GSR and bullet wipe were initially detected in the skin around the gunshot wounds at higher levels than the stab wounds. Due to warmer temperatures, higher larvae activity, increased decomposition rates, and rainfall, the levels of antimony, lead, barium, and copper around the gunshot wounds are reduced more quickly than in the winter study carcasses. Gunshot and stab wounds were no longer visually distinguishable 6 days after death. Antimony and lead levels in the skin around the gunshot wounds remained higher than the stab wounds throughout the entire study.

Larvae were present on the summer study carcasses 24 hours after death. Antimony was detected in larvae feeding on the gunshot wounds at higher levels than larvae feeding on the stab wounds for 10 days after death. Lead levels in the larvae feeding on the gunshot wounds were higher than the larvae feeding on the stab wounds for 4 days after death. Due to possible bio accumulation of barium and regulation of copper for growth in larvae, barium and copper may not be reliable elements for the determination of GSR within larvae.

Possible contamination sources of lead and barium near carcasses must be considered with this type of study. Contamination from human activity on the farm may have contributed to the increase in lead and barium levels in the larvae and skin samples during the study. Little human activity occurred around the carcasses throughout the winter study and no contamination was observed in the larvae or skin samples.

The purpose of this study was to assess the potential for LA-ICP-MS to detect GSR that had been retained around gunshot wounds throughout decomposition. The initial results are promising and future studies to further validate this method in different environments are desirable. Additional studies would be needed in order to assess the retention of GSR around gunshot wounds in other environments and climates. Studies where animal scavengers are allowed access to the carcasses would provide further information as to the identification of gunshot wounds and retention of GSR around the wounds when large animals are present. Determining the period of time GSR is retained around gunshot wounds on human cadavers compared to pig carcasses would be an important study considering pig skin is thicker than human skin and therefore may retain GSR for longer periods of time.

In general, these early results indicate potential forensic value of measuring GSR elements in skin and larvae. More such studies will help to clarify effects of factors such as weather and nearby human activity, which would occur in real forensic applications.

Acknowledgments

Research at the Ames Laboratory was supported by the National Institute of Justice Graduate Research Fellowship (Award No. 201-IJ-CX-0012). The authors would like to extend our greatest appreciation to the Ames Police Department for their cooperation, and for their time and ammunition. We would also like to thank Dr. Basil Nikolau and his research group at Iowa State University (ISU) for the use of their lyophilizer. The ISU Swine Farm provided the carcasses for this study. The mesh cages and some equipment for this study were borrowed from the ISU College Shop. The Ames Laboratory is operated for the U.S. Department of Energy by Iowa State University under Contract No. DEAC02-07CH11358.

References

1. LaGoo L, Schaefer LS, Szymanski DW, Smith RW. Detction of gunshot residue in blowfly larvae and decomposing porcine tissue using inductively coupled plasma mass spectrometry (ICP-MS). J Forensic Sci 2010;55(3):624-632.
2. Rashid RA, Ariffuddin N, Ahmad NW. Blowfly, Chrysomya megacephala as an alternative specimen in determination of gunshot residue. Proceedings of IEEE Symposium on Business, Engineering and Industrial Applications: 2012:542-547.
3. Roeterdink EM, Dadour IR, Watling JR. Extraction of gunshot residues from the larvae of the forensically important blowfly Claaiphora dubia (Macquart) (Diptera: Calliphoridae). Int J Legal Med 2004;118:63-70.
4. Taborelli A, Gibelli D, Rizzi A, Andreola S, Brandone A, Cattaneo C. Gunshot residues on dry bone after decomposition--a pilot study. J Forensic Sci 2012;57(5):1281-1284.
5. MacAulay LE, Barr DG, Strongman DB. Effects of decomposition on gunshot wound characteristics: under moderate temperatures with insect activity. J Forensic Sci 2009;54(2):443-447.
6. Goode SR, Dockery CR, Bachmeyer MF, Nieuwland AA, Morgan SL. Detecting gunshot residue by laser induced breakdown spectroscopy. Optical Society of America 2002:175-177.
7. Dalby O, Butler D, Birkett JW. Analysis of gunshot residue and associated materials--a revie. J Forensic Sci 2010;55(4):924-943.
8. Berryman HE, Kutyla AK, Davis IRJ. Detection of gunshot primer residue on bone in an experimental setting--an unexpected findin. J Forensic Sci 2010;55(2):488-491.
9. Udey RN, Hunter BC, Smith RW. Differentiation of bullet type based on the analysis of gunshot residue using inductively coupled plasma mass spectrometry. J Forensic Sci 2011;56(5):1268-1276.
10. Germani MS. Evaluation of instrumental parameters for automated scanning electron microscopy/ gunshot residue particle analysis. J Canadian Soc of Forensic Sci 1991;36(2):331-342.
11. Taudte RV, Beavis A, Blanes L, Cole N, Doble P, Roux C. Detection of gunshot residues using mass spectrometry. Biomed Res Int 2014:1-16.
12. Koons RD. Analysis of gunshot primer residue collection awabs by inductively coupled plasma-mass spectrometry. J Forensic Sci 1998;43(4):748-754.
13. Wang XD. Determination of antimony, barium, and lead in gunshot residues using the aurora M90 ICP-MS. Bruker; 2011 Application Note No.:CA-273253.
14. Timmermans KR, Peeters W, Tonkes M. Cadmium, zinc, lead and copper in Chrionomus riparius (Meigen) larvae (Diptera, Chironomidae): uptake and effects. Hydrobio 1992;241:119-134.

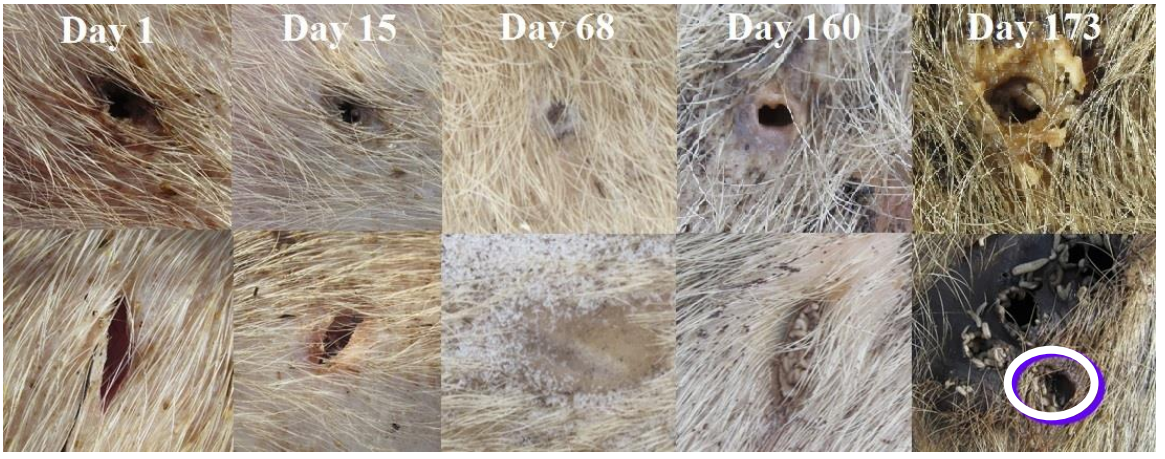

FIG. 1– Comparison of wound morphology in the winter study as carcasses decomposed. The top row is gunshot wounds and the bottom row is stab wounds. Images are not the same wound from day to day. The days listed on the top are the number of days after death. The stab wound is encircled on day 173; the remaining holes were formed as the larvae fed from the carcass.

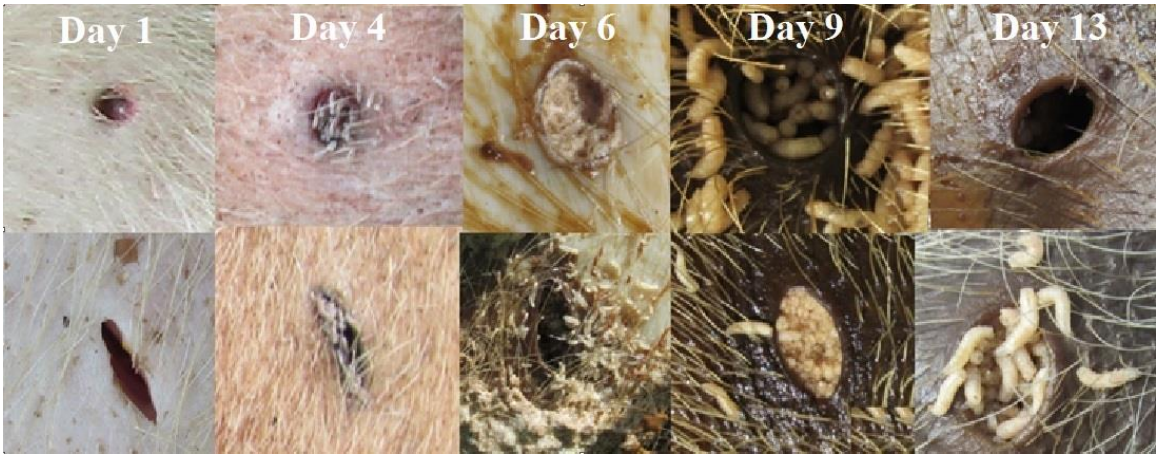

FIG. 2– Comparison of wound morphology in the summer study as carcasses decomposed. The top row is gunshot wounds and the bottom row is stab wounds. Images are not the same wound from day to day. The days listed on the top are the number of days after death.

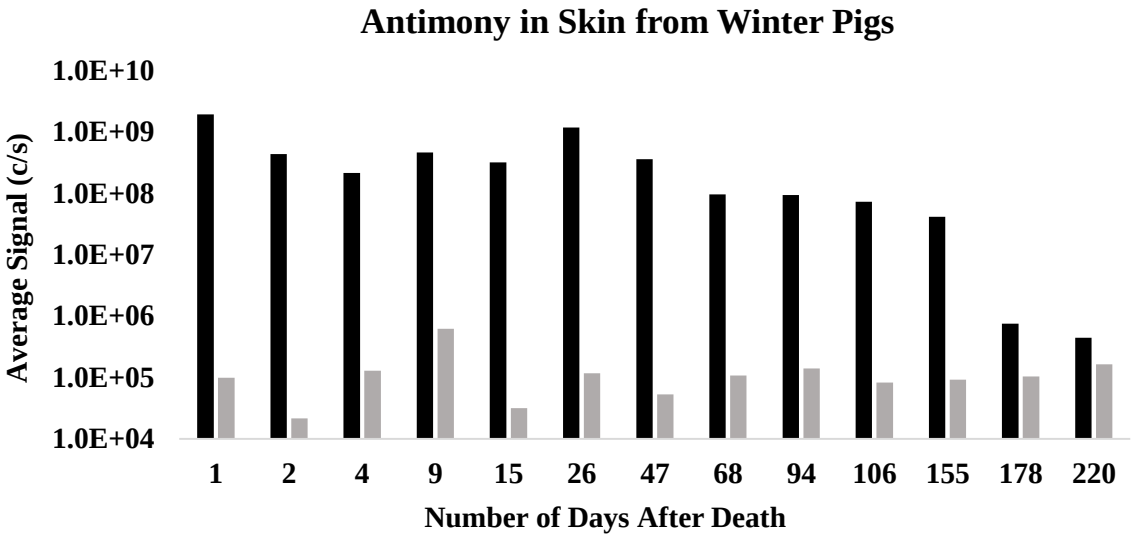

FIG. 3– Log plot of antimony signals in pig skin around gunshot wounds (black) and stab wounds (gray) from the winter study carcasses.

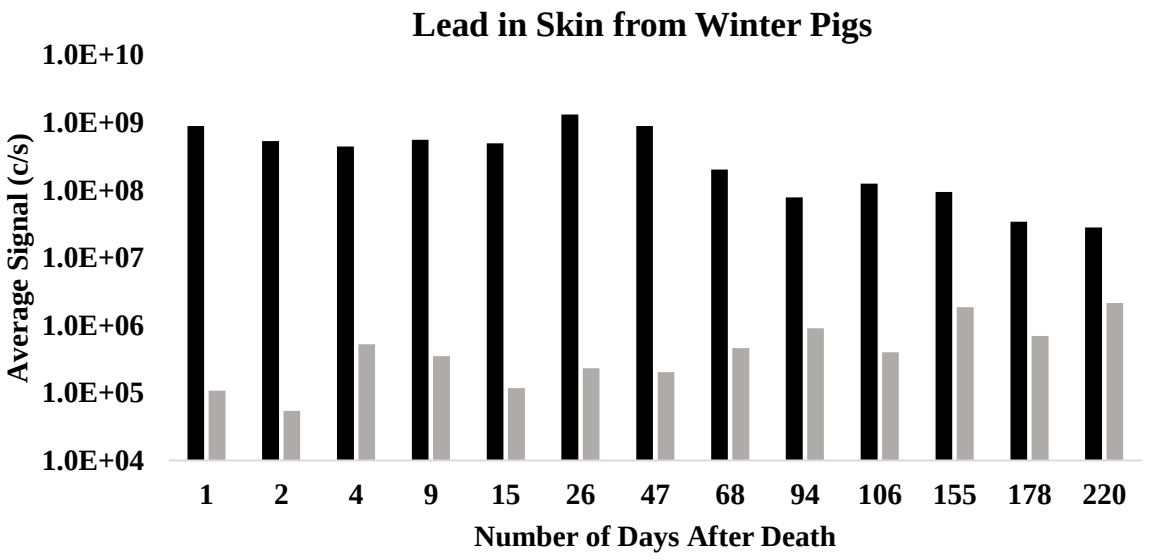

FIG. 4– Log plot of lead signals in pig skin around gunshot wounds (black) and stab wounds (gray) from the winter study carcasses.

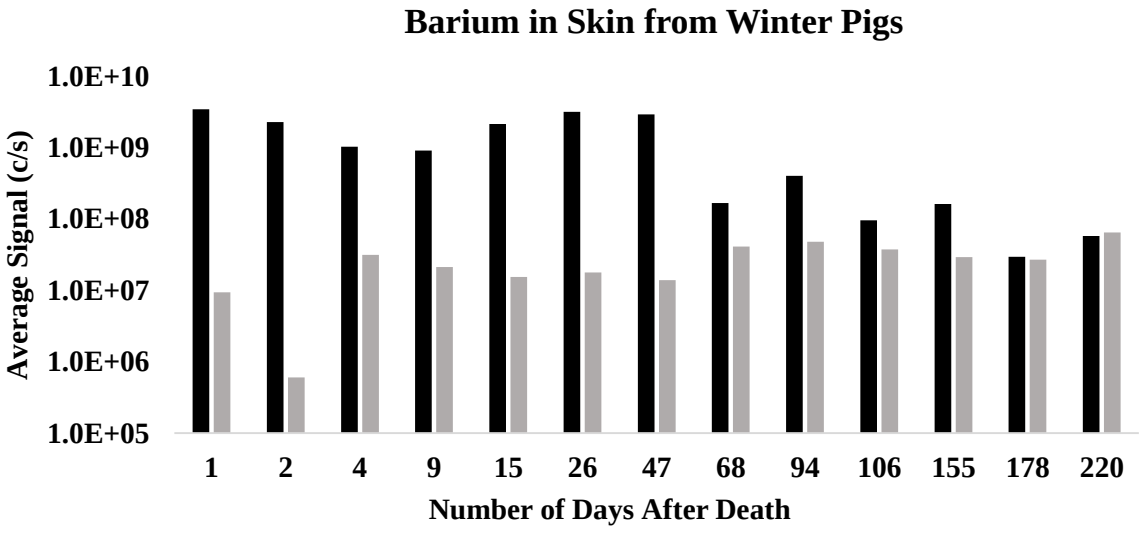

FIG. 5– Log plot of barium signals in pig skin around gunshot wounds (black) and stab wounds (gray) from the winter study carcasses.

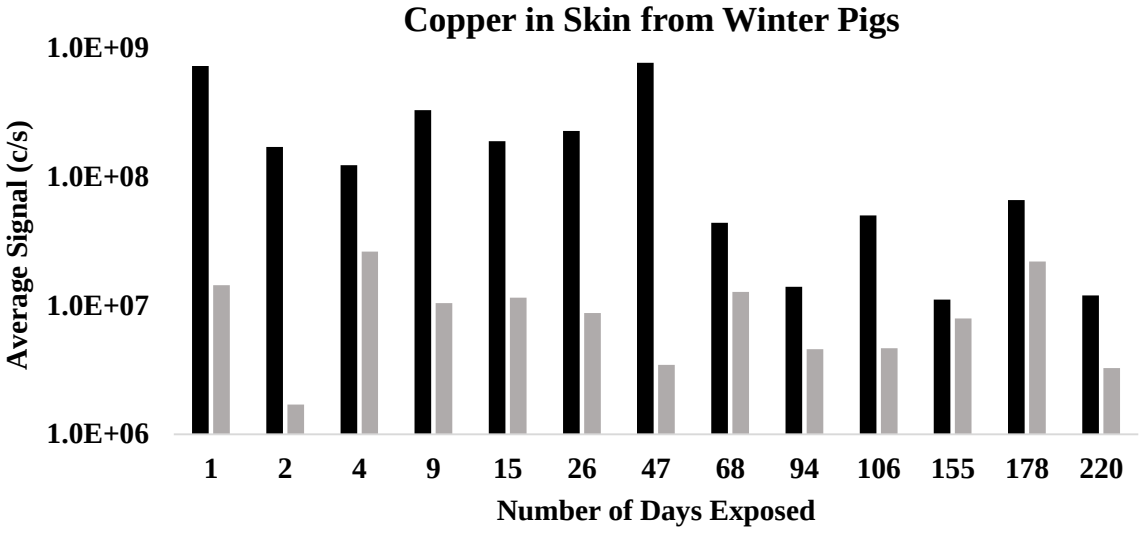

FIG. 6– Log plot of copper signals in pig skin around gunshot wounds (black) and stab wounds (gray) from the winter study carcasses.

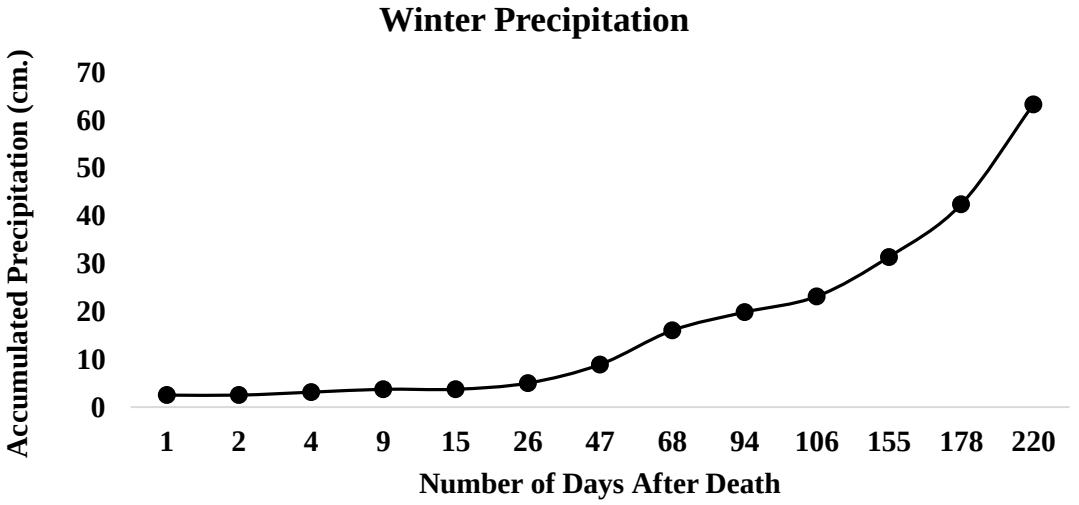

FIG. 7– Plot of accumulated precipitation throughout the winter study. Between days 8 through 128 the precipitation occurred as snowfall. Rainfall occurred between days 1 through 7 and 129 through 220. The x-axis corresponds to the days that skin samples were collected from the carcasses.

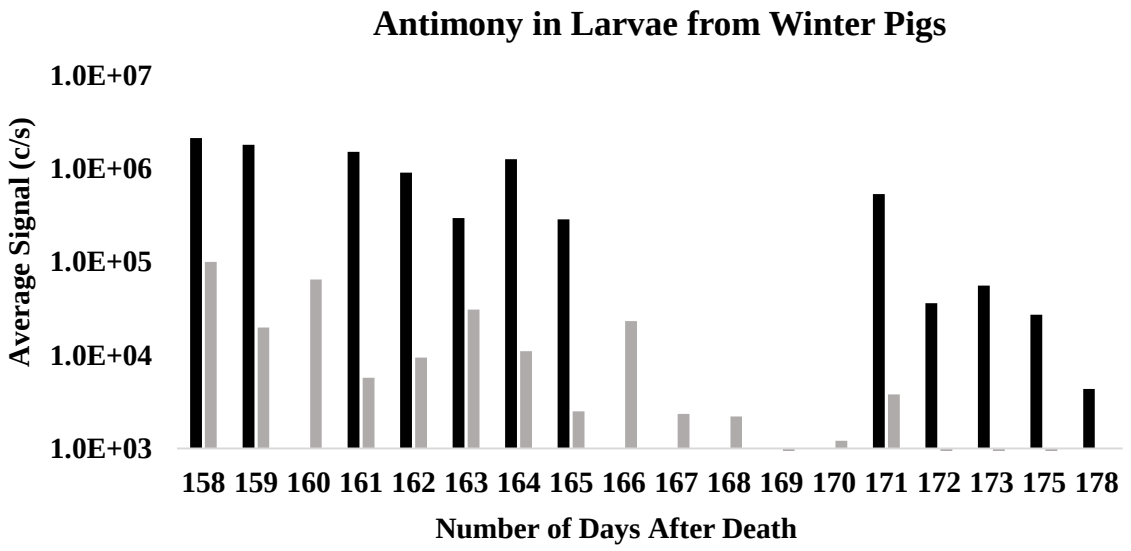

FIG. 8– Log plot of antimony signals in larvae feeding in and around the gunshot wounds (black) and stab wounds (gray) from the winter study carcasses.

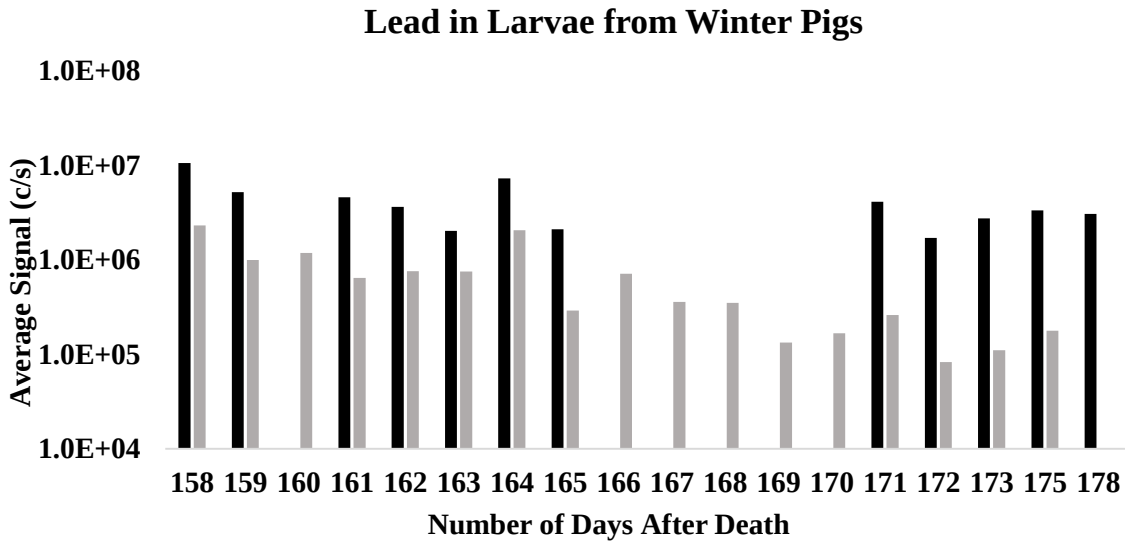

FIG. 9– Log plot of lead signals in larvae feeding in and around the gunshot wounds (black) and stab wounds (gray) from the winter study carcasses.

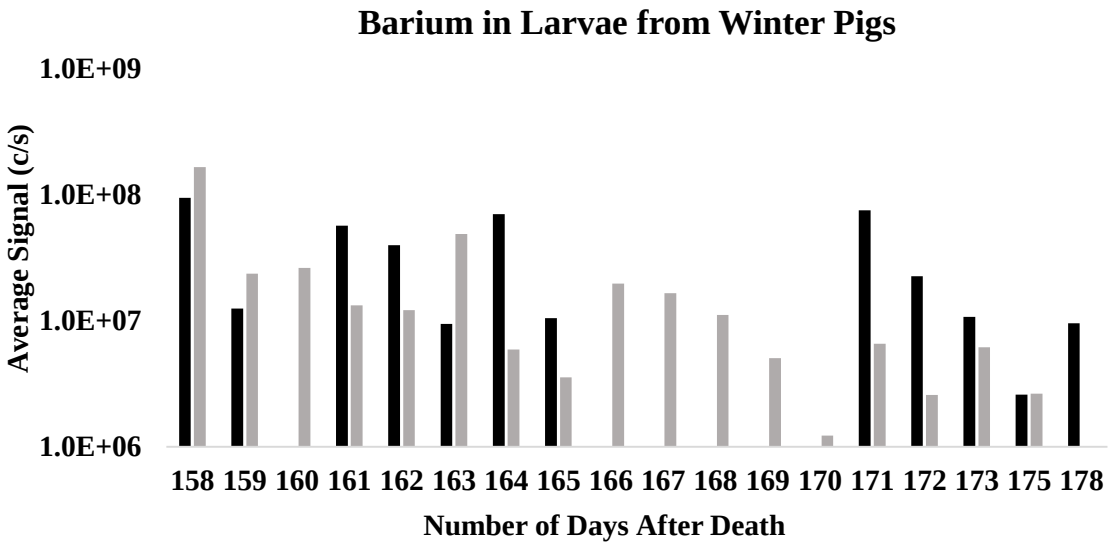

FIG. 10– Log plot of barium signals in larvae feeding in and around the gunshot wounds (black) and stab wounds (gray) from the winter study carcasses.

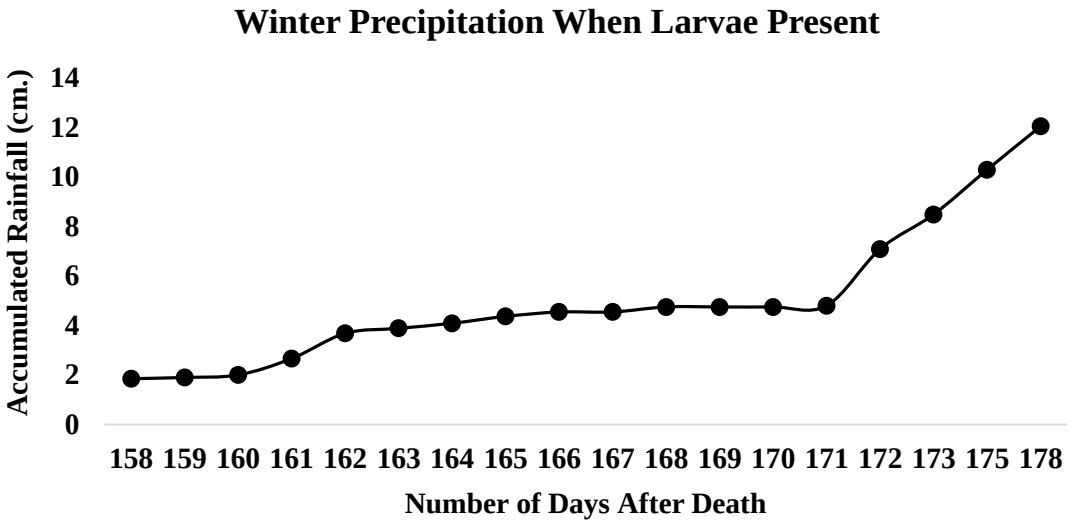

FIG. 11– Plot of accumulated rainfall while larvae were present on the carcasses during the winter study. The x-axis corresponds to the days that larvae were collected from the carcasses.

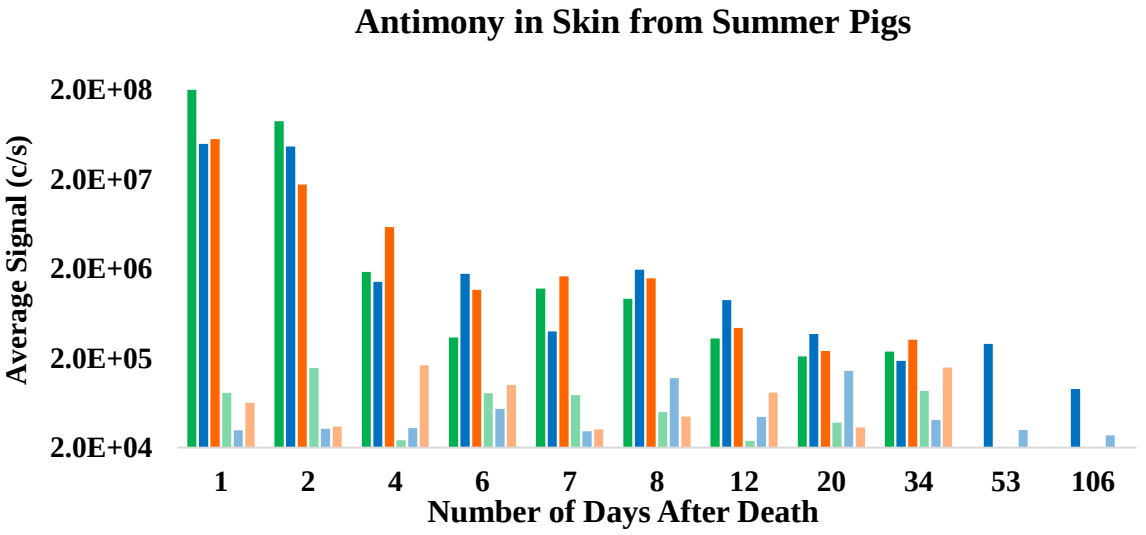

FIG. 12– Log plot of antimony signals in pig skin around gunshot wounds (darker colors) and stab wounds (lighter colors) from the summer study, open field (green), river (blue), and tree (orange) carcasses.

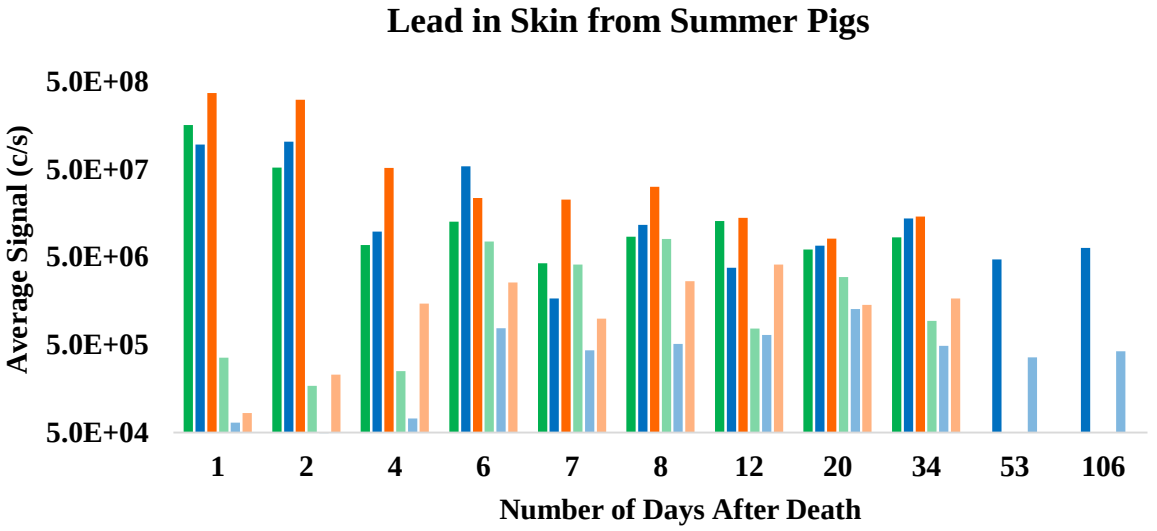

FIG. 13– Log plot of lead signals in pig skin around gunshot wounds (darker colors) and stab wounds (lighter colors) from the summer study, open field (green), river (blue), and tree (orange) carcasses.

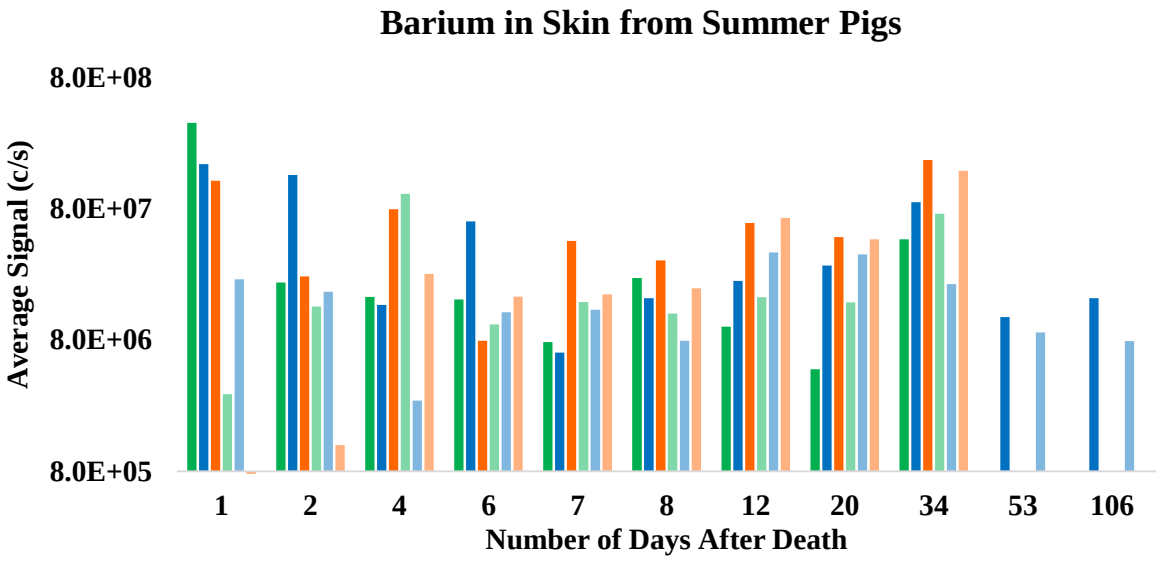

FIG. 14– Log plot of barium signals in pig skin around gunshot wounds (darker colors) and stab wounds (lighter colors) from the summer study, open field (green), river (blue), and tree (orange) carcasses.

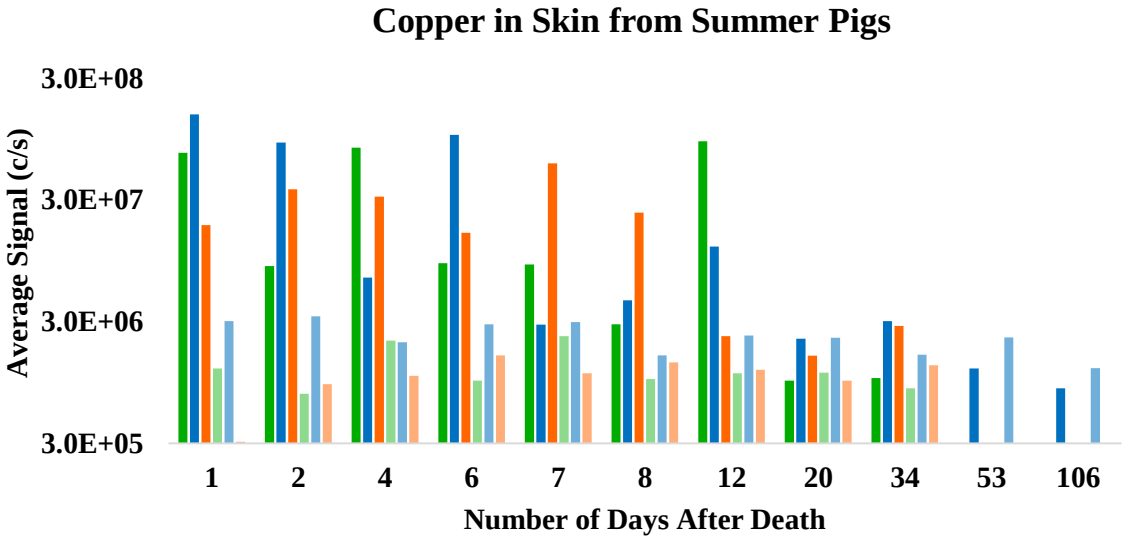

FIG. 15– Log plot of copper signals in pig skin around gunshot wounds (darker colors) and stab wounds (lighter colors) from the summer study, open field (green), river (blue), and tree (orange) carcasses.

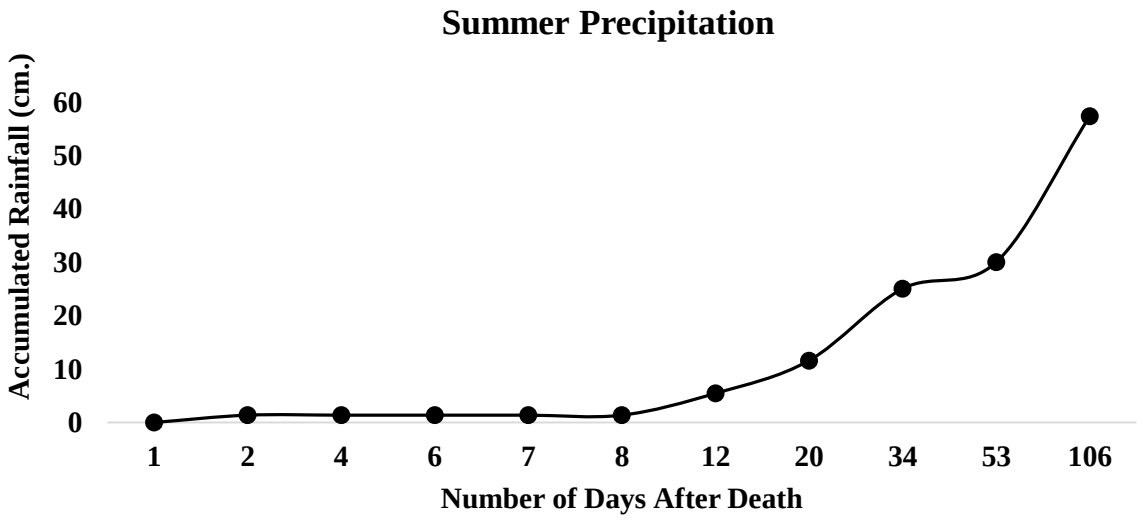

FIG. 16– Plot of accumulated rainfall throughout the summer study. The x-axis corresponds to the days that skin samples were collected from the carcasses.

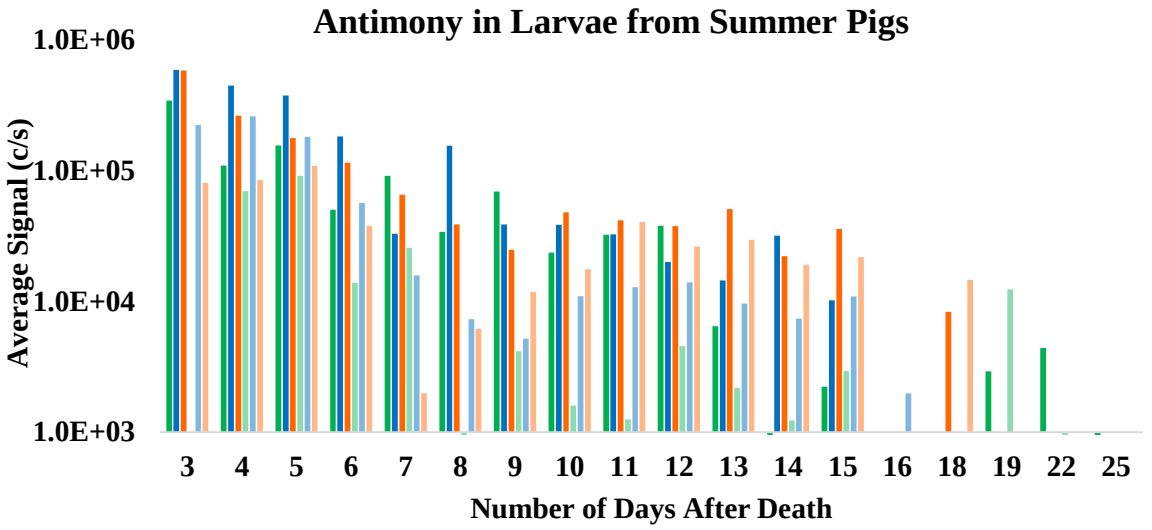

FIG. 17– Log plot of antimony signals in larvae feeding in and around the gunshot wounds (darker colors) and stab wounds (lighter colors) on the summer study, open field (green), river (blue), and tree (orange) carcasses.

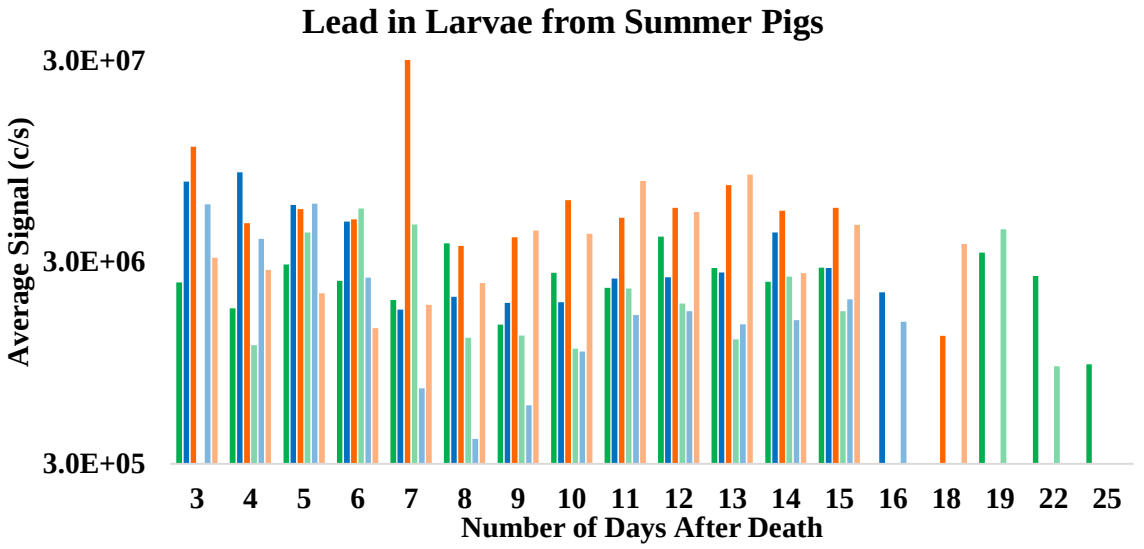

FIG. 18 – Log plot of lead signals in larvae feeding in and around the gunshot wounds (darker colors) and stab wounds (lighter colors) on the summer study, open field (green), river (blue), and tree (orange) carcasses.

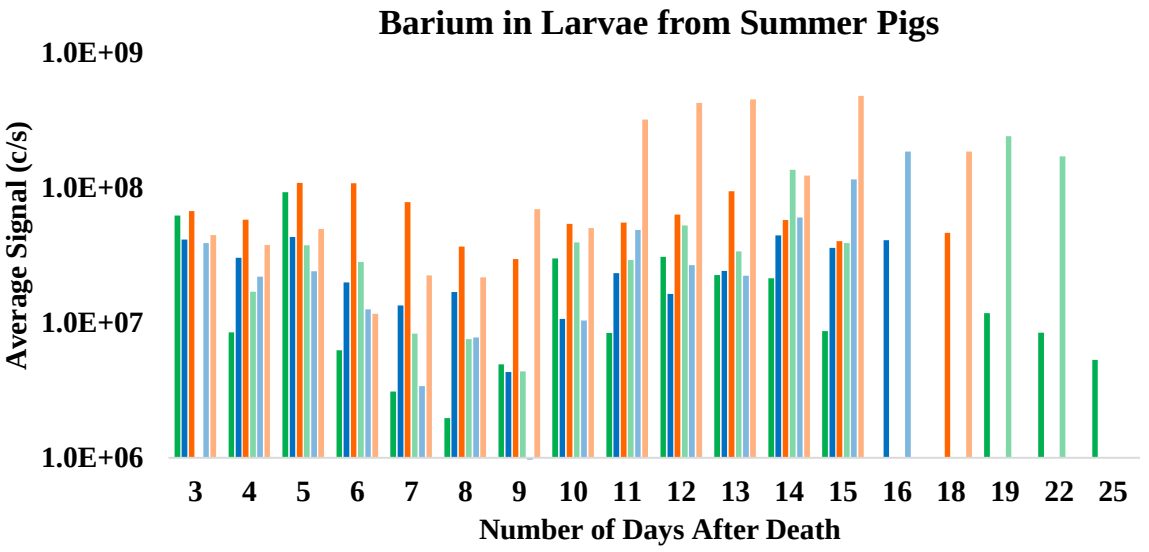

FIG. 19 – Log plot of barium signals in larvae feeding in and around the gunshot wounds (darker colors) and stab wounds (lighter colors) on the summer study, open field (green), river (blue), and tree (orange) carcasses.

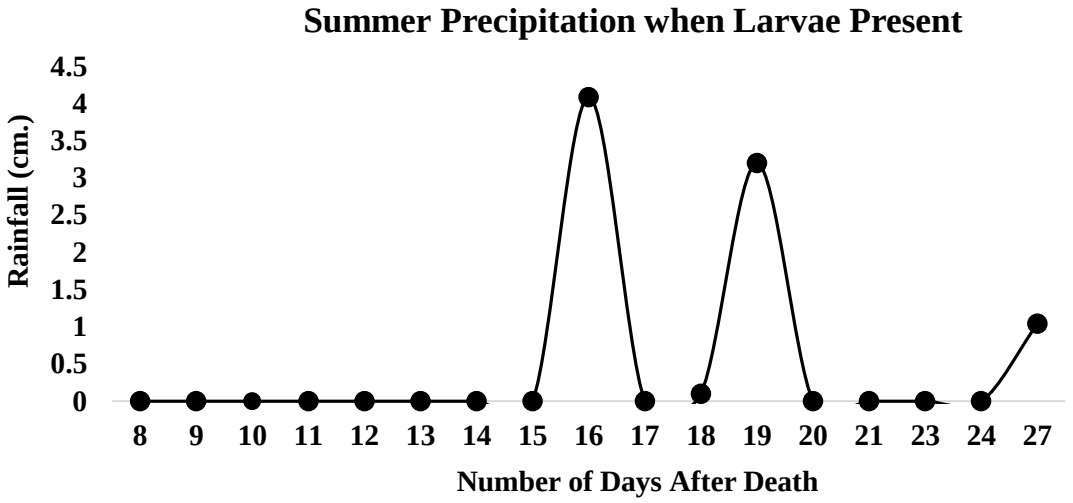

FIG. 20 – Plot of precipitation during the time larvae were present on the carcasses in the summer study. The x-axis corresponds to the days that larvae were collected from the carcasses.

TABLE 1—Instrument and laser parameters for the analysis of skin and larvae

	Trace Elements in Skin	Analysis of Skin	Analysis of Larvae
Outer gas flow	18.0 L Ar min^{-1}		
Auxiliary flow	1.80 L Ar min^{-1}		
Sampler and skimmer cones	Ni and Ni, CRI configuration (Analytik Jena)		
Scan mode	Peak hopping		
Dwell time	10 ms	10 ms	1 ms
RF Power	1400 W		
Torch position, ion optics	Optimized for maximum sensitivity and stability		

100 fs Laser	Coherent Libra Ti:Sapphire		
Operational wavelength	266 nm		
Laser energy	130 mW $pulse^{-1}$; Filtered to 17 mW $pulse^{-1}$		
Frequency	1000 Hz		
Spot size	~70 µm		
Raster speed	150 µm sec^{-1}		
Carrier gas flow rate through cell (L He min^{-1})	1.02	1.06-1.09	0.89-1.04
Additional carrier gas (T in after cell) (L Ar $min^{-1)}$	0.93	1.18-1.25	0.83-0.94

CHAPTER 5. DETECTION OF BULLET RESIDUE IN BONES AND SOIL FROM DECOMPOSED PIG CARCASSES WITH RADIOGRAHY, MICRO-COMPUTED TOMOGRAPHY, AND X-RAY K-EDGE DENSITOMETRY

Jonna Berry, Scott Wendt, R. S. Houk, and J. N. Gray

Will be submitted to *The Journal of Forensic Science*

Abstract

Identifying gunshot trauma on skeletonized remains is important, yet difficult, in forensic investigations. Detection of bullet residue within bone would assist in distinguishing gunshot wounds on skeletonized remains. Pig carcasses were inflicted with gunshot wounds postmortem and placed outside to decompose for either 4 or 11 months. After decomposition, radiographic images of the pig bones containing possible damage from bullets revealed metallic particles embedded within a number of bones. Radiographs of soil from bones containing projectile trauma also contained metallic particles. Micro-CT scans of select bones provided volumetric information of metallic particles and smaller particles were also detected. Metallic particles within the bones were analyzed with x-ray, K-edge densitometry and determined to contain lead. Studies on bullet residue mostly concern human or animal samples in a good state of preservation. Little radiochemical and microscopic research has been conducted regarding the analysis of gunshot wounds on decomposing remains. This study indicates that bullet residue can be retained throughout decomposition and detection of bullet residue within bones would provide valuable information when determining the cause of death.

Introduction

Determining the type of trauma present on a recovered body, i.e. sharp force, blunt force, or projectile trauma, is important in forensic investigations to establish the cause of death. The current method to distinguish projectile trauma from other trauma is by the detection of gunshot residue (GSR) around the wound. GSR is airborne vaporized particles formed from the combustion of the primer and propellant. Molten GSR particles are ejected through the gun muzzle, cool rapidly into liquid droplets, and subsequently solidify (1). GSR particulates usually range in sizes from 0.5 µm to 10 µm in diameter (1). One composition consistent with GSR particles is a combination of lead, barium, and antimony in an individual particle (1). Copper and iron have also been detected in GSR particles associated with propellant/primer (2). GSR from the bullet itself are irregularly shaped fragments formed as it breaks up upon impact. These fragments range in size from 50 microns to several millimeters length and/or width. The presence of many tiny particles is especially true for skeletal cadavers with bones shattered by the bullet, where the small fragments can be tightly embedded in the bone matrix. As a body decomposes, bullet fragments initially embedded within muscle and tissue may settle in the soil below the remains as well. Skeletal remains are difficult to assess and generally bullet fragments remain only in or near the damaged bone.

GSR particles settle in and around the gunshot wound. GSR has also been detected on bone, below the subcutaneous tissue immediately after shooting (3). The outer membrane of the bone, the periosteum, is uplifted when a bullet penetrates the bone exposing it to GSR (4). Berryman *et al.* hypothesized that a low pressure gas zone exists behind the bullet which draws vapor and GSR in during passage through an object,

and distributes it throughout the wound tract and eventually onto the exposed bone under the periosteum. This hypothesis is further supported by the detection of GSR on the bottom of discharged bullets, including some which were severely deformed and recovered from skulls and walls at crime scenes (5).

Characterization of gunshot wounds is one of the widest fields of research in forensic medicine. However, studies on GSR and bullet residue mostly concern human or animal samples in a good state of preservation (6). Unfortunately, little radiochemical and microscopic research has been conducted regarding the analysis of gunshot wounds on decomposing remains (7, 8, 9) and even less literature exists for gunshot wounds on skeletonized remains (3, 9). Projectile trauma is difficult to identify on skeletal remains when typical projectile fracture patterns are not present (3). A few studies have identified GSR and metallic fragments from the bullet retained in the bones during decomposition. In one study, GSR was observed in four out of nine pig skulls containing gunshot wounds after decomposing for 4 years (9). In a second study, GSR particles were detected in 4 cases of buried, charred, or submerged remains, along with the remains of a historical First World War soldier (6). In both studies, GSR persisted even after long periods of decomposition and preservation in peculiar environments.

GSR particulates formed from the combustion of the primer, propellant, and other sources of the weapon usually range in sizes from 0.5 μm to 10 μm in diameter (1). Particles of this size are too small to image with radiography or to determine the composition of with K-edge, x-ray densitometry. Therefore, the particles analyzed in this work are most likely the fragments torn from the bullet as it passed through the bone. These fragments will be referred to as bullet residue in this study. Lead particles from bullet residue are expected to be more abundant around projectile trauma from non-

jacketed bullets (2). However, this study indicates that lead particles can be identified in bones shot with a copper jacketed bullet as well.

The present work evaluates three x-ray techniques for the detection of bullet residue in skeletonized remains. First, radiographic images of bones and the soil surrounding the bones were taken to determine if bullet residue was present. Second, if high density particles were visible, micro-computed tomography (μCT) was performed on several of the bones in order to obtain high resolution spatial and morphological information about the particles. Finally, to positively determine the metallic composition of the bullet residue particles detected within the bone, x-ray K-edge densitometry was performed on select bones.

Metallic lead particles, such as bullet residue, are radiopaque and easily observed in radiographs (10, 11). When a victim is discovered recently after death with possible gunshot injuries, postmortem radiographs are conducted to locate the projectile, depict the bullet track, and assist in retrieval of the bullet and bullet fragments (10). In a study by Lantz *et al.*, (11) radiopaque bullet residue was observed in a radiograph around the entrance wound of a victim shot by a .22 caliber rifle. The bullet residue was analyzed with scanning electron microscopy-energy dispersive x-ray spectroscopy (SEM-EDX) and lead was determined to be the predominant element present (11).

High resolution x-ray imaging, either micro radiography or micro-CT, is a non-destructive radiological technique used to investigate small, centimeter sized objects with spatial resolutions as small as 5 microns. This technique has been used as an objective and rapid tool for estimating the firing distance in intermediate-range gunshot wounds by the detection of GSR within the tissue (12). Micro-CT was also used to detect GSR on remains that were decomposed or severely charred by fire to differentiate entrance wounds from exit wounds (12, 13).

K-edge absorption densitometry is capable of detecting heavy metals and has been used to measure and monitor uranium and plutonium in facilities around the world (14). In K-edge densitometry analysis, a white x-ray beam is passed through a sample to a collimated energy-sensitive x-ray detector, such as a high purity germanium detector with a multichannel analysis capability. Figure 1 shows the x-ray absorption coefficient for lead plotted as a function of photon energy. A discontinuous sharp increase in the absorption coefficient is observed at a photon energy of 88 keV. This increase results in an abrupt decrease in transmission rate of photons through the material, resulting in a step edge at a particular photon energy of the transmitted x-ray spectrum (15), see Figure 9a. Each element has a large change in the absorption coefficient at a unique photon energy corresponding to the binding energy of the 1s electrons. The presence of a K-edge at a particular photon energy identifies the unique element while the size of the jump is related to how much of the element is present. K-edge densitometry is capable of simultaneously measuring multiple heavy metals present in various materials.

Experimental

This work involved a winter and summer study. In both studies, pig carcasses were inflicted with gunshot wounds 1 to 3 hours postmortem. All carcasses were euthanized for other reasons prior to use in this study. Carcasses were then placed outside in large mesh cages for a period of time to decompose. The mesh cages were to keep large animals out while allowing insects to access the remains. These carcasses, along with carcasses containing stab wounds, were also used in another study to investigate the retention of GSR in tissue and within larvae feeding around the wounds during decomposition.

Four pig carcasses (~60-115 kg) were each shot 15 times by Ames Police Department detectives with a Sig Sauer .40 caliber handgun and Winchester SXT 180 grain bonded hollow point jacket ammunition. The handgun was cleaned with a Bore Snake in between each shot and held approximately 30 cm away from the carcass for each shot. Adjacent gunshot wounds were separated by a minimum of 13 cm. After the gunshot wounds were inflicted, the carcasses were placed in mesh cages outside to decompose. Mesh cages were constructed from hog panel and covered with 6 mm wire mesh. The sides of the cages were buried 15 to 25 cm deep into the soil to prevent animal scavengers from burrowing under the cages to access the carcasses.

In the winter study, one pig carcass (~60 kg) was shot and placed outside in a mesh cage to decompose in November 2013. The bones were collected after 306 days of decomposition. In the summer study, three pig carcasses (~115 kg) were each shot and place outside in mesh cages to decompose in June 2014. In order to determine whether different environments affected the retention and detection of metallic particles from the bullet in the bones, carcasses were placed in separate outside environments on a farm.

One pig carcass was placed near a river bank, another in a forested area, and the third carcass was placed in an open field. The bones from the summer study carcasses were collected after 143 days of decomposition.

The bones from each carcass were collected and placed in 18 gallon plastic containers. Bones were stored in a laboratory and allowed to dry for 84 days for the winter carcass and 48 days for the summer carcasses. After the bones and any organic matter on the bones were dried, the organic matter was cleaned off of the bones from the summer carcasses with toothbrushes and a nail brush to avoid metal contamination. The bones from the winter study carcass had little residual organic matter and did not require cleaning.

Radiographs were taken of bones that showed damage, possibly from a bullet, to look for indications of metallic fragments. Soil that had fallen off of the bones from the carcass containing gunshot wounds and the carcass containing stab wounds from the winter study was collected from the bottom of the plastic containers. Digital x-ray images of the damaged bones and collected soil were captured using the high resolution CT facility at the Center for Non-Destructive Evaluation (CNDE). The micro-CT system is comprised of a Kevex micro-focus x-ray tube (130 kV, 4 μm diameter spot), 4-axis micro-step positioner and digital array detector. The detector is a General Electric DXR500L amorphous silicon flat panel detector with a CsI conversion screen. GE Rhythm data collection software generates the digital images. The CT system can generate both high resolution (2 micron) digital radiography and 3D CT data at 3 micron voxel sizes to be performed.

CT scans were subsequently performed on bones that contained numerous high density particles, typical of Pb fragments. High-speed CT reconstruction was done using

custom reconstruction software, and custom image analysis software was used for visualizing the 2D and 3D data sets. The visualization software is capable of isolating the high contrast particles from the bones in order to obtain better morphological information. The isolated objects can be exported and saved as virtual 3-D objects defined in a standard computer aided drafting (CAD) format.

A third type of x-ray scan, a K-edge densitometry measurement, was also performed on bones with relatively large fragments (~0.5 mm in width) to determine their elemental composition. For this scan, an energy dispersive x-ray detector was used to positively identify the high density indications observed in the radiographs as Pb fragments. The system is comprised of a standard 3.2 kW industrial Comet x-ray tube (320kV, 1.5 to 3 mm diameter spot), an x-z-theta multi-axis sample positioner and a high purity germanium (HPGe) detector coupled to a multi-channel analyzer (MCA). This x-ray photon counting detector measures x-ray spectra that can be used to identify metal particles based on the presence of a step edge in the Bremsstrahlung spectrum. As discussed above, each element has a specific energy at which this edge occurs. When Pb is present within the area irradiated with x-rays a sharp step edge in the measured Bremsstrahlung spectrum at 88 keV is observed.

Results and Discussion

Decomposition of Carcasses

The carcass from the winter study was in the desiccation stage of decomposition when the bones were collected (Fig. 2). The bones contained a light layer of dirt and were not cleaned before analysis. The carcasses from the summer study were in between

the end of the advanced stage of decomposition and the beginning of the desiccation stage (Fig. 3). Organic matter from the decomposing carcasses was present on all of the bones and was cleaned off before further analysis.

X-Ray Imaging of Bones and Soil

Radiographic images were taken of 35 bones containing fractures that may have been caused by a bullet projectile. Metallic radiopaque particles were identified in 29 of the 35 bones. A summary of the number of metallic particles identified in each bone or bone fragment is found in Table 1. Example radiographs of a few bones and bone fragments are shown in Figures 4-6. Many of the metallic particles clustered near fracture areas are most likely GSR, or metallic particles from the bullet itself which were deposited on and within the bone as the bullet passed through, also known as, bullet residue.

More metallic particles were identified on bones from the winter carcass compared to the summer carcasses. This may be because the bones from the carcass in the winter study were covered with only a slight layer of dirt when collected from the field and were not cleaned. Many of the bones from the summer study were partially to fully covered in organic matter from the decomposing carcasses. The organic matter was brushed off with a nail or tooth brush and bullet residue may have been removed during this process. On day 25 of the summer study, 4 cm of rainfall caused the river near the farm to flood and the carcasses placed under the trees and in the open field were submerged under approximately 50 cm of flowing water for an unknown period of time (less than 24 hours). The cleaning and immersion events may have contributed to fewer particles being observed in the bones from the summer carcasses compared to the winter

carcass. However, even after these events, significant and easily detectable Pb bullet fragments are still found, the retention of bullet residue within skeletonized remains is robust enough to withstand a long period of time and unpredictable events.

Fractured bones that did not contain metallic particles may have been broken during transport of the carcasses, or more likely, as the bullet passed through nearby bones and torsion caused them to fracture without ever coming in contact with the bullet.

Radiographic images of the soil which fell from the winter carcasses containing either gunshot wounds or stab wounds are compared in Figure 7. Numerous high contrast particles are observed in the radiograph of the soil from the bones of the carcass containing gunshot wounds (Fig. 7a). No high contrast particles are identified in the soil from the bones of the carcass containing stab wounds (Fig 7b). The two carcasses were both placed in mesh cages and located only 3 feet from one another. The high contrast particles observed in the soil from the gunshot carcass are most likely metallic fragments from the bullets. These results indicate soil around the bones, and potentially the soil directly below the carcass may also contain bullet residue. As a body decomposes, bullet fragments initially embedded within muscle and tissue may settle in the soil below the remains and should be considered for analysis when determining the type of trauma present on skeletonized remains.

µCT of Bones

µCT scans of "Fragment 1" from the left scapula of the carcass from the winter study were performed. A CAD image of the metallic particles extracted from the bone was created (Fig. 8). Morphological information of the metallic particles embedded within the bone is available from the µCT scans. The three large particles embedded within the bone fragment are irregularly shaped, not spherical (Fig. 8). GSR particles

from the primer combustion are known to be spherically shaped. However, the irregular shape observed from the particles embedded within bone is consistent with irregular shapes formed from the mechanical destruction of the bullet as fragments are torn off during passage. This is another indication that the particles embedded within the bones are fragments from the bullet and not GSR from the primer.

CT provides better image resolution compared to radiographic 2D images and numerous smaller metallic particles are observed in the CAD image extracted from the CT scan of the bone fragment (Fig. 8). In the original x-ray image of "Fragment 1" of the left scapula from the carcass in the winter study, three lead fragment are observed. These three fragments are approximately 0.75 mm in width (Fig. 8a). In the CAD image from the CT scans, the three ~0.75 mm sized particles are observed, along with many otherwise undetected lead fragments on the order of 0.1 mm in diameter (Fig. 8b). The size of the particle that can be identified with CT is dependent on the spatial resolution of the detector. High resolution-CT is needed for imaging the smaller lead fragments (0.1 mm). Samples no larger than a few hundred square mm can be analyzed with high resolution-CT, therefore, an area containing possible projectile trauma may need to excised from larger bones before analysis.

X-ray, K-edge Analysis of Metallic Particles

Two bones and one bone fragment were analyzed with an energy dispersive x-ray, K-edge technique in order to determine the composition of the embedded particles observed in their radiographs. This technique will identify metals with relatively high atomic numbers, such as lead, if present in the particles. The bones for which x-ray, K-edge analyses were performed are shown in Figures 4-6. As mentioned, if a K-edge at 88 KeV is shown in the Bremsstrahlung spectrum then lead is present in the sample volume

irradiated by the x-rays. The edges in the spectra collected on the bullet residue particles indicates that lead is present in all of the metallic particles that were analyzed (Figs 9-11). For each bone analyzed, several additional x-ray spectra were collected within a few mm from the metallic particle to verify that no Pb K-edge was present (Figs. 9-11). This indicates that the Pb detected near the metal particles is from the particle itself and not from anything else. This is illustrated in Figure 12 which shows the result of a 2D raster scan of an area around one particular particle. An x-ray spectrum is collected at each location of the raster scan, and those spectra are available for later analysis.

The 2-dimensional raster scan shown in Figure 12 was performed with the germanium detection, K-edge system in a square area around particle #1 (labeled in Fig. 6) on "Vertebrae 2" from the carcass in the open field (Fig. 12). The scan has a very fine spatial resolution (~150 μm) in the horizontal direction, and a coarser resolution (~1 mm) vertically. A transmitted spectrum is collected for each pixel in the scan. The red and black areas correspond to the empty region just above the bone (Fig. 12) where the un-attenuated incident x-rays reach the detector and produce very high intensities. The lighter green areas are where the x-rays are passing through the relatively thin bone. The white, pink, and dark blue squares indicate areas where fewer photons are detected due to a denser object attenuating much of the x-ray beam (particle #1). This area corresponds to the lead fragment (#1) in the box on the radiograph in Figure 12 (also in Fig. 6). From this image, portions of the metallic particle are being detected in several grid locations of the raster scan covering an area that is approximately 0.25 mm wide by 0.5 mm long (Fig. 12). Due to the presence of an edge at 88 keV in the x-ray spectrum (Fig. 11a) from this particular metallic particle, the energy dispersive measurement proves that the suspect particle is indeed a lead fragment, most likely from a bullet fragment.

All particles analyzed with the K-edge system were at least partially composed of lead (Figs 8-11). From the particles' location around damaged bone, the irregular morphology, and lead composition, it can be assumed that these particles are bullet fragments. It must be noted that lead particles are also created from other sources such as: leaded petrol emissions, plumbing materials, battery plates, solder, glass, and paints, (1) however, it is unlikely that metallic lead from some other source would be found embedded within skeletonized remains, particularly in the vicinity of bone damage. Animal scavenging of a carcass can break bone but will not result in Pb becoming embedded in the bone.

Unfortunately, the K-edge system at CNDE is not optimized to perform K-edge scans needed to locate and identify small Pb fragments in bone. More specifically, the imaging capability is separate from the K-edge system and it is difficult to locate the particle for K-edge analysis. K-edge analyses on the CNDE system required up to 18 hours for a detailed scan. Therefore, only a few bones were analyzed with the x-ray, K-edge technique. However, particles from the remaining bones were embedded near fractures and have similar high density radiographic features. These particles most likely contain lead bullet fragments.

Lead particles are expected to be more abundant around projectile trauma from non-jacketed bullets (2). However, this study indicates that lead particles can be identified in bones shot with a copper jacketed bullet as well. Antimony and barium are also present in primer GSR (1); however, the presence of these elements could not be determined. This is probably because the concentrations are below the level that can be detected by K-edge densitometry. Elements with lower atomic numbers become harder

to detect because the K-edges are at lower energies where more photons are absorbed in the bone and therefore, fewer low energy photons reach the detector. At these photon energies, the K-edges cannot be distinguished from the noise. In general, elements with lower atomic masses (below ~140) are difficult to detect, especially at low concentrations. However, it is unlikely that these fragments contained antimony or barium being that these fragments are from the bullet itself and not from the primer.

This study indicates that bullet residue remained embedded within and on the bones for 306 days of decomposition throughout the winter study. In the summer study, carcasses decomposed for 143 days, the carcasses in the trees and open field were submerged underwater in a flood for a day, and the bones from all three carcasses were cleaned with a nail brush or tooth brush, yet bullet residue was still retained and identified in some of the bones.

A typical collection method for skeletonized remains from a crime scene is to collect the bones in paper bags for transfer. The soil directly underneath any bone trauma may contain bullet residue and could be collected for analysis as well. It would be advantageous for the soil and debris to be broken down into fine particulates and imaged in a thin layer. This would increase the chances of detected any small lead fragments by minimizing the contrast effects produced by larger soil particles. A forensic advantage of identifying bullet fragments in skeletonized remains with this method is that the bones can be imaged with x-ray radiography without removing the bag and disturbing the evidence. If bullet residue is not observed, the bone could then be cleaned with a brush and the bone and removed soil could be imaged separately in an effort to find very small particles that may have been obscured. Any bones containing metallic fragments in the vicinity of bone trauma could be sent for further analysis to determine the composition of

the metallic fragments. Techniques such as K-edge densitometry or laser ablation-inductively coupled plama-mass spectrometry (LA-ICP-MS) could determine if the particles are composed of lead with little to no sample destruction. If lead fragments are detected around the vicinity of bone trauma it is very likely the fragments embedded within the bone are from a bullet and would provide valuable information when determining the cause of death.

Conclusion

Radiographic images of pig bones containing possible bullet trauma revealed bullet residue on 29 of the 35 bones imaged. The bones from the summer study contained less GSR and bullet residue than the bones from the carcass in the winter study, most likely because the summer bones were cleaned and some were submerged underwater in a flood. Radiographic images of the soil from the bones of the winter carcass containing gunshot would revealed numerous metallic particles, most likely from the bullets, compared to the soil from the bones of the stabbed carcass.

Micro-CT allowed for morphological information of the particles which showed irregular shapes indicative of mechanical tearing of the bullet fragments. Smaller particles were also visible with the micro-CT method. The bullet residue particles were determined to contain some amount of lead with x-ray K-edge densitometry.

Little research has been conducted on the retention of bullet residue on and within skeletonized remains. This pilot study demonstrates the potential for bullet fragments to be detected on skeletonized remains to aid in the identification of projectile trauma. This methodology is completely non-destructive; the entire samples remain intact after the analysis which is advantageous in forensic work. Identification of projectile trauma on

skeletonized remains would be important in forensic investigations in order to assist in determining the cause of death.

Acknowledgements

Research at the Ames Laboratory was supported by the National Institute of Justice Graduate Research Fellowship (Award No. 201-IJ-CX-0012). The authors would like to extend our greatest appreciation to the Ames Police Department for their cooperation, and for their time and ammunition. The ISU Swine Farm provided the carcasses for this study. The mesh cages and some equipment for this study were borrowed from the ISU College Shop. The Ames Laboratory is operated for the U.S. Department of Energy by Iowa State University under Contract No. DEAC02-07CH11358.

References

1. Dalby O, Butler D, Birkett JW. Analysis of gunshot residue and associated materials--a review. J Forensic Sci 2010;55(4):924-943.
2. Udey RN, Hunter BC, Smith RW. Differentiation of bullet type based on the analysis of gunshot residue using inductively coupled plasma mass spectrometry. J Forensic Sci 2011;56(5):1268-1276.
3. Berryman HE, Kutyla AK, Davis JR. Detection of gunshot primer residue on bone in an experimental setting--an unexpected finding. J Forensic Sci 2010;55(2):488-491.
4. Faller-Marquardt M, Bohnert M, Pollak S. Detachment of the periosteum and soot staning of its underside in contact shots to the cerebral cranium. Int J Legal Med 2004;118:343-347.
5. Bergman P, Enzel P, Springer E. The Detection of gunshot residue (GSR) particles on the bottom of discharged bullets. J Forensic Sci 1988;33(4):960-968.
6. Amadasi A, Gibelli D, Mazzarelli D, Porta D, Gaudio D, Salsarola D et al. Assets and pitfalls of chemical and microscopic analyses on gunshot residues in skeletonized bodies: a report of five cases. Int J Legal Med 2014.
7. LaGoo L, Schaefer LS, Szymanski DW, Smith RW. Detction of gunshot residue in blowfly larvae and decomposing porcine tissue using inductively coupled plasma mass spectrometry (ICP-MS). J Forensic Sci 2010;55(3):624-632.

8. Roeterdink EM, Dadour IR, Watling JR. Extraction of gunshot residues from the larvae of the forensically important blowfly claaiphora dubia (Macquart) (Diptera: Calliphoridae). Int J Legal Med 2004;118:63-70.
9. Taborelli A, Gibelli D, Rizzi A, Andreola S, Brandone A, Cattaneo C. Gunshot residues on dry bone after decomposition--a pilot study. J Forensic Sci 2012:57(5):1281-1284.
10. Brogdon BG. Forensic radiology. Boca Raton: CRC Press, 1998.
11. Lantz PE, Jerome GW, Jaworski JA. Radiopaque deposits surrounding a contact small-caliber gunshot wound. Am J Foren Med Path 1994:15(1):10-13.
12. Fais P, Giraudo C, Boscolo-Berto R, Amagliani A, Miotto D, Feltrin G et al. Micro-CT features of internediate gunshot wounds severly damaged by fire. Int J Legal Med 2013;127:419-425.
13. Cecchetto G, Amagliani A, Giraudo C, Fais P, Cavarzeran F, Montisci M et al. MicroCT detection of gunshot residue in fresh and decomposed firearm wounds. Int J Legal Med 2012;126:377-383.
14. Aljundi T, Jensen T, Gray JN. Heavy metal contamination detection using x-rays. Quant Nondes Eval 1996;15:465-472.
15. Jensen T, Aljundi T, Gray JN. Using x-ray, K-edge densitometry in spent fuel characterization. Proceedings of the Topical Meeting on the DOE Spent Nuclear Fuel and Fissile Materials Management; Charleston, SC, 1998.

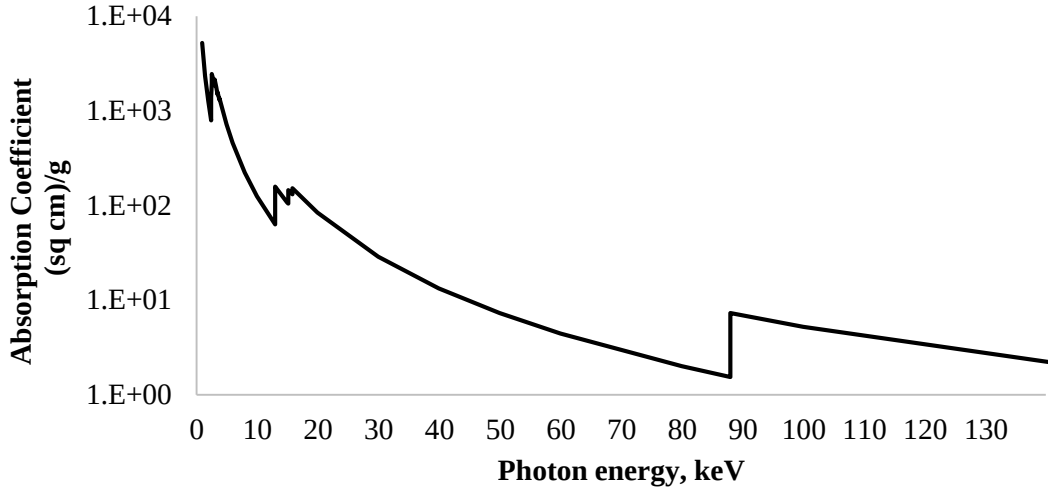

FIG 1—Absorption coefficient plot for lead (Pb), the K-edge is observed at 88 keV. The discontinuities at the left are L-edges and correspond to the 2s and 2p electron binding energies of the lead atom.

FIG 2—Images of the winter carcass a) ~4 hours after death. and b) when the bones were collected, 306 days after death (bottom).

FIG 3—Images of the summer carcass left in the trees a) ~6 hours after death, and b) when the bones were collected, 143 days after death (bottom).

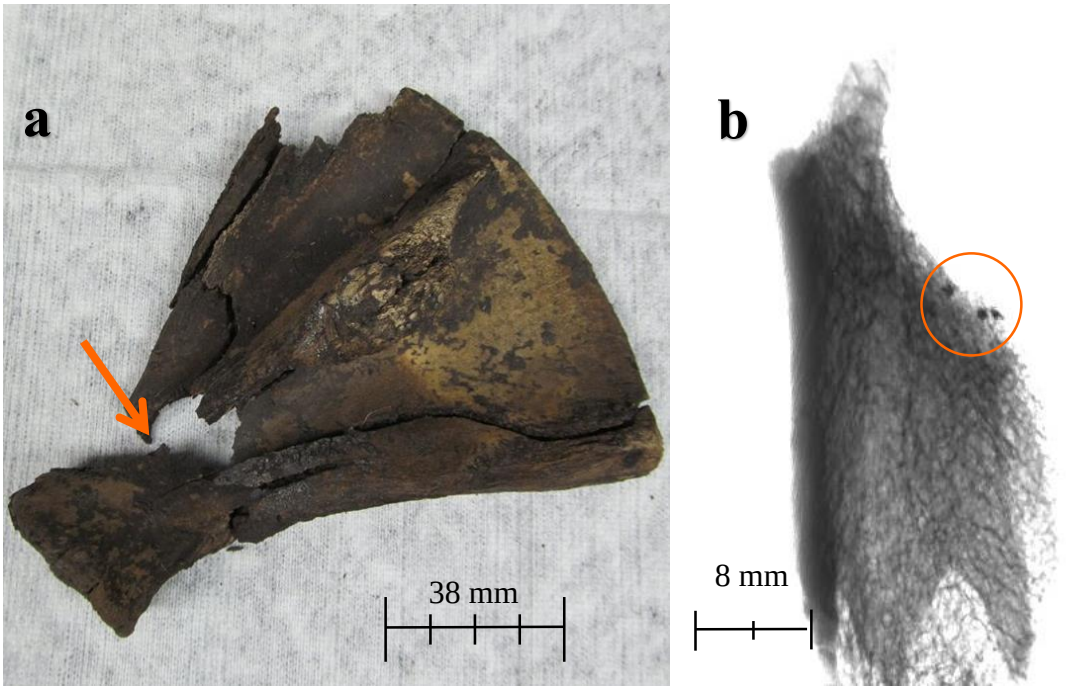

FIG 4—a) - Image of seven fragments of the left scapula from the winter carcass. The arrow in the left image indicates the fragment that is depicted on the right ("Fragment 1" from Table 1); 4b) X-ray radiograph of the "Left Scapula Fragment 1" from the winter carcass, the three dark spots in the circle are the metallic lead particles.

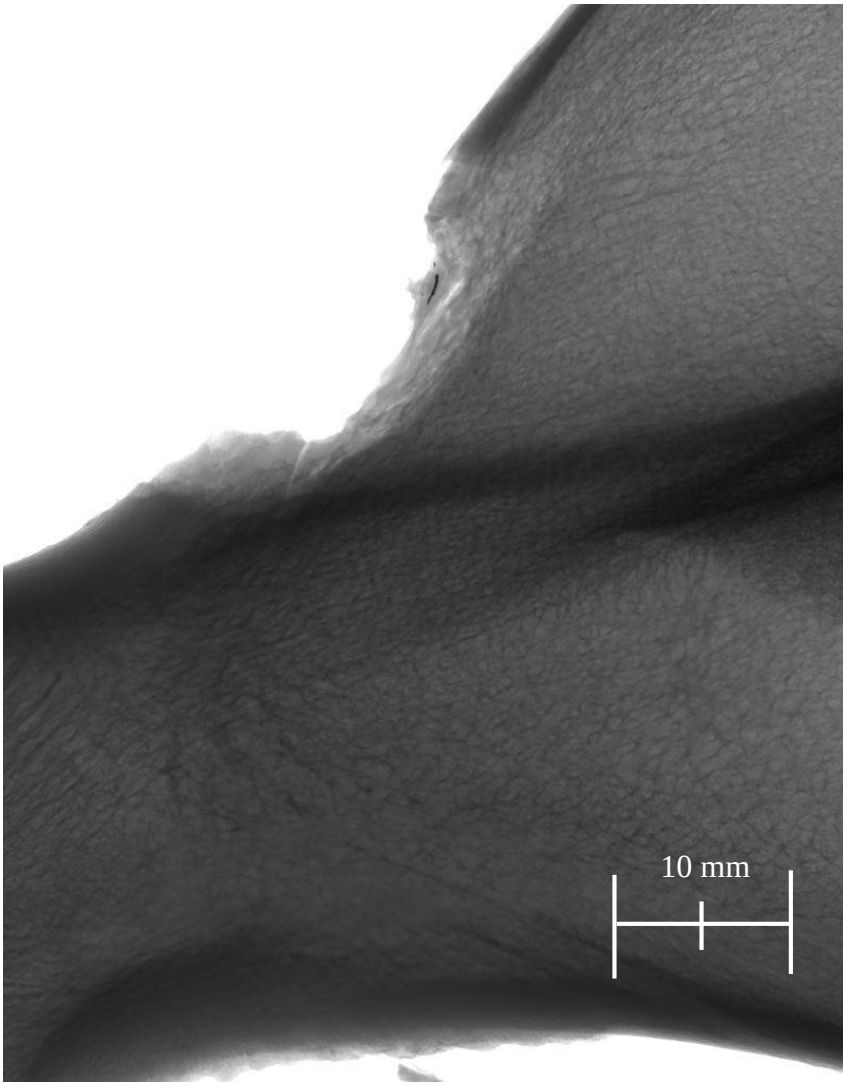

FIG 5—X -ray radiograph of "Right Scapula" from the winter carcass. The dark line in the circle is several metallic particles.

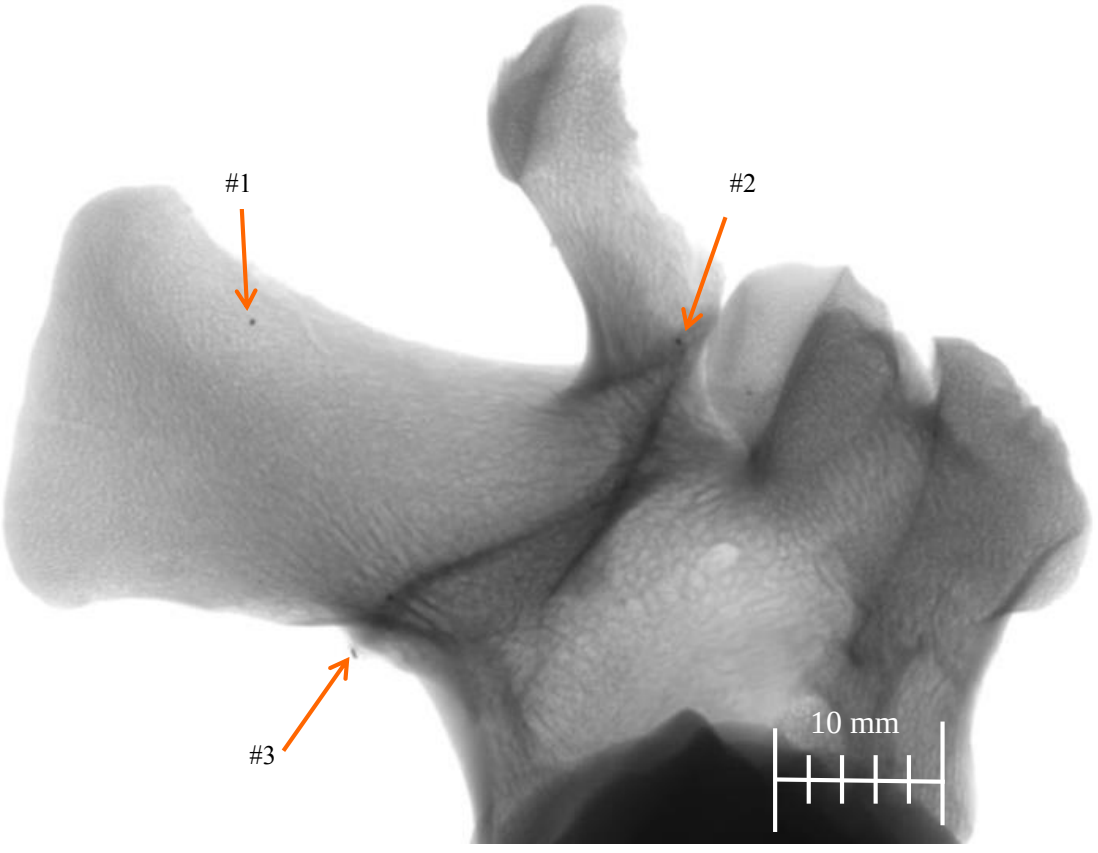

FIG 6—X-ray radiograph of “Vertebrae 2” from the summer carcass in the open field. The arrows indicate the metallic particles (dark spots) and are labeled #1, #2, and #3 for reference in the text and in Fig.9.

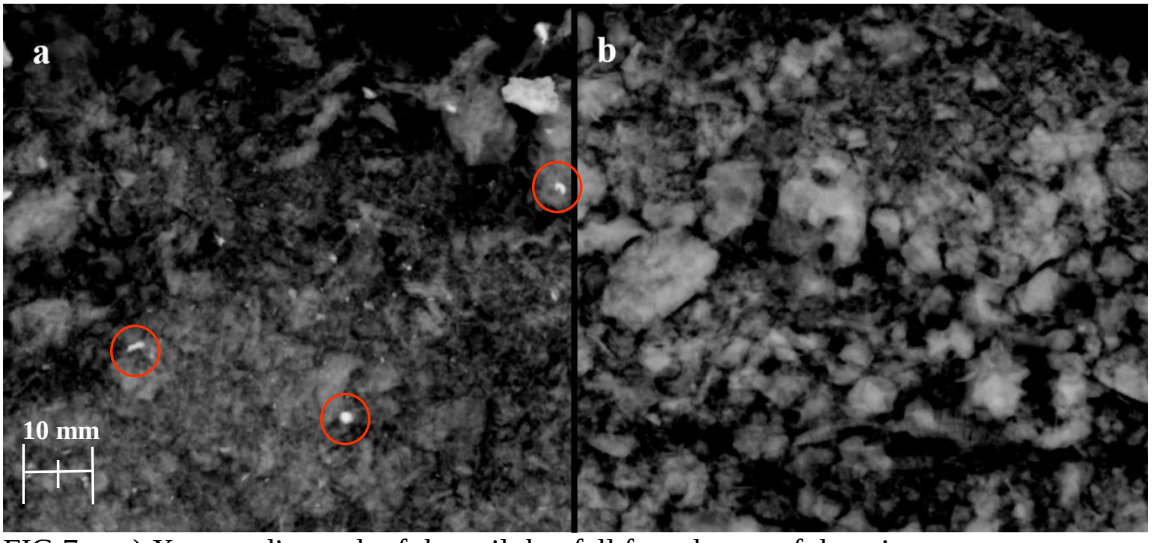

FIG 7— a) X-ray radiograph of the soil that fell from bones of the winter carcass containing gunshot wounds. The lighter spots are the metallic lead particles (some circled in orange) b) X-ray radiograph of the soil that fell from bones of the winter carcass containing stab wounds.

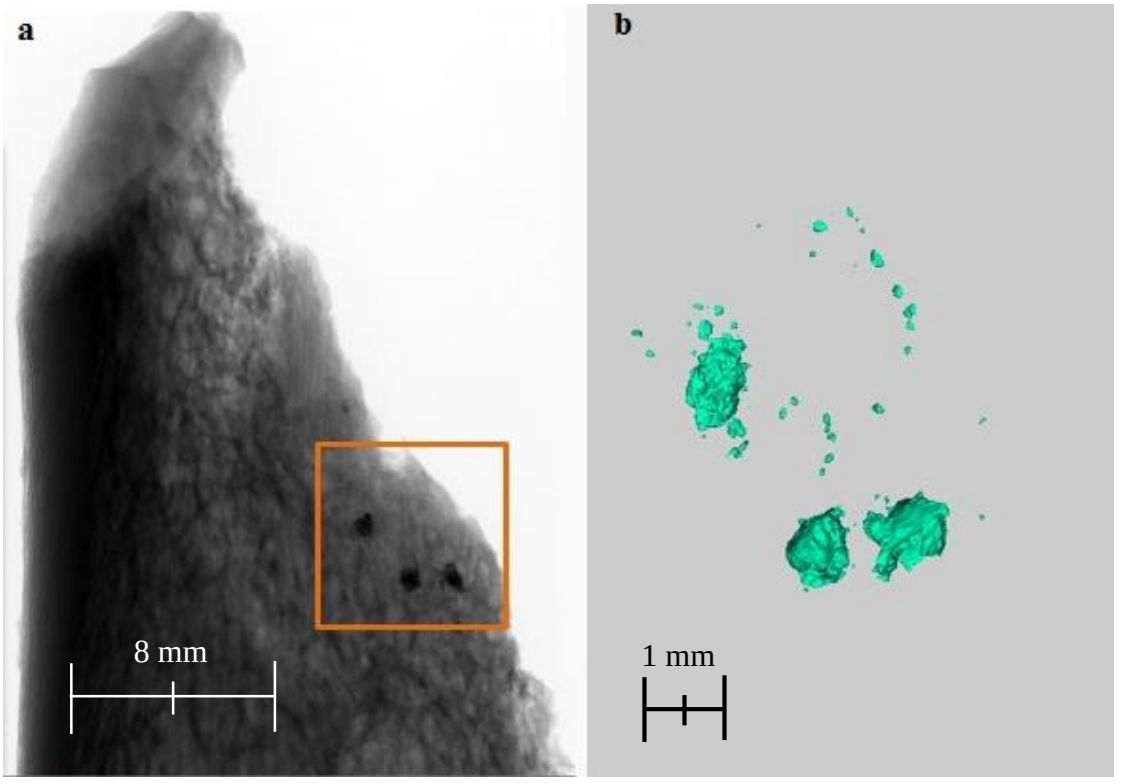

FIG 8— a) Zoomed X-ray radiograph of the "Left Scapula Fragment 1" from the winter carcass. The three dark spots in the box are the metallic lead particles; b) Particles were isolated from the bone in CT analysis revealing many additional tiny fragments.

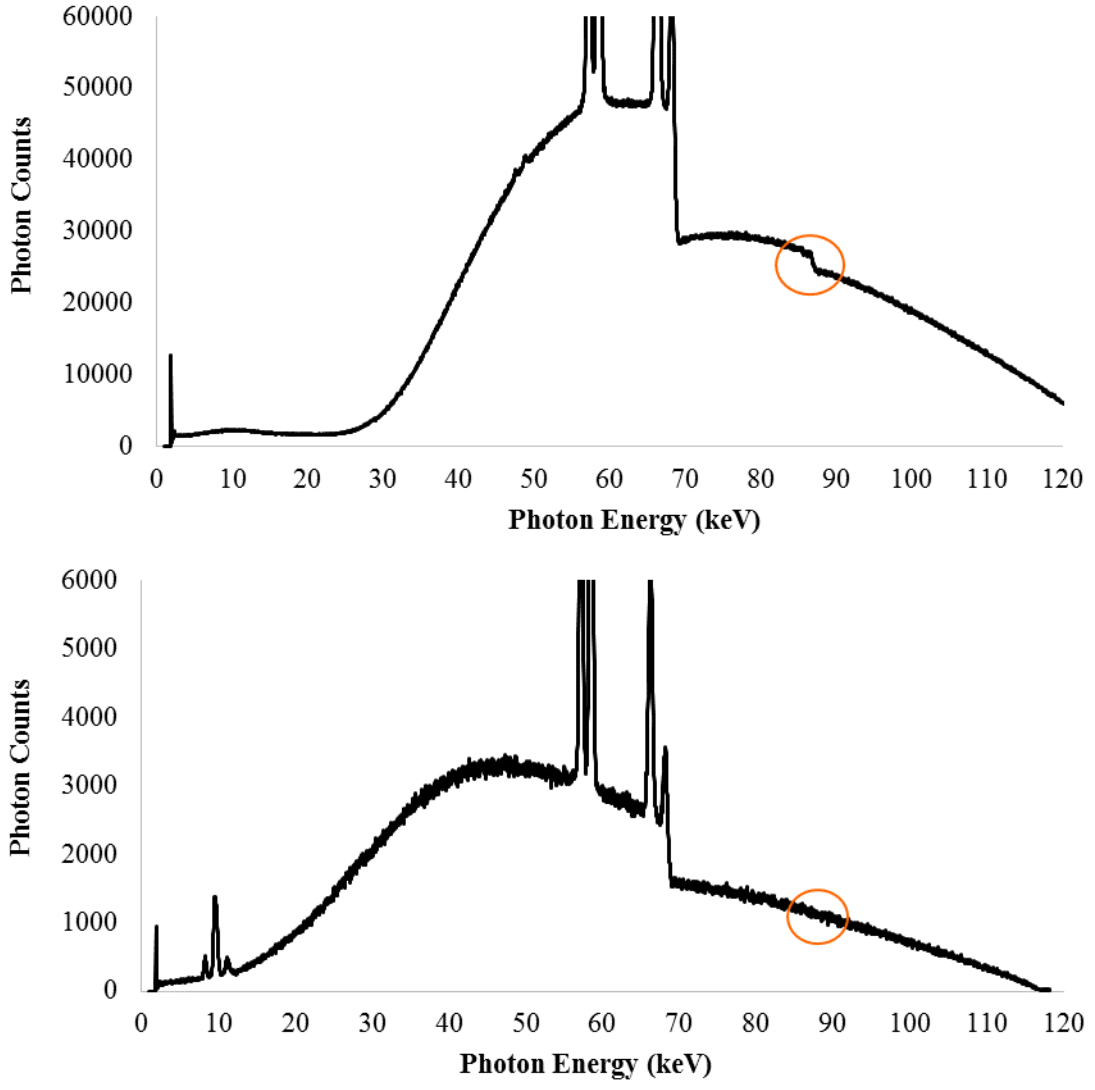

FIG 9—X-ray Bremsstrahlung spectrum of metallic particle in the "Left Scapula Fragment 1" from the Winter carcass (top) and the similar spectrum of an area of the bone 4 mm away from metallic particle (bottom). The area circled on both plots is the photon energy at which the K-edge is located if lead is present.

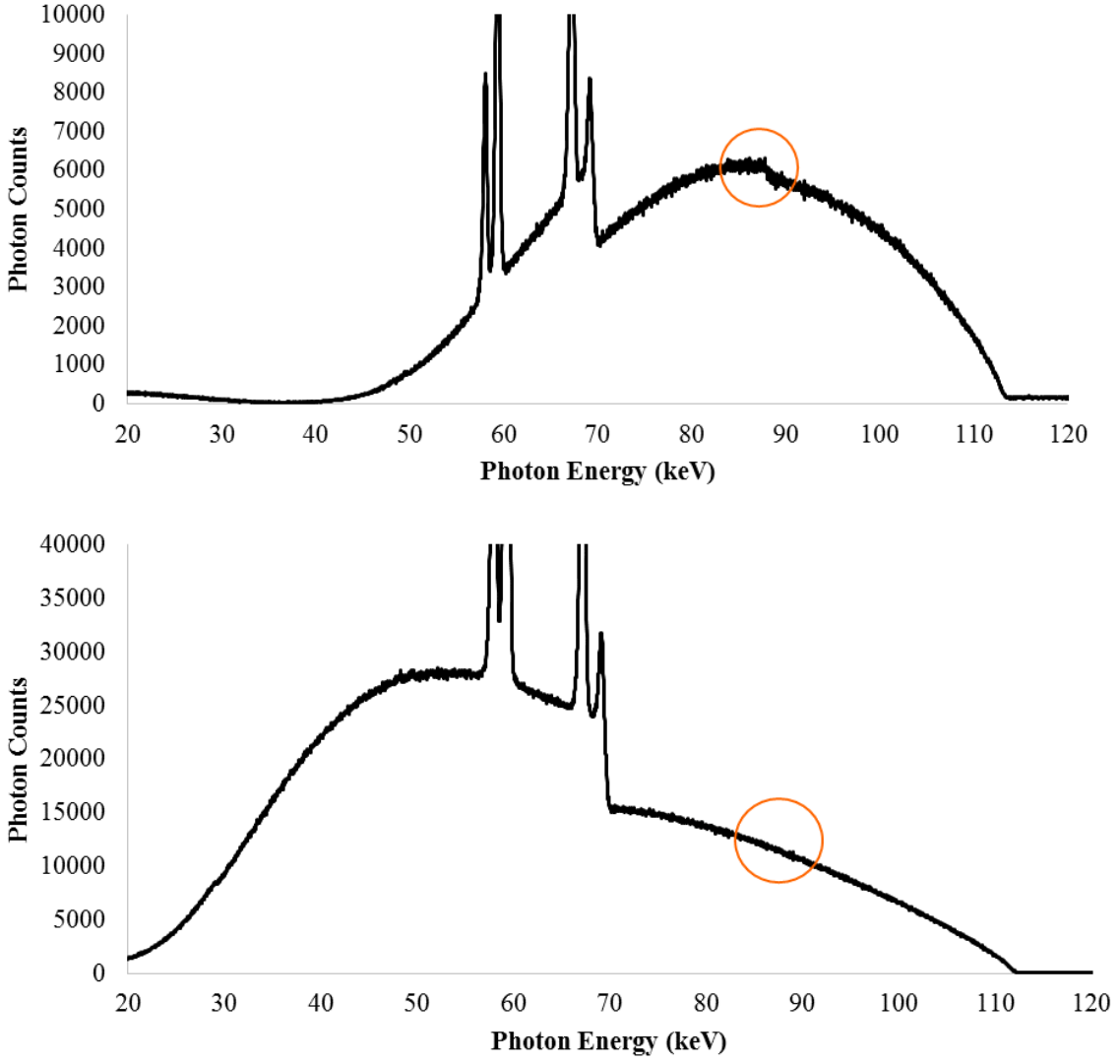

FIG 10—X-ray Bremsstrahlung spectrum from metallic particle in the "Right Scapula" from the Winter carcass (top) and a similar spectrum from an area of the bone 2 mm away from metallic particle (bottom). The area circled on both plots is the photon energy at which the K-edge is located if lead is present.

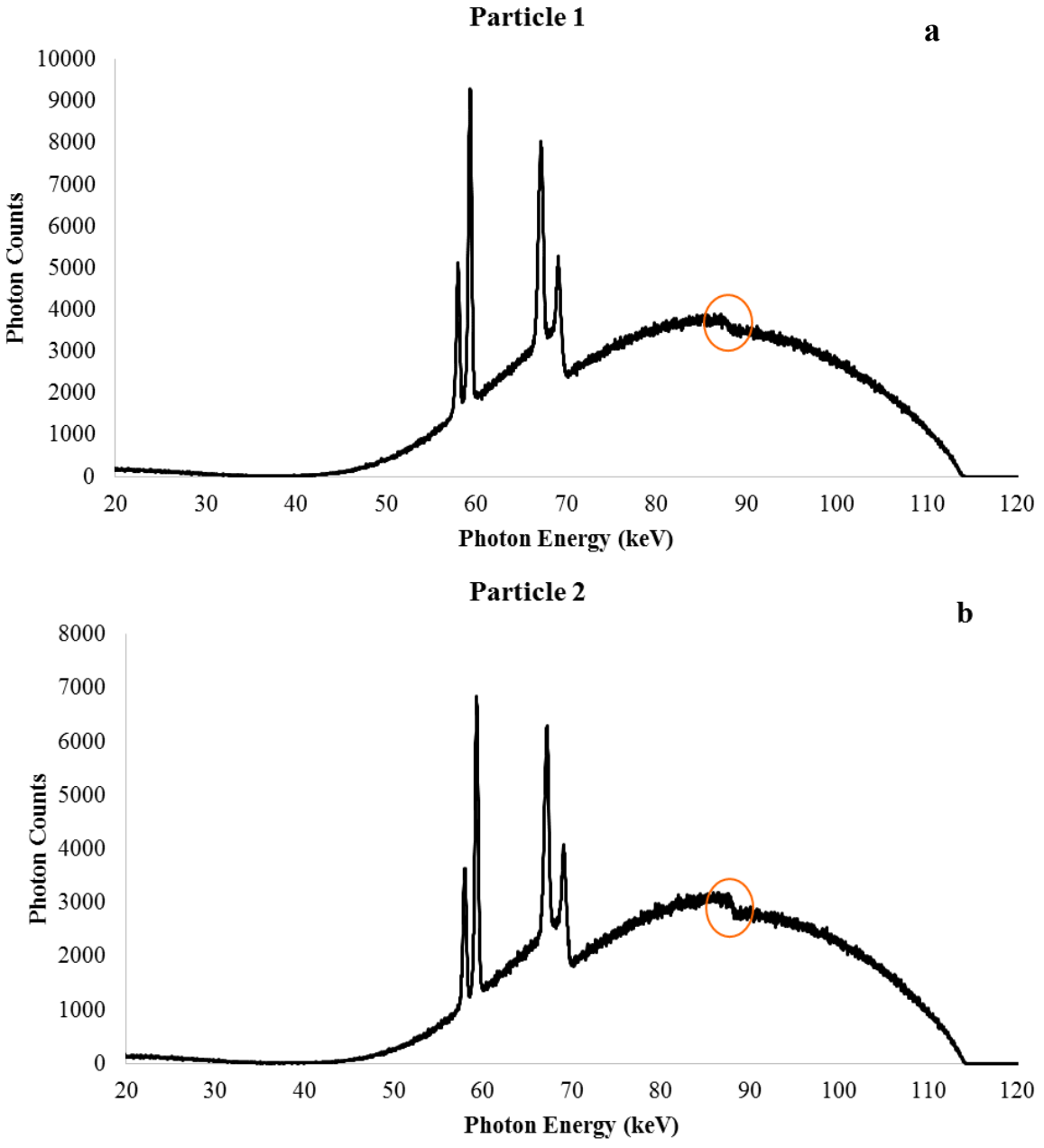

FIG 11—X-ray Bremsstrahlung spectra of metallic particle #1 (a), particle #2 (b), particle #3 (c), and 0.2 mm away from metallic particle #1 (d) (particles numbered from Fig. 3) in the "Vertebrae 2" from the Open Field carcass. The area circled on the plots is the photon energy where the K-edge for lead is located if lead is present.

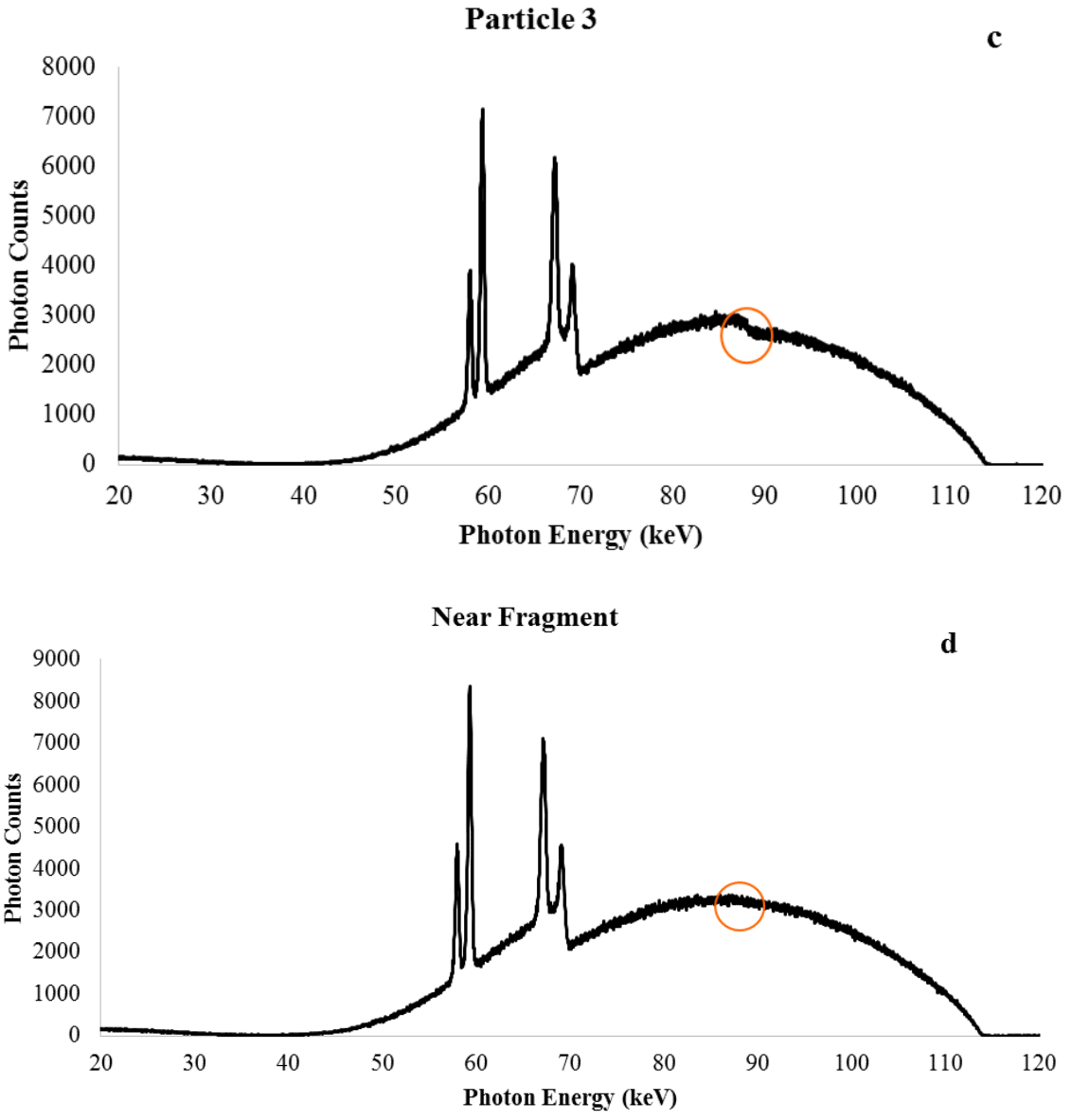

FIG 11 continued—X-ray Bremsstrahlung spectra of metallic particle #1 (a), particle #2 (b), particle #3 (c), and 0.2 mm away from metallic particle #1 (d) (particles numbered from Fig. 3) in the "Vertebrae 2" from the Open Field carcass. The area circled on the plots is the photon energy where the K-edge for lead is located if lead is present.

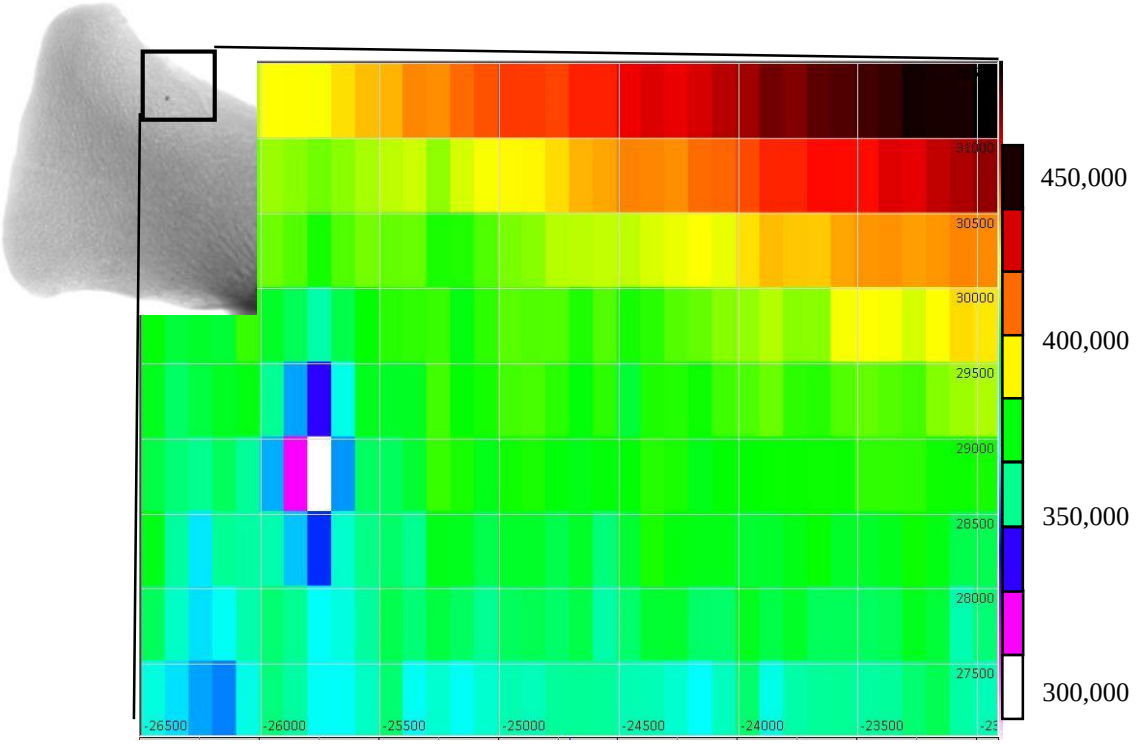

FIG 12—2D raster scan around particle #1 on “Vertebrae 2” from the Open Field carcass (Right). The color look up table to the right indicates the color range corresponding to the photon counts. The axes are distance in µm from the zero point on the translation stages. The black box on the radiograph of the “Vertebrae 2” around particle #1 is the area where the 2D scan was performed (top left).

TABLE 1—Sum of metallic radiopaque particles identified in each bone or bone fragment from the four pig carcasses. Metallic particles from the bolded bones and fragments were analyzed by x-ray, K-edge densitometry.

Winter Carcass	
Right Scapula	9
Left Scapula Fragment 1	3
Left Scapula Fragment 2	2
Left Scapula Fragment 3	1
Left Scapula Fragment 4	4
Left Scapula Fragment 5	4
Left Scapula Fragment6	1
Left Scapula Fragment 7	4
Humerous Fragment 1	7
Humerous Fragment 2	12
Rib 1	14
Rib 2	3
Rib 3 Fragment	10
Rib 4 Fragment	1
Skull	4
Vertebrae 1	7
Vertebrae 2	1
Vertebrae 3	4
Open Field Carcass	
Rib	1
Vertebrae 1	5
Vertebrae 2	8
Trees Carcass	
Right Scapula	8
Rib 1	3
Rib 2	3
Vertebrae Fragment	6
Mandible	4
River Carcass	
Right Scapula	1
Mandible Fragment 1	5
Mandible Fragment 2	1

CHAPTER 6. GENERAL CONCLUSIONS

In Chapter 2, little variation in trace element composition throughout a lipstick sample was observed, showing that lipstick samples were homogeneous. All lipstick samples of different brands or colors are distinguishable from lipstick samples of similar colors based on their trace element compositions in a PCA scores plot. In forensic applications, analysis of lipstick samples with LA-ICP-MS could assist in the identification of the brand and color of an unknown lipstick sample recovered at a crime scene by matching or distinguishing the unknown sample from known lipstick samples based on trace element composition.

Chapter 3 concluded that the heterogeneity of a sample and sampling size must be considered in order to confirm an indistinguishable pair, or distinguish two samples from one another, based on trace elemental composition. The variations in the trace elemental composition along the length of a copper strand are similar to the variations between different strands of the same speaker cable, and cannot be readily distinguished from one another. In actual forensic applications, the possibility of spatial heterogeneity should be evaluated, particularly in cases where only small samples are available (e.g., copper strand fragments after an explosion).

As discussed in Chapter 4, larvae, temperature, and precipitation had substantial effects on the retention of GSR in the skin around gunshot wounds on decomposing carcasses. Elements consistent with GSR and bullet transfer were detected in the skin around the gunshot wounds and larvae feeding from the wounds at higher levels in the gunshot wounds compared to the stab wounds for an extended period of time. In general, these early results indicate potential forensic value of measuring GSR elements in skin and larvae for a period of time throughout the decomposition process.

Little research has been conducted on the retention of GSR or metallic particles from bullet residue on and within skeletonized remains. In Chapter 5, the potential for GSR to be detected on skeletonized remains to aid in the identification of projectile trauma was demonstrated with radiography and K-edge, x-ray densitometry. Identification of projectile trauma on skeletonized remains would be important in forensic investigations in order to assist in determining the cause of death.

Overall, trace elements were determined for forensic comparisons of various samples or detection of GSR on samples. Issues with measuring a representative sample when small fragments are recovered were described. LA-ICP-MS is a relatively non-destructive techniques, whereas x-ray, K-edge densitometry is completely non-destructive. Both techniques have low detection limits for the measurement of trace elements, and most, or all, of the original sample integrity remains intact, which is advantageous in forensic analyses.

APPENDIX A. AN X-RAY FLUORESCENCE STUDY ON THE SEGREGATION OF Cs AND I IN AN INVERTED ORGANIC SOLAR CELL

William R. Lindemann, Teng Xiao, Wenjie Wang, Jonna E. Berry, Nathaniel A. Anderson, Robert S. Houk, Ruth Shinar, Joseph Shinar, David Vaknin

A paper published in Organic Electronics, 2013, 14, 3190-3194.

Abstract

X-ray near-total-reflection fluorescence reveals that in multilayers of the inverted organic solar cell (ITO/CsI/P3HT:PCBM-based) Cs diffuses into the organic layer and iodide diffuses into the ITO. Laser ablation inductively coupled plasma mass spectrometry measurements, which integrate elemental concentration across the whole multilayer structure, indicate that the Cs:I ratio remains 1:1 confirming there is no loss of iodine from the sample. Iodide diffusion to the bulk ITO layer is also found in a similarly prepared ITO/NaI/P3HT:PCBM multilayer structure. Our results are consistent with recent XPS measurements which show that the Cs:I ratio at the ITO/CsI surface exceeds 8:1, and rationalize this observation.

Introduction

Because of their potentially low production costs, organic photovoltaic devices have become an area of critical research in the development of alternative energy sources. Over the past decade, the power conversion efficiency (PCE) of these devices has increased from 1% to over 10%. [1, 2, 3, 4, 5, 6] Many efficient organic devices are

comprised of a polymer/fullerene bulk-heterojunction structure - often studied is a mixture of poly(3-hexylthiophene) (P3HT) and 1-(3-methoxycarbonyl)propyl-1-phenyl[6,6]C_{61} (PCBM). [1, 5, 7]

These devices include 'standard' and 'inverted' configurations. [5] An example of a successful inverted device structure is Glass / ITO / Cs_2CO_3 / P3HT:PCBM Blend / MoO_3 / Al. [8, 9] ITO and aluminum are the cathode and anode, respectively; the Cs_2CO_3 and MoO_3 serve to alter the work function at the nodes. [5, 10]

A cesium iodide film, spin-coated from its aqueous solution as a substitute for the Cs_2CO_3 layer, has been demonstrated to produce a usable solar cell (see Figure 1). [8] However, repeated elemental analysis of the CsI film using x-ray photoelectron spectroscopy (XPS) has demonstrated a surface Cs:I ratio of 8:1. [8] Replacing CsI with CsCl or CsF resulted in inferior devices; however, the Cs:Cl and Cs:F ratios at the ITO surface were much closer to the stoichiometric ratio (i.e. 1.4:1 and 1:1, respectively). [8] Previous attempts to depth-profile organic devices using secondary ion mass spectrometry (SIMS) were not quantitative or conclusive. This study utilized x-ray near-total-reflection fluorescence (XNTRF) and laser ablation inductively coupled plasma mass spectrometry (LA-ICP-MS) to study the apparent depletion of iodine at the ITO surface. Moreover, previous results [8] indicated the presence of Cs at the P3HT:PCBM surface when a solution with higher concentration of CsI was spin-coated on ITO. In the best cells, however, where lower concentrations of CsI were utilized, Cs was not detected in the organic layer. The aforementioned techniques substantiate Cs diffusion into the P3HT:PCBM, even in the optimized cells. XNTRF analysis was also performed on a cesium carbonate cell.

Materials and Methods

A solution of 1:1 P3HT:PCBM (by weight) in 1,2-dichlorobenzene with a concentration of 30 mg/mL was used to spin-coat the organic active layer. P3HT was purchased from Rieke Metals, and PCBM from nano-C; neither was refined further. The P3HT solution was filtered using an 0.22 μm Millex PTFE filter before it was mixed with PCBM. Layers of CsI or NaI and P3HT:PCBM were spin-coated (as previously described) and thermally annealed. [8] MoO_3 and Al layers were not added. Glass/ITO/CsI or NaI/P3HT:PCBM structures were studied, so that only effects caused by layers adjacent to the iodide would be observed. The electron number density (ED) and absorption profiles across the interface of the stratified structure determine the fluorescent volume and allow a depth profile of the concentrations fluorescent elements. The details of the depth profile depend on the quality of the sample and the homogeneity of each stratum.

Here, we limit our depth profile to distinguishing elemental positions only with respect to the ITO/P3HT:PCBM interface, i.e., into ITO substrate or into the P3HT:PCBM film. The ED of ITO (ρ_{ITO}=1.88 e/Å^3) is calculated by assuming that its constituents - In_2O_3 and SnO_2 - are homogeneously mixed, so that electrons are uniformly distributed. The ITO is 90% In_2O_3 and 10% SnO_2 by mass, so the density calculation is weighted accordingly. From ρ_{ITO}, the critical

XNTRF measurements were conducted on the Ames Laboratory horizontal surface spectrometer (LSS) [14] using an UltraX-18 Rigaku x-ray generator with a rotating copper anode (Cu Kα, wavelength λ=1.54 Å), operating at 50 kV and 250 mA.

The Cu *K*α line was selected by a Ge(111) crystal, which steered the downstream beam onto the surface at the desired angle of incidence, α_i. The fluorescence was detected with a Vortex energy dispersive detector (EDD) subtending the illuminated surface (additional details described elsewhere [14]). A schematic of the XNTRF setup is shown in Fig. 1. To determine the relative emission efficiency of emission lines of different elements, salt (i.e., NaI, and CsCl) solutions were measured in a thermostatic, solid Teflon Langmuir trough maintained at 20 ^{o}C. [15] Aqueous solutions of 20mM CsCl and NaI from Sigma Aldrich were prepared using ultrapure water (Milli-Q; resistivity, 18.1 MΩ).

To evaluate the location of the emitting element, we measure the fluorescence as a function of the X-ray incident angle (α) as it determines the penetration depth of the x-ray into the film and thus the rough location of the emitting element. For a uniform interface with no deposited film, below Q_c and dominated by the ED, the evanescent wave penetrates only to a few nm (thus the fluorescence is surface sensitive), whereas above Q_c , the penetration depth is dominated by the absorption of the substrate. Above Q_c, the wave can penetrate organic layers through depths on the order of micrometers.

Quantitatively, the angular dependence of the penetration depth normal to the interface ($D(\alpha)$) is given by

$$D(\alpha)= \frac{1}{\sqrt{2}k_0} \left\{[(\sin^2(\alpha)-\sin^2(\alpha_c))^2-4\beta^2]^{1/2}+\sin^2(\alpha_c)-\sin^2(\alpha)\right\}^{-1/2} \quad (1)$$

where k_0 represents the x-ray wave number, α_c is the critical incident angle for total reflection and β is a constant given by $\beta=\mu/(2k_0)$, where μ is the reciprocal of attenuation length. [14] The incident angle α is related to momentum transfer Q_z by the equation

Q_z=4πsin(α)/λ. Using Eq. 1, below Q_c D≈2.6 nm. Above Q_c (up to Q_z= 0.065 Å^{-1}) D≈36 nm.

On the other hand for a semi-infinite organic layer (P3HT:PCBM) the corresponding penetration depths below and above Q_c are 6.6 nm and 8200 nm. So, below the ITO critical angle for total reflection the fluorescence is mainly from the bulk of the organic layer with some contribution from ITO/organic-layer interface. At larger angles the fluorescence is from both the organic layer and the bulk of the ITO. Due to the complexity of the iodide-ITO surface-structure, these estimates have fairly large uncertainties. They are only used to distinguish signals that emanate from the organic layer and the 'bulk' of the ITO.

When primary x-rays travel through the film, they excite bound electrons, causing the materials to fluoresce. The fluorescence spectra are characteristic of individual elements, allowing the development of a chemical depth profile of each sample. In this study, the x-ray fluorescence spectra of a Glass/ITO/CsI/P3HT:PCBM structure and of a Glass/ITO/NaI/P3HT:PCBM structure were recorded and compared to the spectrum of a Glass/ITO structure. Below the critical angle (α_c) of the ITO layer, reflection from ITO was near-total, and only the ITO surface (atoms within the top 2.6 nm of the ITO) fluoresced. Above α_c, the beam penetrated into the bulk of ITO, so that fluorescence data included signal from bulk ITO (atoms up to 36 nm into the ITO) as well as signal from the surface. The intensity of the $L\alpha$ emission lines for Cs and I was used to compare the relative quantities of cesium and iodine in each structure.

Because of the overlap of cesium and iodine spectra, x-ray fluorescence spectra (data not shown) for 20 mM NaI and CsCl bulk solutions were recorded to determine the

relative sensitivity to each element. Their spectral profiles served as references for obtaining the Cs:I ratio in the samples. These profiles were used to generate ideal Gaussian distributions around the Lα peaks of cesium in the Glass/ITO/CsI/P3HT:PCBM structure. The full-width at half-maximum of the cesium peak was determined and scaled peaks of equivalent widths were placed at the ideal location of the Lα peak for iodine.

LA-ICP-MS was then used to analyze this same Glass/ITO/CsI/P3HT:PCBM structure. Several linear, lateral trenches were dug into the sample using a 100 fs laser (Coherent Libra, 266 nm, 10 μJ/pulse, 1000 pulses/s). The ablated particulates were transported from the LA cell to the sample with argon carrier gas. Signals for Sn^+, I^- and Cs^+ were acquired using a magnetic sector mass spectrometer (Thermo Finnigan Element 1, resolution $m/\Delta m \approx 300$). Plasma and ion optical conditions were optimized to provide maximum signal and signal stability during ablation of NIST glass 610 reference material. The background was measured with the laser off and argon flowing through the sample cell into the plasma.

Results

LA-ICP-MS data (Fig. 2) indicated the presence of iodine in significant quantities in the CsI-based structure. Figure 2 shows that signals for Cs^+ and I^- rise together soon after the ablation starts. The steady-state signal levels for I^- and Cs^+ were used to estimate the relative concentrations of the two elements (Table 1). This calculation assumed the ionization efficiencies for Cs and I were 100% and 29%, respectively. [16] The Cs:I concentration ratio is close enough to unity to indicate that iodine was not greatly depleted from the structure.

The ablated trenches were examined with a profilometer and found to be approximately 70 μm wide x 20 μm deep, i.e., deep enough so the trench penetrated through the P3HT:PCBM, the CsI and the ITO layers. This explains the observation of Sn^{+} signals from the ITO layer in Fig. 2.

X-ray fluorescence spectra were collected for ITO, a Glass / ITO / CsI / P3HT:PCBM structure, and a Glass / ITO / NaI / P3HT:PCBM structure. Overlap between the spectra of cesium, iodine and indium made precise calculation of the quantities of these chemicals difficult. To avoid interference from indium, the spectrum for ITO was subtracted from the spectra of the other two. In the energy range of 3.8 - 5.0 keV, only iodine, cesium and indium showed peaks, so after subtraction, all intensity was assumed to be due to the presence of cesium and/or iodine.

Figure 3 shows the fluorescence spectra after subtraction. Figure 3 (a) shows fluorescence signals integrated above the ITO critical angle. These peaks are mainly due to the bulk contribution of cesium and iodine. The scaled Gaussian reference peaks coincide well with the data for the CsI structure, indicating a near-stoichiometric Cs:I ratio. Moreover, the iodine fluorescence intensities originating from the bulk of the structures were nearly indistinguishable from one another, which is consistent with the fact that NaI and CsI of equivalent molarity were deposited onto the substrate under identical conditions.

Figure 3 (b) shows fluorescence signal integrated below the ITO critical angle, originating from the bulk of the P3HT:PCBM layer and from the surface of the ITO. Gaussian distributions around the Lα peak of cesium indicate a significant presence of cesium in the organic layer and on the ITO surface. However, fluorescence signals around

the Lα peak of iodine were much weaker than the scaled reference peaks, indicating the significant depletion of iodine from the surface in both structures - i.e. the surface ratio of Na:I and of Cs:I was much greater than 1. No signal was observed below the critical angle of the P3HT:PCBM layer, indicating that cesium did not reach the surface of the organic layer.

Conclusions

This study demonstrates that in inverted organic photovoltaic cells with a CsI interlayer, iodide diffuses into the ITO. Based on LA-ICP-MS data, the possibility that the iodine was lost during the preparation process was eliminated. Fluorescence results indicate that surface iodine in both sodium iodide and cesium iodide interlayers is depleted, supporting the XPS results of Xiao et al. [8] However, once the surface of the ITO layer of these structures was penetrated, fluorescence data clearly indicated the presence of iodine, suggesting the diffusion of iodine into the ITO interlayer. Fluorescence results also demonstrate a significant presence of cesium in the P3HT:PCBM layer, suggesting the diffusion of cesium into the organic interlayer. XNRTF analyses also demonstrated this diffusion in a Cs_2CO_3 device. These results, however, await further analysis.

Neutron reflectivity data indicate that in annealed P3HT:PCBM layers, PCBM concentrations are disproportionately high near the external interfaces of the organic film. [12] Graphite intercalation experiments demonstrate that, under the appropriate conditions, cesium interacts spontaneously with carbon, so the diffusion of cesium into

the P3HT:PCBM interlayer may be explained by the interaction of cesium with the fullerenes in the organic layer. [17]

Based on the XPS findings [8], it is believed that the diffusion of iodine may be a consequence of iodine's high polarizability, since the Cs:X ratio decreased sharply with halide polarizability. Because of the spectral overlap of indium, iodine and cesium, quantitative depth profiling of this phenomenon was not possible using these methods.

Acknowledgements

We would like to acknowledge the generous financial support of the Iowa State University Foundation. The work at Ames Laboratory was supported by the Office of Basic Energy Sciences, U.S. Department of Energy under Contract No. DE-AC02-07CH11358. Ruth Shinar acknowledges partial support of the Iowa Energy Center.

References

[1] Z. Liu and E. Lee, "Efficiency improvement in fullerene-layer-inserted organic bulk-heterojunction solar cells," *J. Appl. Phys.*, vol. 111, 2012.

[2] L. Dou, Y. Jingbi, J. Yang, C. C. Chen, Y. He, S. Murase and et al. , "Tandem polymer solar cells featuring a spectrally matched low-bandgap polymer," *Nat. Photonics,* vol. 6, pp. 180-185, 2011.

[3] Z. He, C. Zhong, X. Huang, W. Wong, H. Wu, L. Chen, S. Su and Y. Cao, "Simultaneous enhancement of open-circut voltage, short-circut current density, and fill factor in polymer solar cells," *Advanced Mater,* vol. 23, pp. 4636-4643, 2011.

[4] "National Renewable Energy Laboratory: NREL," Best Research-Cell Efficiencies, 5 June 2015. [Online]. Available: www.nrel.gov/ncpv/images/efficiency_chart.jpg.

[5] J. Nelson, "Polymer: fullerene bulk heterojunction solar cells," *Mater,* vol. 14, pp. 462-470, 2011.

[6] R. A. Janssen and J. Nelson, "Factors limiting device efficiency in organic photovoltaics," *Advanced Mater,* vol. 25, pp. 1847-1858, 2013.

[7] G. Dennler, M. C. Scharber and C. J. Brabec, "Polymer-fullerene bulk-heterojunction solar cells," *Advanced Mater,* vol. 21, pp. 1323-1338, 2009.

[8] T. Xiao, W. Cui, M. Cai, W. Leung, J. W. Anderegg, J. Shinar and R. Shinar, "Inverted polymer solar cells with a solution-processed cesium halide interlayer," *Org. Electronics,* vol. 14, pp. 267-272, 2013.

[9] T. Lee, J. H. Youn, M. S. Ryu, J. Kim, H. T. Moon and J. Jang, "Electrical properties of inverted poly(3-hexylthiophene): methano-fullerene [6,6]-phenyl C-71-butyric acid methly ester bulk hetero-junction solar cell with Cs2CO3 and MoO3 layers," *Sol. Eng. Mater. and Sol. Cells,* vol. 95, pp. 3276-3280, 2011.

[10] G. Li, C. W. Chu, V. Shrotriya, J. Huang and Y. Yang, "Efficient inverted polymer solar cells," *Appl. Phys. Letters,* vol. 88, pp. 1077-3188, 2006.

[11] J. Als-Nielsen and D. McMorrow, Elements of modern x-ray physics, West Sussex: John Wiley and Sons Ltd., 2001.

[12] J. W. Kiel, B. J. Kirby, C. F. Majkrzak, B. B. Maranville and M. E. Mackay, "Nanoparticle concentration profile in polymer-based solar cells," *Soft Matter,* vol. 6, pp. 641-646, 2010.

[13] N. D. Treat, M. A. Brady, G. Smith, M. F. Toney, E. J. Kramer, C. J. Hawker and M. L. Chabinyc, "Interdiffusion of PCBM and P3HT reveals miscibility in a photovoltaically active blend," *Adv. Energy Mater.,* vol. 1, pp. 82-89, 2011.

[14] D. Vaknin, X-ray diffraction and spectroscopic techniques for liquid surfaces and interfaces in: E.N. Kaufmann (Ed.) characterization of materials, John Wiley and Sons, 2012.

[15] W. Wang, R. Park, D. H. Meyer, A. Travesset and D. Vaknin, "Ionic specificity and pH regulated charged interfaces: Fe3+ versus La3+," *Langmuir,* vol. 27, pp. 11917-11924, 2011.

[16] K. G. Jarvis, A. L. Gray and R. S. Houk, Handbook of ICP-MS, New York: Chapman and Hall, 1992.

[17] M. S. Dresselhaus and G. Dresselhaus, "Intercalation compounds of graphite," *Advances in Phys.,* vol. 51, pp. 1-186, 2002.

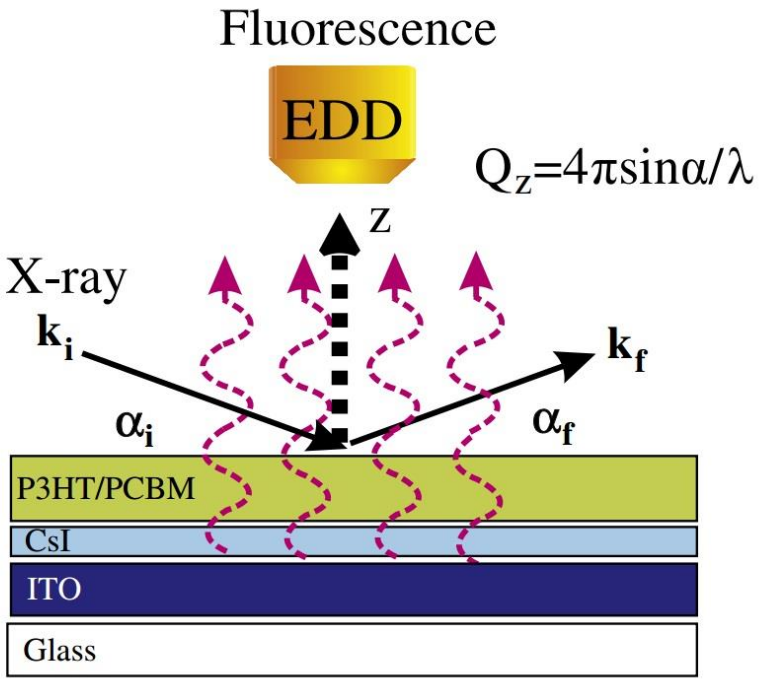

Figure 1: Schematic of x-ray fluorescence setup and the CsI structure used in experimentation (not to scale). The commonly used Cs_2CO_3, spun from an organic solution, was replaced with CsI. The structure studied did not include MoO_3 or Al layers. In the diagram, α_i is the angle of incidence, α_f is the angle of reflectance, and $\alpha_i=\alpha_f=\alpha$. Z is the surface normal, and k_i and k_f are the momentum vectors of incident and reflected photons, respectively. An energy dispersive detector (EDD) records the fluorescence signal.

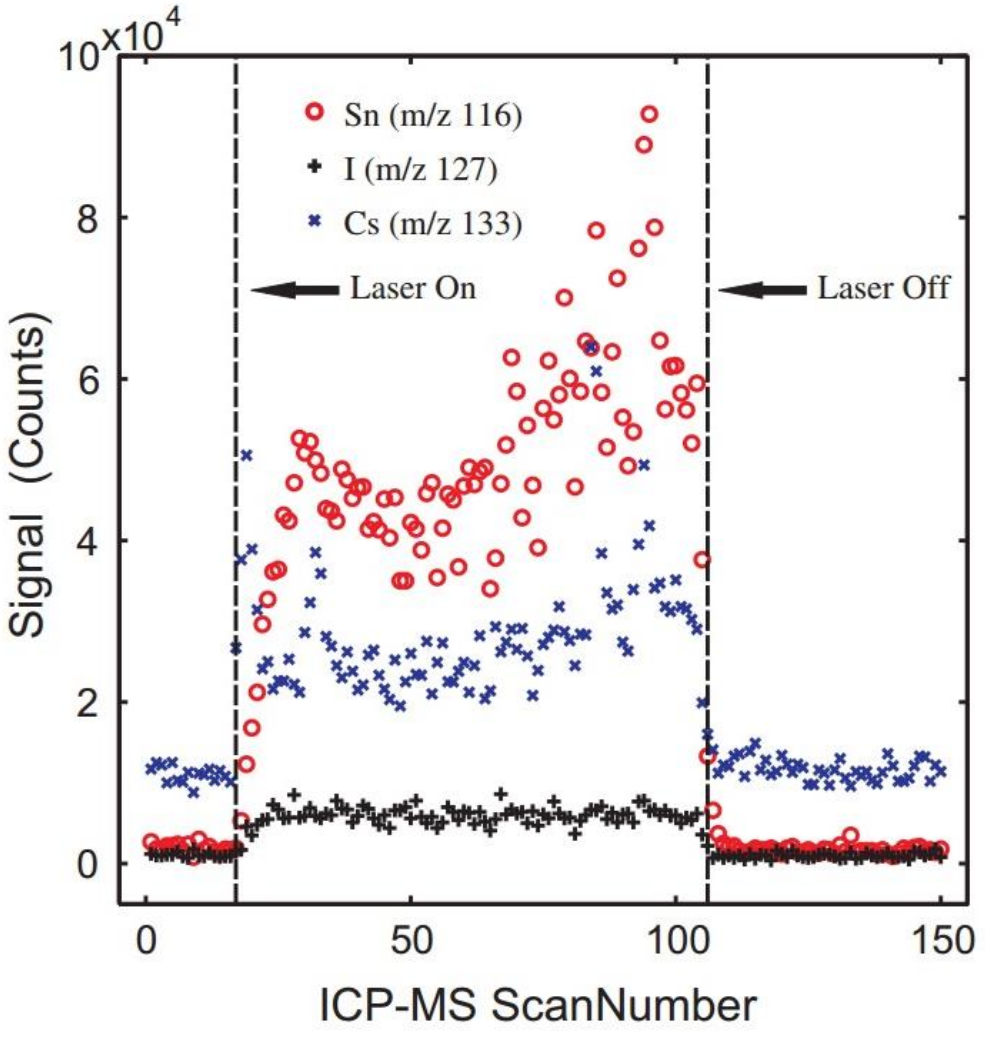

Figure 2: Mass spectra of I, Cs, and Sn over 150 scans of the ICP-MS. Mass spectra were determined for lateral ablations across the sample surface. Scans 0-18 and 108-150 are the background signals for the three m/z values acquired with the laser off. Scans 19-107 were acquired while the laser was ablating the Glass/ITO/CsI/P3HT:PCBM structure in a single line scan.

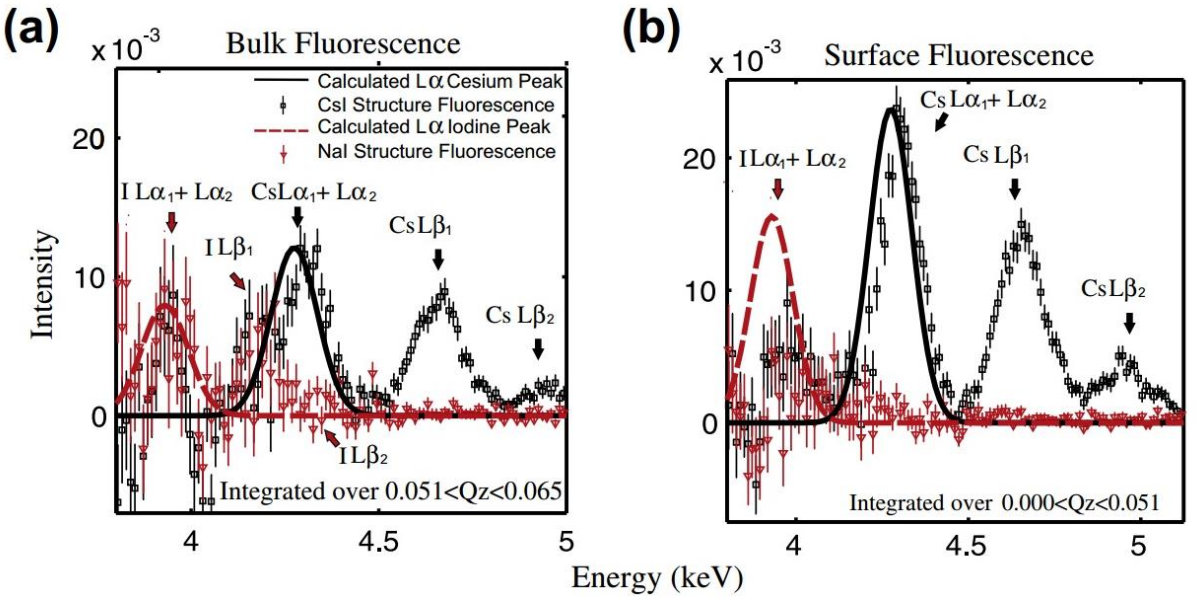

Figure 3: Integrated bulk and surface fluorescence intensities of a Glass / ITO / NaI / P3HT:PCBM structure and of a Glass/ITO/CsI/P3HT:PCBM structure with the ITO spectrum subtracted. Gaussian distributions were plotted around the Lα lines for cesium and iodine. Data (with error bars) are displayed along with ideal peaks, displayed as solid lines. Units of intensity are arbitrary.

Table 1: Ratio of cesium to iodine (within one standard deviation) in CsI structure, as determined by LA-ICP-MS.

Cs:I	Trial 1	Trial 2	Trial 3
Average Concentration Ratio	1.18±0.44	1.38±0.36	1.40±0.28

ACKNOWLEDGEMENTS

The research in chapters 2 and 3 were funded under a grant by the National Institute of Justice (award number: 2009-DN-R-112). The work in chapters 4 and 5 at the Ames Laboratory was supported by the National Institute of Justice Graduate Research Fellowship (Award No. 201-IJ-CX-0012). The studies described in chapter 2-4 were performed at Ames Laboratory under Contract No. DE-AC02- 07CH11358 with the U.S. Department of Energy (USDOE). Research for chapter 5 was performed at Iowa State University (ISU) Center for Nondestructive Evaluation (CNDE).

I would like to thank a number of people for their encouragement and support throughout my time as a graduate student at ISU. First, I would like to thank Dr. R. S. Houk for his assistance and guidance, as well as, for allowing and supporting me to pursue forensically based research projects throughout my graduate career. I would like to thank Dr. Stan Bajic for his advice and support during my research and also for his PCA instruction. For their assistance and instruction with the femtosecond laser I would like to thank Stan Bajic and Dan Zamzow. I would also like to thank Dr. David Baldwin for his advice, support, and for his forensic knowledge and referrals. I would like to extend my gratitude to three former Houk group members, Megan Mekoli, Chris Ebert, and Travis Witte for providing me with introductory knowledge of ICP-MS and laser ablation, and for their support and friendship. Chapter 5 of this dissertation would not have been completed without Scott Wendt and Dr. Joe Gray at the CNDE. I am very grateful for their assistance, instruction, advice, and support for that project.

A big thank you to my friends here at ISU for your support and friendship throughout my graduate career. I would like to acknowledge Katherine Weber, Jeneé Jacobs, Mark Juetten, Jonathan Bobbitt, Daniel Freppon, Alexander Buck, and Malinda

Reichert for helping to dig trenches for pig cages, and for their assistance transporting and placing 250 pound pig carcasses into the cages. Jeneé Jacobs has been there for me through this journey with her support, advice, and assistance with numerous projects, including her help with the pig carcasses, many times. Jeneé has not only been my co-worker for the past five years, but also my best friend and graduate school would not have been the same without her. I would also like to thank Katherine Weber for her continuous support and encouragement. Her constant optimism has helped me get through many difficult times during my graduate studies.

Lastly, I would like to thank my parents Fred and Diane Berry for their unwavering love and support throughout my entire life, as well as, my little sister, Christa Berry, for her support and her comic relief during difficult times. I would also like to thank my grandparents Kent and Jean Johnson, and the rest of my extended family for their love, encouragement, and support throughout my many adventures. I am very blessed to have this wonderful family as my foundation for past, present, and future endeavors.